USGS
science for a changing world

Prepared in cooperation with the North Dakota State Water Commission

Stochastic Model for Simulating Souris River Basin Precipitation, Evapotranspiration, and Natural Streamflow

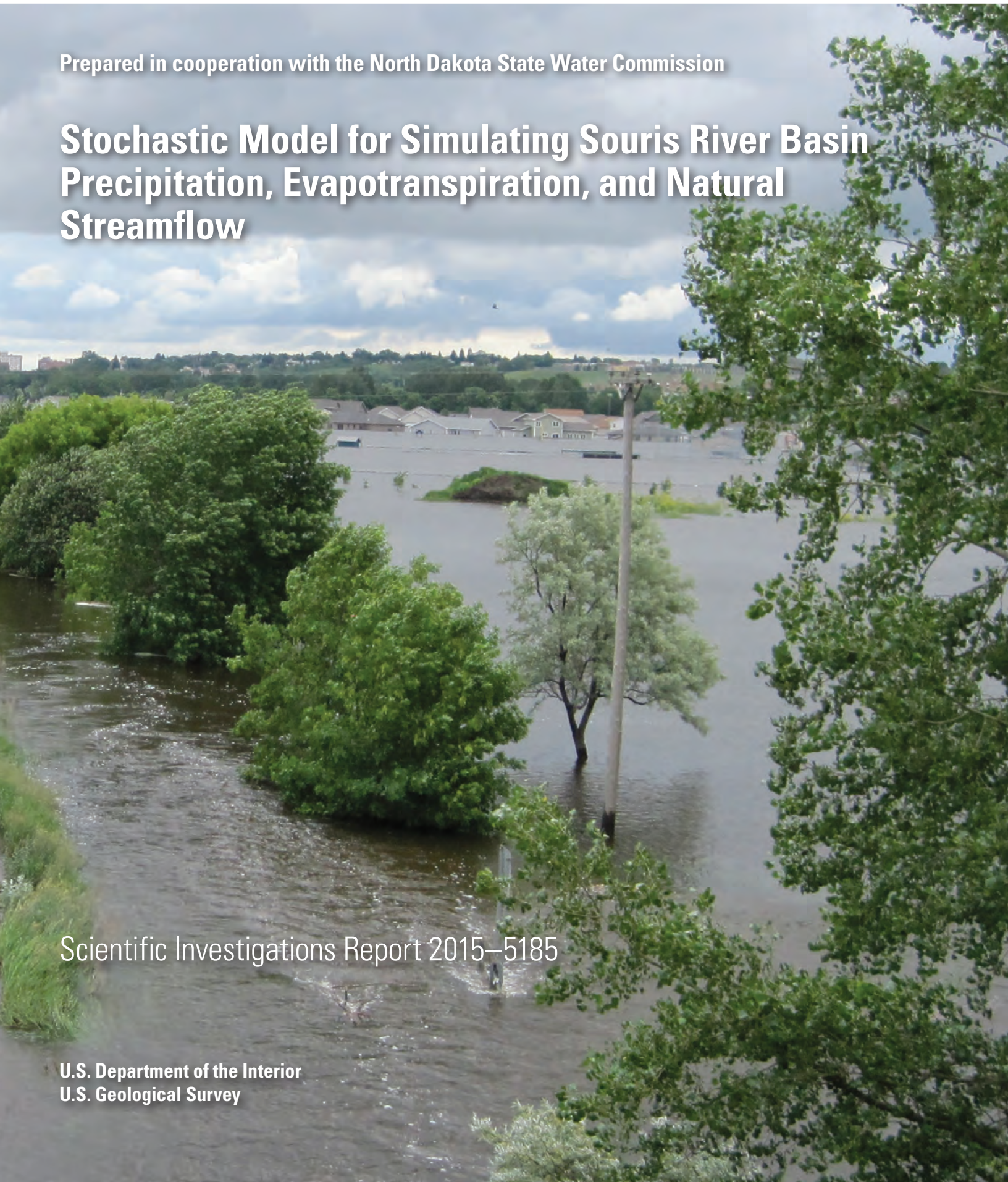

Scientific Investigations Report 2015–5185

U.S. Department of the Interior
U.S. Geological Survey

Covers. Floodwaters of the Souris River surrounding homes (front) and railroad tracks (back) in Minot, North Dakota, June 27, 2011 (photograph by Brent R. Hanson, U.S. Geological Survey).

Stochastic Model for Simulating Souris River Basin Precipitation, Evapotranspiration, and Natural Streamflow

By Kelsey A. Kolars, Aldo V. Vecchia, and Karen R. Ryberg

Prepared in cooperation with the North Dakota State Water Commission

Scientific Investigations Report 2015–5185

U.S. Department of the Interior
U.S. Geological Survey

U.S. Department of the Interior
SALLY JEWELL, Secretary

U.S. Geological Survey
Suzette M. Kimball, Director

U.S. Geological Survey, Reston, Virginia: 2016

For more information on the USGS—the Federal source for science about the Earth, its natural and living resources, natural hazards, and the environment—visit http://www.usgs.gov or call 1–888–ASK–USGS.

For an overview of USGS information products, including maps, imagery, and publications, visit http://www.usgs.gov/pubprod/.

Suggested citation:
Kolars, K.A., Vecchia, A.V., and Ryberg, K.R., 2016, Stochastic model for simulating Souris River Basin precipitation, evapotranspiration, and natural streamflow: U.S. Geological Survey Scientific Investigations Report 2015–5185, 55 p., http://dx.doi.org/10.3133/sir20155185.

ISSN 2328-0328 (online)

Acknowledgments

We gratefully acknowledge Tim Fay and Mitch Weier of the North Dakota State Water Commission for their helpful reviews and Chanel Mueller of the U.S. Army Corps of Engineers, St. Paul District, for providing the natural (unregulated) streamflow data.

We also wish to acknowledge U.S. Geological Survey employees Don Rosenberry and Stacey Archfield for their helpful reviews and Tara Gross for providing technical support.

Contents

Figures

Tables

Conversion Factors

Inch/Pound to International System of Units

Multiply	By	To obtain
	Volume	
acre-foot (acre-ft)	1,233	cubic meter (m^3)
acre-foot (acre-ft)	0.001233	cubic hectometer (hm^3)

International System of Units to Inch/Pound

Multiply	By	To obtain
	Length	
centimeter (cm)	0.3937	inch (in.)
millimeter (mm)	0.03937	inch (in.)
kilometer (km)	0.6214	mile (mi)
kilometer (km)	0.5400	mile, nautical (nmi)
	Area	
square kilometer (km^2)	247.1	acre
square kilometer (km^2)	0.3861	square mile (mi^2)
	Volume	
cubic meter (m^3)	6.290	barrel (petroleum, 1 barrel = 42 gal)
cubic meter (m^3)	264.2	gallon (gal)
cubic meter (m^3)	0.0002642	million gallons (Mgal)
cubic meter (m^3)	35.31	cubic foot (ft^3)
cubic meter (m^3)	1.308	cubic yard (yd^3)
cubic meter (m^3)	0.0008107	acre-foot (acre-ft)
	Flow rate	
cubic meter per second (m^3/s)	70.07	acre-foot per day (acre-ft/d)
cubic meter per second (m^3/s)	35.31	cubic foot per second (ft^3/s)
cubic meter per second (m^3/s)	22.83	million gallons per day (Mgal/d)
centimeter per hour (cm/h)	0.3937	inch per hour (in/h)

Temperature in degrees Celsius (°C) may be converted to degrees Fahrenheit (°F) as °F = (1.8 × °C) + 32.

Datums

Horizontal coordinate information is referenced to the North American Datum of 1983 (NAD 83) and projected to the USA Contiguous Albers Equal Area Conic U.S. Geological Survey version.

Stochastic Model for Simulating Souris River Basin Precipitation, Evapotranspiration, and Natural Streamflow

By Kelsey A. Kolars, Aldo V. Vecchia, and Karen R. Ryberg

Abstract

The Souris River Basin is a 61,000-square-kilometer basin in the Provinces of Saskatchewan and Manitoba and the State of North Dakota. In May and June of 2011, record-setting rains were seen in the headwater areas of the basin. Emergency spillways of major reservoirs were discharging at full or nearly full capacity, and extensive flooding was seen in numerous downstream communities. To determine the probability of future extreme floods and droughts, the U.S. Geological Survey, in cooperation with the North Dakota State Water Commission, developed a stochastic model for simulating Souris River Basin precipitation, evapotranspiration, and natural (unregulated) streamflow. Simulations from the model can be used in future studies to simulate regulated streamflow, design levees, and other structures; and to complete economic cost/benefit analyses.

Long-term climatic variability was analyzed using tree-ring chronologies to hindcast precipitation to the early 1700s and compare recent wet and dry conditions to earlier extreme conditions. The extended precipitation record was consistent with findings from the Devils Lake and Red River of the North Basins (southeast of the Souris River Basin), supporting the idea that regional climatic patterns for many centuries have consisted of alternating wet and dry climate states.

A stochastic climate simulation model for precipitation, temperature, and potential evapotranspiration for the Souris River Basin was developed using recorded meteorological data and extended precipitation records provided through tree-ring analysis. A significant climate transition was seen around 1970, with 1912–69 representing a dry climate state and 1970–2011 representing a wet climate state. Although there were some distinct subpatterns within the basin, the predominant differences between the two states were higher spring through early fall precipitation and higher spring potential evapotranspiration for the wet compared to the dry state.

A water-balance model was developed for simulating monthly natural (unregulated) mean streamflow based on precipitation, temperature, and potential evapotranspiration at select streamflow-gaging stations. The model was calibrated using streamflow data from the U.S. Geological Survey and Environment Canada, along with natural (unregulated) streamflow data from the U.S. Army Corps of Engineers. Correlation coefficients between simulated and natural (unregulated) flows generally were high (greater than 0.8), and the seasonal means and standard deviations of the simulated flows closely matched the means and standard deviations of the natural (unregulated) flows. After calibrating the model for a monthly time step, monthly streamflow for each subbasin was disaggregated into three values per month, or an approximately 10-day time step, and a separate routing model was developed for simulating 10-day streamflow for downstream gages.

The stochastic climate simulation model for precipitation, temperature, and potential evapotranspiration was combined with the water-balance model to simulate potential future sequences of 10-day mean streamflow for each of the streamflow-gaging station locations. Flood risk, as determined by equilibrium flow-frequency distributions for the dry (1912–69) and wet (1970–2011) climate states, was considerably higher for the wet state compared to the dry state. Future flood risk will remain high until the wet climate state ends, and for several years after that, because there may be a long lag-time between the return of drier conditions and the onset of a lower soil-moisture storage equilibrium.

Introduction

The Souris River Basin is a 61,000-square-kilometer (km^2) basin in the Provinces of Saskatchewan and Manitoba and the State of North Dakota (fig. 1). The basin topography consists of gently rolling prairie landscape and flat valleys. The main channel of the Souris River is approximately 700 kilometers (km) in length, originating in southeast Saskatchewan, flowing southeast into North Dakota, and then continuing northward into Manitoba. The flow upstream from Minot, N. Dak., is affected by regulation from the Rafferty, Alameda, and Boundary Reservoirs in Saskatchewan and Lake Darling in North Dakota (fig. 1), which are operated in accordance with an international agreement between Canada and the United States (International Joint Commission, 1989).

Widespread record-setting flooding took place in the Souris River Basin from May to August of 2011. The flooding

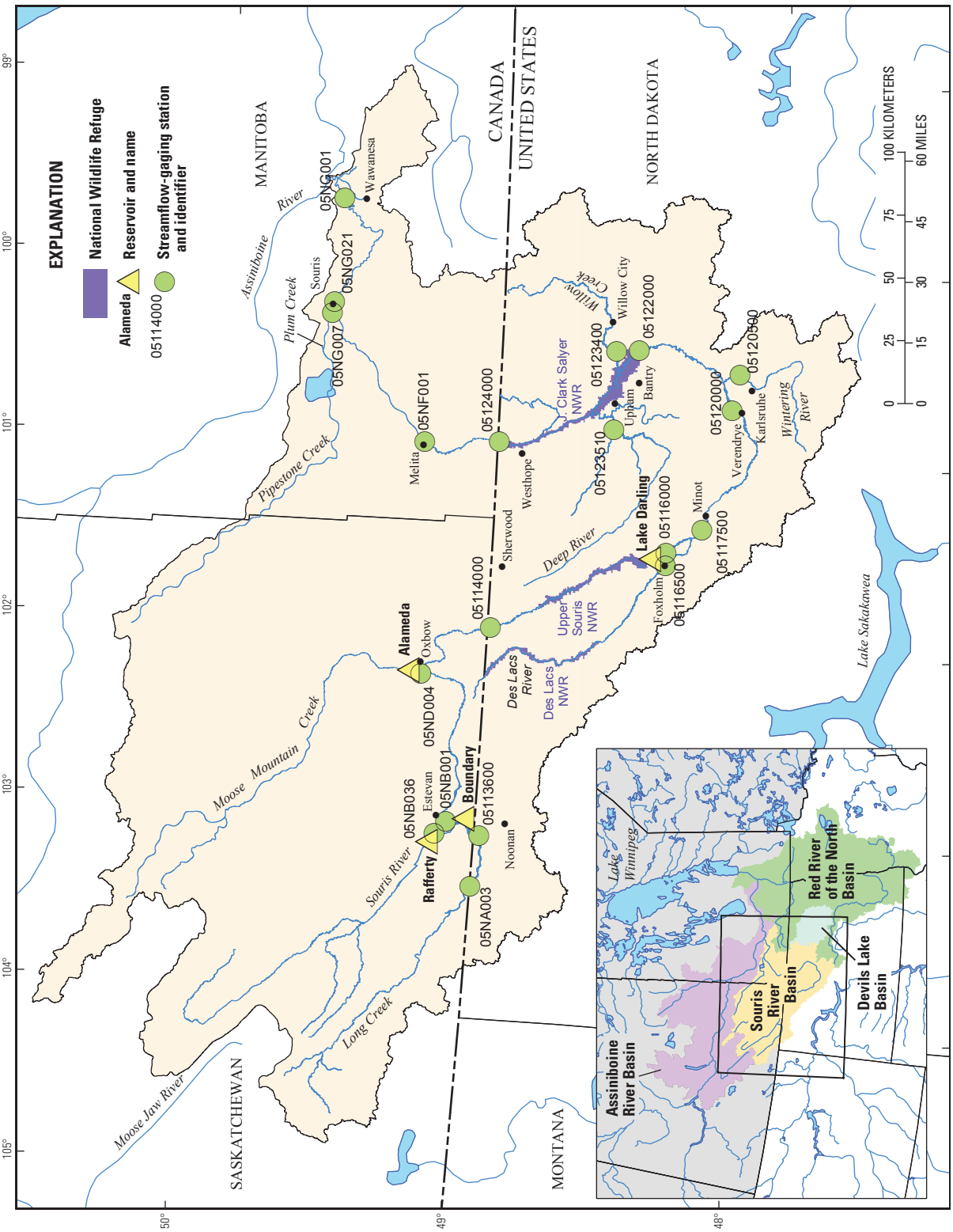

Figure 1. Souris River Basin showing locations of major reservoirs and streamflow-gaging stations used for developing the stochastic natural streamflow model.

resulted from an unusually wet fall season in 2010, high snowfall during the subsequent winter season, and a series of record-setting rains during May and June 2011 in the headwater areas of the Souris River Basin in Saskatchewan and North Dakota (U.S. Department of Commerce, 2012). Emergency spillways of the upstream reservoirs were discharging at or near capacity, which resulted in extensive flooding to numerous downstream communities, including Minot, N. Dak., that had devastating damages with more than 4,000 homes flooded (U.S. Department of Commerce, 2012). Annual peak streamflow for the Souris River above Minot, N. Dak., (streamflow-gaging station 05117500) during 2011 was more than 736 cubic meters per second (m^3/s), which was more than twice that of any previously recorded peak streamflow since 1904 and more than five times the estimated 100-year post-regulation peak streamflow (142 m^3/s; fig. 2; U.S. Geological Survey, 2014b).

As a result of the record 2011 flood, a Souris River Basin Task Force convened to develop a plan of study for determining the likelihood of future severe flooding events, reviewing existing operating plans for upstream reservoirs, and improving downstream levees and other structures for mitigating future damages (International Souris River Board, 2013). One of the recommendations of the task force was to develop a stochastic model for simulating future streamflow and evaluating the probability of future severe floods or droughts. Streamflow modeling in the Souris River Basin is particularly challenging because of the extreme climatic variability and flat topography of the basin. As a result of the task force recommendation, the U.S. Geological Survey (USGS), in cooperation with the North Dakota State Water Commission, developed a stochastic model for simulating future Souris River Basin precipitation, evapotranspiration, and natural (unregulated) streamflow. Simulations from the model can be used in future studies to simulate regulated streamflow, design levees, and other structures, and complete economic cost/benefit analyses.

Purpose and Scope

The purpose of this report is to describe a stochastic natural streamflow model and present results of model simulations for evaluating the probability of future floods in the Souris River Basin. The stochastic natural streamflow model was developed through a series of four stages that are described in subsequent sections of this report:

1. analysis of long-term climatic variability in the Souris River Basin and surrounding region,
2. development of a stochastic climate model for simulating climatic inputs,
3. development of a water-balance model for simulating natural (unregulated) monthly streamflow in response to climatic inputs, and
4. development of a natural (unregulated) streamflow routing model for simulating streamflow at a three-per-month (approximately 10-day) time step.

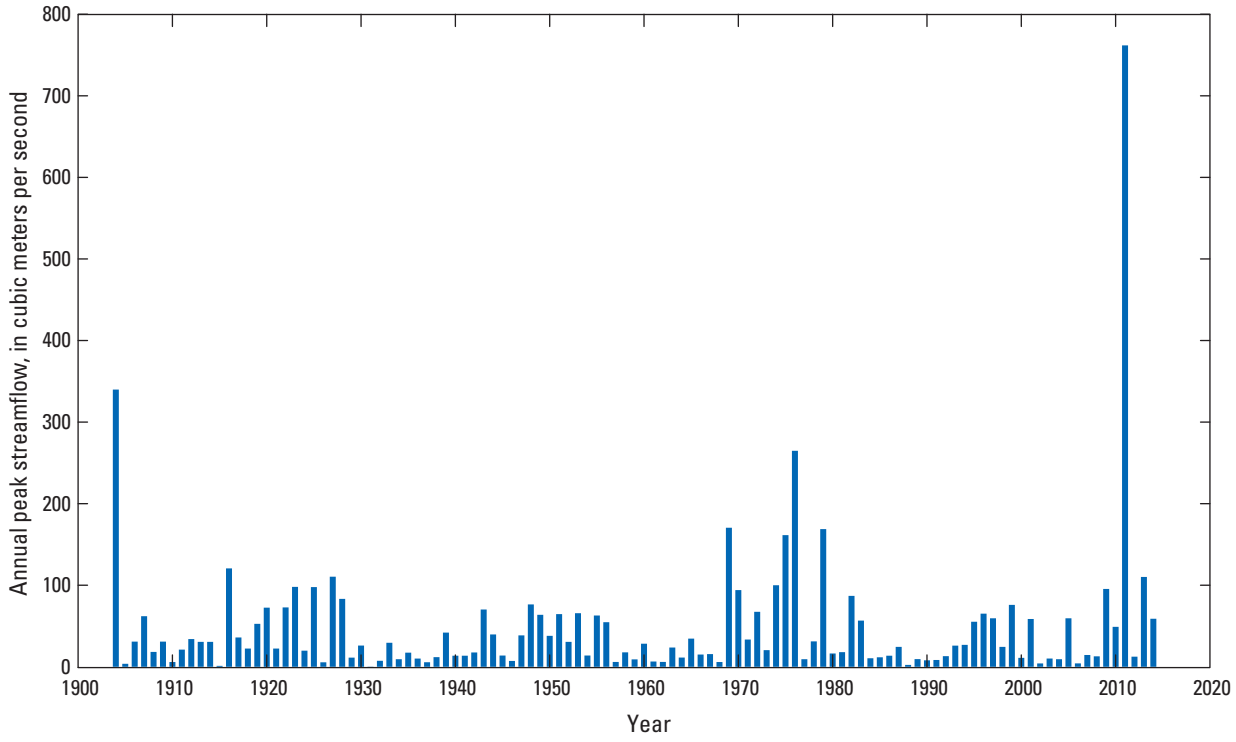

Figure 2. Annual peak streamflow for the Souris River above Minot, North Dakota streamflow-gaging station (05117500) 1904–2014.

Analysis of Long-Term Climate Variability

Long-term climate variability was analyzed using tree-ring data to extend historical precipitation records from the Souris River Basin and surrounding areas back to the early 1700s and to compare recent (since the late 1800s) "extreme" wet and dry conditions to earlier conditions. The methods and results summarized in this section are described in detail in Ryberg (2015). A brief overview is given in this report to provide background information for the subsequent sections.

Data and Methods

To evaluate climate variability for the Souris River Basin in a larger regional context, historical precipitation and temperature data were obtained from United States and Canadian meteorological stations in an area extending beyond the Souris River Basin boundary and including parts of other basins in the region, including the Missouri River, Red River of the North, Assiniboine River, and Saskatchewan River (fig. 3). Monthly precipitation and temperature (average, maximum, and minimum) data were downloaded for Canadian stations from the Adjusted and Homogenized Canadian Climate Data (AHCCD; Environment Canada, 2014) and were downloaded for U.S. stations from the United States Historical Climatology Network (USHCN; Menne and others, 2014). The AHCCD and USHCN datasets are designed to minimize potential trends because of changes in instrumentation, station locations, and other factors unrelated to natural climate variability or climate change.

Tree-ring data were downloaded from The International Tree-Ring Data Bank (ITRDB; National Oceanic and Atmospheric Administration National Climate Center, 2014). As described in Ryberg (2015), after careful analysis of data from sites within and near the study boundary, four sites were selected for inclusion in the analysis (fig. 3): Boundary Bog in Saskatchewan, Theodore Roosevelt National Park and Burning Coal Vein in North Dakota, and Cedar Butte in South Dakota.

Monthly precipitation and temperature data for each of the AHCCD and USHCN meteorological stations were aggregated to obtain seasonal total precipitation and average temperature for three 4-month seasons: season 1 (November–February), season 2 (March–June), and season 3 (July–October). These seasons were selected because climatic conditions in each season have a distinct and important effect on runoff for the Souris River Basin. Precipitation during season 1 generally is trapped in frozen soils or stored in the basin as snowpack and either replenishes soil moisture deficits from the previous summer or provides snowmelt runoff. Season 2 generally is the period when peak streamflow from snowmelt runoff and (or) spring rainfall takes place, and season 3 generally is a period of low flows and moisture deficits as potential evapotranspiration (PET) exceeds precipitation and soil moisture is depleted.

Hierarchical agglomerative cluster analysis (HACA; Maechler and others, 2014) was used to identify five distinct climatic clusters of sites based on mean seasonal precipitation (1900–2010; fig. 4). Precipitation and temperature were initially considered for the cluster analysis, but precipitation was by far the dominant of the two variables; thus, temperature was not used (Ryberg, 2015). The position of the Souris River Basin and its partitioning into multiple clusters (fig. 4) highlights the complexity and variability of climatic conditions in the basin despite its small size.

To focus on regional-scale temporal variability, precipitation data for each season and each cluster were averaged over the stations in the cluster to obtain 15 (5 clusters times 3 seasons) yearly time series for the period 1888 through 2010; furthermore, to remove high-frequency variability and focus on long-term (multidecadal) variability, the yearly time series were averaged over 12-year moving windows. A 12-year window was used because a number of studies have identified quasi-periodic signals with wavelengths of 12 years or less for precipitation in the north-central United States and south-central Canada during various seasons (Ault and St. George, 2010; Small and Islam, 2008, 2009; Garbrecht and Rossel, 2002; Yang and others, 2007).

To hindcast the seasonal precipitation, each of the 15 smoothed yearly time series described in the previous paragraph were modeled based on the annual tree-ring chronologies. Multiresolution decomposition (Bunn and others, 2014; Whitcher, 2013) was used to express the annual tree-ring data for each site in terms of additive frequency components or wavelet voices (fig. 5). Because the precipitation data were smoothed using a 12-year window, the high-frequency wavelet voices (D1, D2, and D3, fig. 5), corresponding to wavelengths of 2, 4, and 8 years, were not used in the analysis. Also, because the tree-ring chronologies were not long enough to have confidence in the D7 wavelength (128 years), D7 was not used in the analysis; therefore, for all four tree-ring chronologies, three wavelet voices (D4, D5, and D6), corresponding to wavelengths of 16, 32, and 64 years, were used to estimate precipitation. Thus, there were 12 potential explanatory variables (plus an intercept) used to model each of the 15 yearly precipitation time series. The calibration period (the time interval for which both tree-ring and precipitation data were available) extended from 1888, 1889, or 1890 (depending on the precipitation group) to 1990, the year shortly after which most of the tree-ring chronologies ended. The beginning of the hindcast period (the period during which only tree-ring data were available) was chosen to be 1700. Although three of the tree-ring chronologies extended well back into the 1600s, the Boundary Bog chronology, which began about 1700, turned out to be the most frequently used explanatory variable.

As described in Ryberg (2015), all-subsets regression along with extensive model selection and verification criteria were used to select the best models for explaining variability in each of the precipitation time series based on the tree-ring wavelet voices. To reduce serial correlation, the regression

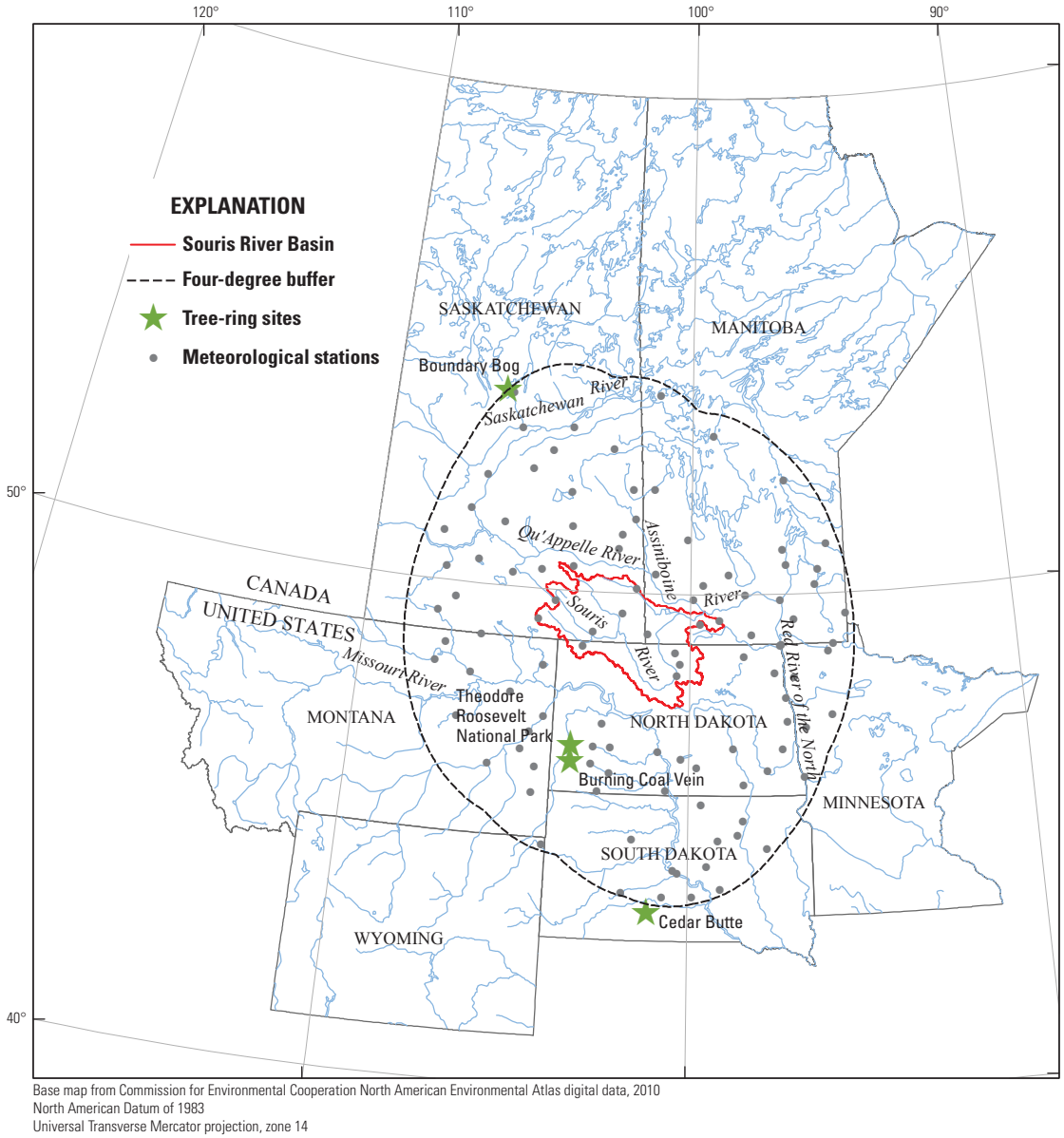

Base map from Commission for Environmental Cooperation North American Environmental Atlas digital data, 2010
North American Datum of 1983
Universal Transverse Mercator projection, zone 14

Figure 3. Study area boundary (four-degree buffer around Souris River Basin), meteorological stations, and potential tree-ring sites used for long-term climate analysis. Modified from Ryberg (2015).

models were based on thinned (every fourth year) values of the annual time series.

Climate Variability Results

The regression analysis for estimating the smoothed yearly precipitation data for each season and cluster based on the tree-ring data indicated that, with few exceptions, the tree-ring wavelet voices for the selected sites explained most of the multidecadal variability in seasonal precipitation (table 5.1 in Ryberg, 2015). The regression models explained more than 60 percent of the variability in precipitation (based on the adjusted coefficient of determination) for cluster 1 (all 3 seasons), cluster 2 (seasons 1 and 3), cluster 3 (season 1), cluster 4 (seasons 1 and 3), and cluster 5 (all 3 seasons); and many of these models explained more than 80 percent of the variability. Of the remaining models, the models for cluster 2 (season 2) and cluster 4 (season 2) explained 58 and 54 percent, respectively, of the variability. Only cluster 3 (seasons 2 and 3) had a relatively low coefficient of determination (32 and 45 percent, respectively), and these were the only models that failed the regression diagnostic tests; therefore, with the exception of cluster 3 (seasons 2 and 3), the tree-ring chronologies were good predictors of seasonal precipitation for all five clusters. The most frequently used explanatory variables included wavelet voice D6 for Burning Coal Vein (10 models),

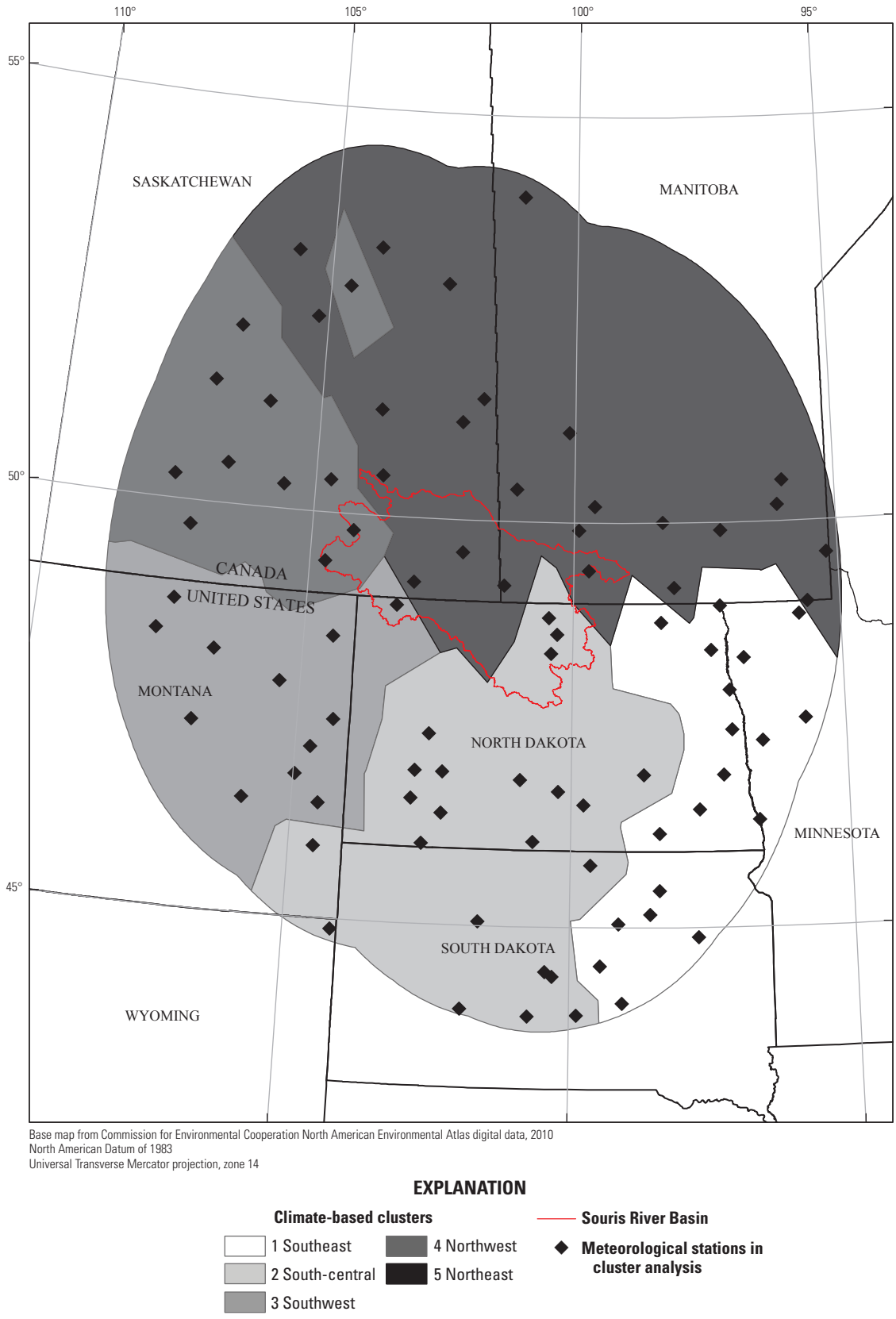

Figure 4. The five clusters of meteorological stations in the study area. Modified from Ryberg (2015).

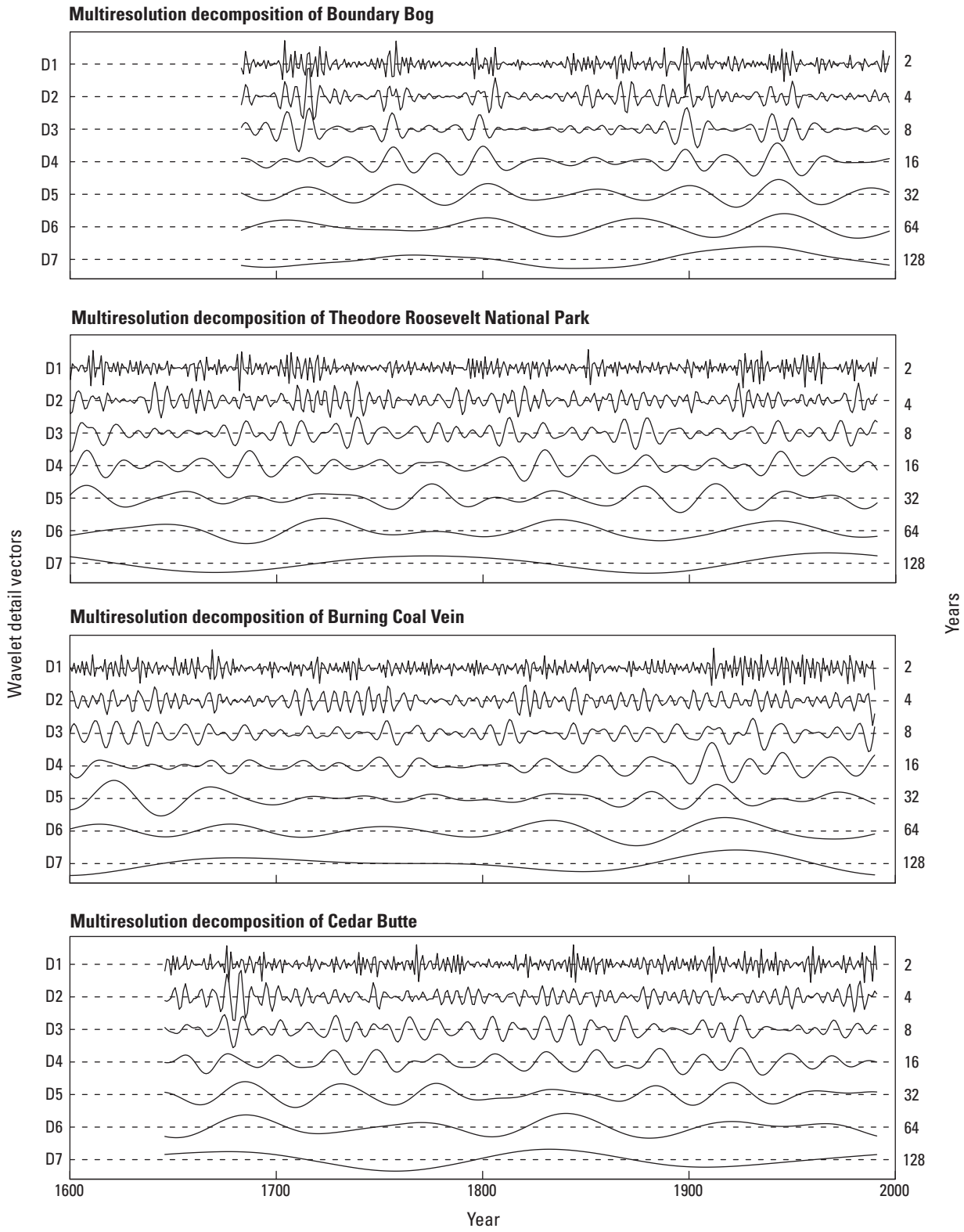

Figure 5. Multiresolution decomposition of tree-ring chronologies used in the climate analysis. Modified from Ryberg (2015).

Boundary Bog (8 models), and Theodore Roosevelt National Park (8 models); and wavelet voice D5 for Cedar Butte (9 models), Boundary Bog (8 models), and Theodore Roosevelt National Park (6 models).

The extended precipitation time series for cluster 1 (southeast) and season 2 (March–June) is shown in figure 6 along with the observed precipitation data. The coefficient of determination for this model was 62 percent (based on the thinned data). Observed season 2 precipitation for this group was highest at the end of the record (about 1993 to present) and during about 1890–1910. Similar (in magnitude) but longer duration wet periods were seen about 1820–50 and 1740–70. There were two extreme (compared to the observed record) season 2 droughts during the 1860s and early 1700s. These extreme wet and dry periods prior to the precipitation record were confirmed in Ryberg (2015) based on historical information and comparison with other paleoclimatic studies from the region.

The extended precipitation time series for cluster 5 (northeast) and season 3 (July–October) is shown in figure 7 along with the observed 12-year moving average precipitation data. The coefficient of determination for this model was 81 percent. Observed 12-year moving average precipitation for this season is extremely high from about 1980 to present, remaining well above previously recorded precipitation. A shift toward higher summer and fall precipitation in about 1980 has been documented in a number of previous studies in the southeastern part of the study area and elsewhere in the north-central United States and south-central Canada (Garbrecht and Rossel, 2002; Shapely and others, 2005; Vecchia, 2008; Small and Islam, 2008). Based on figure 7, this recent wet summer/fall period extends well into southern Manitoba and southeastern Saskatchewan, including a large part of the Souris River Basin (fig. 4). The extended precipitation record indicates a similar (though perhaps shorter duration) wet period during about 1830–50 and another extreme wet period during the early 1700s (fig. 7). Extreme dry summer/fall conditions are indicated during the 1740s and 1790s, and these droughts are similar to the drought of the 1930s (fig. 7). These extreme wet and dry periods, indicated by the extended precipitation data, were verified in Ryberg (2015) based on historical information and comparison with other paleoclimatic studies.

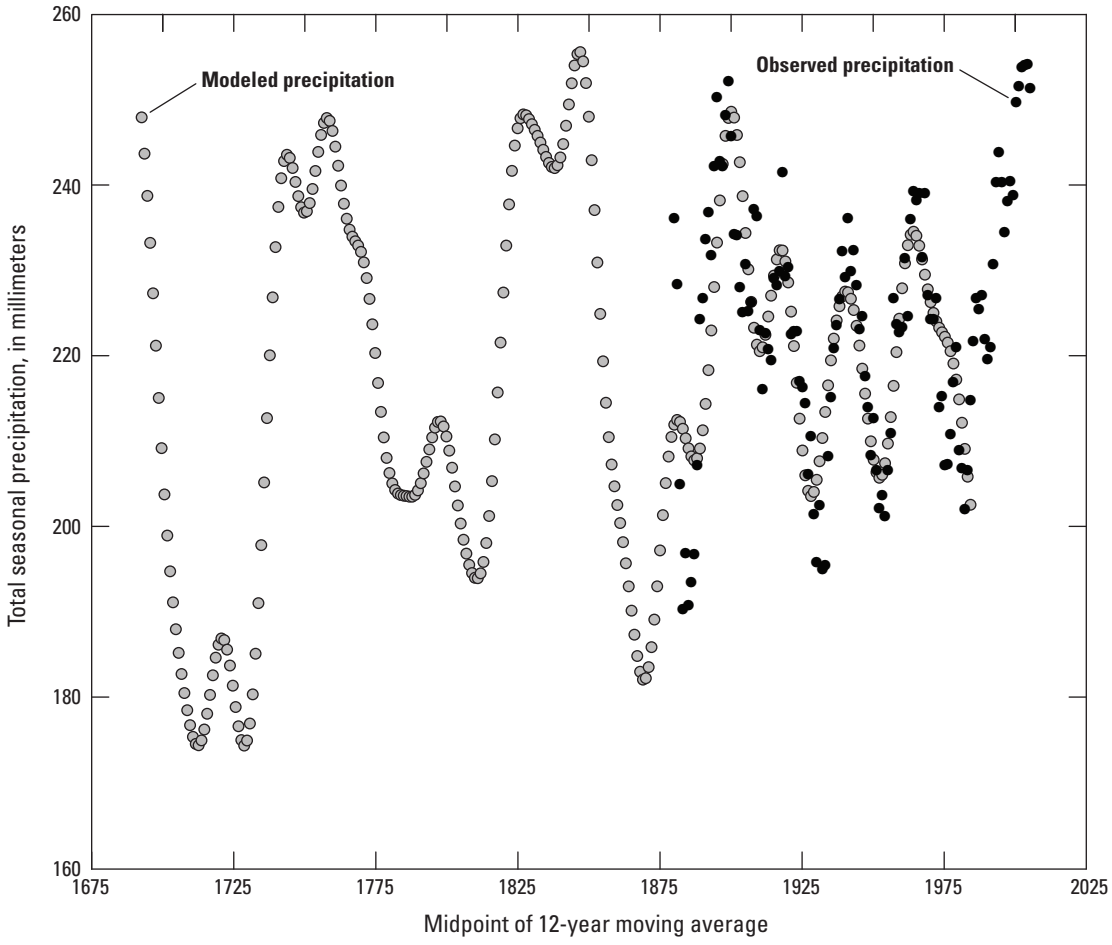

Figure 6. Modeled and observed 12-year moving average precipitation for cluster 1 (southeast, representing much of the Red River of the North Basin in the United States), season 2 (March-June).

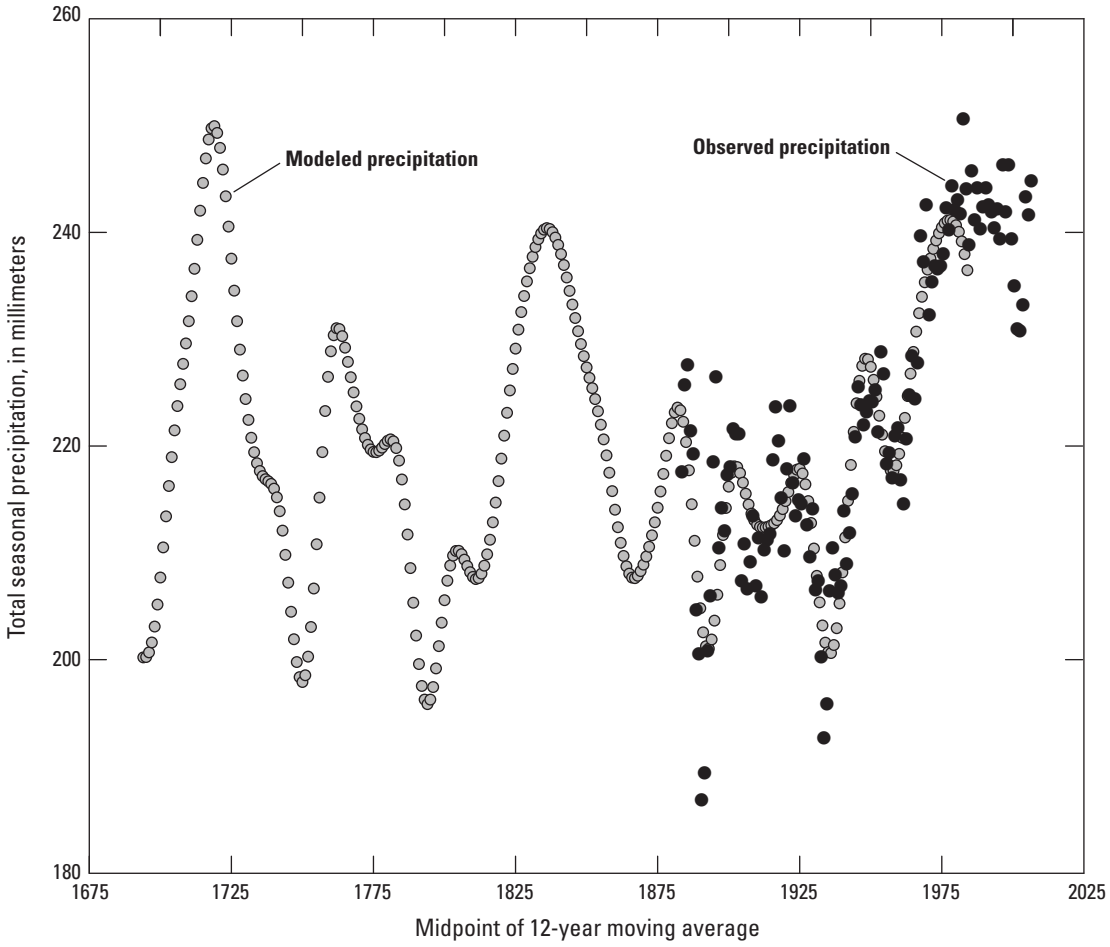

Figure 7. Modeled and observed 12-year moving average precipitation for cluster 5 (northeast, representing southern Manitoba and southeastern Saskatchewan), season 3 (July–October).

Stochastic Climate Model for Simulation of Precipitation, Temperature, and Potential Evapotranspiration

The water-balance model for estimating natural streamflow, described in subsequent sections of this report, uses monthly precipitation, temperature, and PET to estimate runoff from selected headwater basins and intervening subbasins of the Souris River Basin. The water-balance model was calibrated and verified using historical climate inputs and streamflow data; however, the objective of this study is to generate potential future streamflow. Therefore, a stochastic climate model was developed to simulate future precipitation, temperature, and PET over the Souris River Basin that reproduces both the short-term variability in the historical meteorological records and the long-term variability in the extended tree-ring precipitation records. The stochastic climate simulation model is described in this section.

Data and Methods

The meteorological data described previously in the section "Analysis of Long-term Climate Variability" were examined to select stations in and near the Souris River Basin with complete or nearly complete records of monthly precipitation and average temperature for 1912–2011. The starting year (1912) was selected because many of the stations had missing or partially missing records prior to that date. The large areal extent of the regions used previously (fig. 4) contained many stations and thus spatial averages over the regions could be estimated for earlier years despite missing records for some stations; however, for this analysis it was important to use stations in and closely surrounding the Souris River Basin, and the stations needed to have a common period of record. There were 27 stations closest to the basin that were initially considered (fig. 8). Of these stations, 16 had continuous records for 1912–2011. The 16 continuous-record sites were split into 4 station groups of 4 stations each (fig. 8). Note that the station groups defined here differ from the clusters defined in the previous section of this report. This grouping of stations was

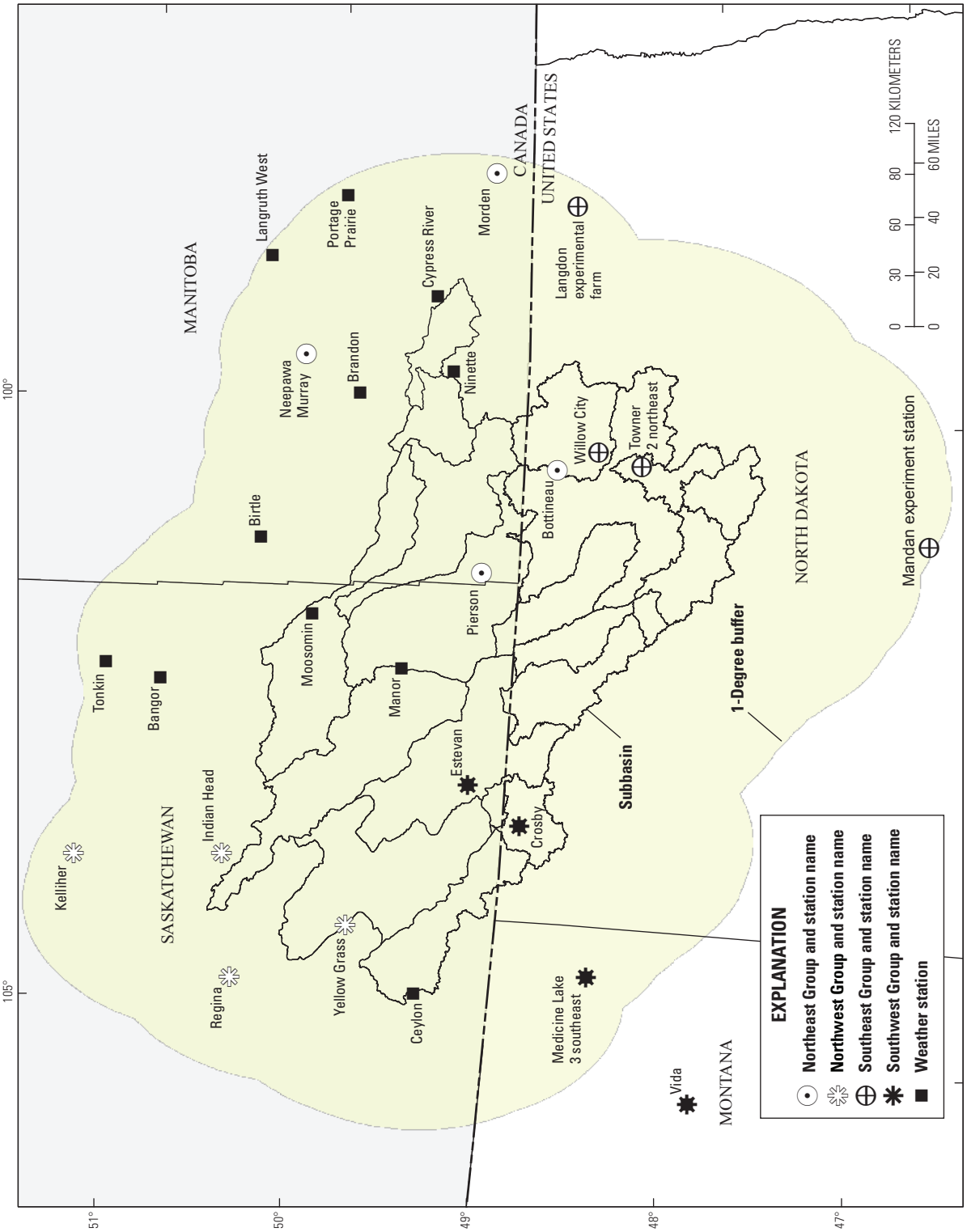

Figure 8. Locations of meteorological stations in and near the Souris River Basin, including station groups used to develop the stochastic climate simulation model for precipitation, temperature, and potential evapotranspiration (northeast, northwest, southeast, and southwest groups) and additional stations used for calibrating the water-balance model.

the most compact set of stations with continuous record that was sufficient to generate the climatic inputs required for the water-balance model. Some of these stations had occasional missing values but none had large (greater than 1 year) periods of missing data.

Monthly PET values were estimated using the Hamon method (Lu and others, 2005; Huffman and others, 2011) and modified as described in the following section "Water-Balance Model for Estimating Natural Streamflow" of this report. The Hamon method estimates PET as a function of monthly average temperature, position (latitude), and time of year (radiation as it relates to declination of the Earth). For a given spatial position and month, PET computed using this method is a one-to-one, monotonically increasing function of monthly average temperature; therefore, because monthly temperature can be computed directly from monthly PET, the stochastic climate simulation model was developed for precipitation and PET. Temperature, which is required for the snowmelt algorithm used in the water-balance model, was computed directly from PET as described later in the section "Stochastic Natural Streamflow Model" of this report.

The stochastic climate model for simulating monthly precipitation and PET for the 16 sites contained in the groups shown in figure 8 was developed in two stages. First, a model was developed for group-averaged seasonal data for each of the four station groups and the same three seasons used in the section "Analysis of Long-Term Climate Variability." Then, the group-averaged seasonal data were disaggregated, as described later in the section "Stochastic Natural Streamflow Model," to obtain monthly values for individual sites. The group-averaged seasonal data is designated as

$$PET_{G,S}(y); P_{G,S}(y) \tag{1}$$

where

$PET_{G,S}(y)$ is the potential evapotranspiration for station group G, season S, and year y;

$P_{G,S}(y)$ is the precipitation for station group G, season S, and year y;

G equals 1 (southeast), 2 (southwest), 3 (northwest), and 4 (northeast);

S equals 1 (November–February), 2 (March–June), and 3 (July–October); and

y equals 1912, 1913, …, 2011.

Henceforth, the variables in equation 1 will be referred to as time series variables. The first step in the analysis was to transform each of these 24 time series variables (2 climate variables times 4 groups times 3 seasons) so that the transformed values had an approximate standard normal distribution. This was accomplished using power transformations:

$$ZPET = \frac{[PET - c]^r - M}{SD}; ZP = \frac{[P - c]^r - M}{SD}, \tag{2}$$

where

$ZPET$ is the transformed value of PET;

ZP is the transformed value of P;

c and r are the transformation parameters;

M is the sample mean, values provided in table 1; and

SD is the sample standard deviation, values provided in table 1.

The transformation parameters (table 1) were selected as follows. For c=0, values r=1, 1/2, 1/3, 1/4, and 1/5 were applied, and the value for which the skewness coefficient of the transformed data was closest to zero (in absolute value) was selected. The resulting values were r=1 (no transformation) for PET for season 3 and r=1/3 (season 1) or r=1/2 (seasons 2 and 3) for P. For PET during seasons 1 and 2, the skewness coefficient was positive and did not approach zero as r was decreased. In those cases, c=10 was used for season 1 and c=100 for season 2, and the value r=1/4 resulted in a skewness coefficient close to zero. The M and SD are the sample means and standard deviations of the transformed variables for 1912–2011. Normal probability plots of $ZPET$ and ZP were examined and in all cases the standard normal approximation was deemed adequate.

The next step in the model development was to use principal components analysis to evaluate spatial patterns in the transformed time series variables that could be used to simplify the model. For each season, principal components are linear combinations of the time series variables over the station groups; for example, for PET, the principal components can be expressed as

$$ZPET^*_{j,S}(y) = \sum_{G=1}^{4} a_{jG} ZPET_{G,S}(y), \quad \text{for } j = 1,2,3,4 \tag{3}$$

$$Corr\{ZPET^*_{j,S}(y), ZPET^*_{k,S}(y)\} = 0, j \neq k \tag{4}$$

$$\begin{aligned} &Var\{ZPET^*_{1,S}(y)\} > Var\{ZPET^*_{2,S}(y)\} \\ &> Var\{ZPET^*_{3,S}(y)\} > Var\{ZPET^*_{4,S}(y)\} \end{aligned} \tag{5}$$

$$\sum_{j=1}^{4} Var\{ZPET^*_{j,S}(y)\} = \sum_{G=1}^{4} Var\{ZPET_{G,S}(y)\} \tag{6}$$

where

$ZPET^*_{j,S}(y)$ is the transformed value of PET for principal component j, season S, and year y;

$ZPET_{G,S}(y)$ is the transformed value of PET for station group G, season S, and year y; and

a_{jG} is the coefficient for principal component j and station group G.

The coefficients of the principal components (a in eq. 3) are computed such that the components are mutually uncorrelated (eq. 4), the variance of the components decreases as the component number (j) increases (eq. 5), and the total variance of the principal components equals the total variance

Table 1. Transformation parameters for time series variables used in the stochastic climate simulation model.

[*c* and *r*, transformation parameters defined in equation 2; *M*, sample mean; *SD*, sample standard deviation; SE, southeast; SW, southwest; NW, northwest; NE, northeast]

Season	Group	Potential evapotranspiration				Precipitation			
		c	*r*	*M*	*SD*	*c*	*r*	*M*	*SD*
1	SE	10	0.25	2.24	0.13	0	0.33	3.61	0.47
	SW	10	0.25	2.30	0.14	0	0.33	3.64	0.43
	NW	10	0.25	2.10	0.16	0	0.33	4.50	0.41
	NE	10	0.25	2.17	0.14	0	0.33	4.32	0.44
2	SE	100	0.25	3.26	0.12	0	0.5	13.48	2.01
	SW	100	0.25	3.31	0.13	0	0.5	12.93	2.08
	NW	100	0.25	3.14	0.13	0	0.5	13.63	2.17
	NE	100	0.25	3.25	0.12	0	0.5	14.12	1.99
3	SE	0	1.0	301.7	17.5	0	0.5	13.66	1.90
	SW	0	1.0	309.0	18.7	0	0.5	12.32	1.75
	NW	0	1.0	274.5	16.9	0	0.5	13.60	1.89
	NE	0	1.0	298.5	17.3	0	0.5	14.53	1.90

Table 2. Results of principal components analysis for time series variables used in the stochastic climate simulation model.

[PC, principal component; SE, southeast; SW, southwest; NW, northwest; NE, northeast]

Season	PC number	Potential evapotranspiration					Precipitation				
		Variance	Coefficients for station groups				Variance	Coefficients for station groups			
			SE	SW	NW	NE		SE	SW	NW	NE
1	1	3.84	0.50	0.50	0.50	0.50	2.71	0.48	0.51	0.50	0.51
	2	0.07	0	-0.77	0.16	0.62	0.56	0.72	-0.22	-0.64	0.16
	3	0.04	-0.64	0	0.75	-0.16	0.44	-0.19	-0.69	0.19	0.67
	4	0.01	-0.58	0.40	-0.40	0.59	0.25	-0.46	0.47	-0.56	0.51
2	1	3.77	0.50	0.50	0.50	0.50	2.93	0.50	0.50	0.47	0.53
	2	0.10	0.48	-0.47	-0.53	0.51	0.59	0.59	-0.34	-0.65	0.34
	3	0.06	-0.30	-0.65	0.62	0.33	0.32	-0.11	-0.77	0.50	0.39
	4	0.02	0.65	-0.34	0.30	-0.61	0.12	0.63	-0.22	0.32	-0.67
3	1	3.74	0.51	0.49	0.47	0.53	2.76	0.51	0.51	0.45	0.53
	2	0.16	0.50	-0.41	-0.62	0.45	0.65	0.51	-0.27	-0.72	0.38
	3	0.08	0	-0.75	0.61	0.22	0.34	0.23	-0.81	0.53	0.10
	4	0.04	0.70	-0.13	0.15	-0.68	0.21	0.65	0.11	0	-0.75

of the original data (eq. 6). The statistical software R function "princomp" (R Core Team, 2015) was used to evaluate principal components for each season, and the results are given in table 2. For both *ZPET* and *ZP* and all three seasons, the first principal component (PC1) consisted of the average of all four station groups (multiplied by a constant). PC1 explained almost all (about 95 percent) of the variability for *ZPET* and most the variability (from 67 to 73 percent) for *ZP*. The second principal component (PC2) was similar for all three seasons and both *ZPET* and *ZP* and consisted of a weighted average of the eastern groups minus a weighted average of the western groups, or an east-west contrast. PC2 explained less than 4 percent of the variability for *ZPET* and from about 14 to 16 percent of the variability for *ZP*. The third principal component (PC3) also was similar for all three seasons and both *ZPET* and *ZP* and consisted of a weighted

average of the northern groups minus a weighted average of the southern groups, or a north-south contrast. PC3 explained less than 2 percent of the variability for *ZPET* and from about 8 to 11 percent of the variability for *ZP*. The fourth principal component (PC4) explained less than 1 percent of the variability for *ZPET* and less than 6 percent of the variability for *ZP*.

Based on the results presented in the previous paragraph, a model for the first three principal components for both *ZPET* and *ZP* was developed. Although, for *ZPET*, the second and third components explain a small part of the variability, these components were included because they were similar (in terms of the coefficients) to those for *ZP* and were important for maintaining cross-correlation between *ZPET* and *ZP*. PC4 is not included in any of the subsequent plots. PC4 was assumed to consist of white noise (independently distributed normal random variables) with mean zero and variance given by the corresponding values from table 2. In the simulation model described later in this section, all four principal components needed to be generated in order to be able to back-compute *ZPET* and *ZP* from the principal components.

Time series plots of the first three principal components for each of the seasons are shown in figures 9–11. A stochastic model needed to be developed to jointly simulate these 18 time series variables (in addition to the 6 variables for PC4, which were simulated as described in the previous paragraph). The model needed to reproduce the statistical properties of the data, including any important correlations between values from one season to the next or between values for PET and

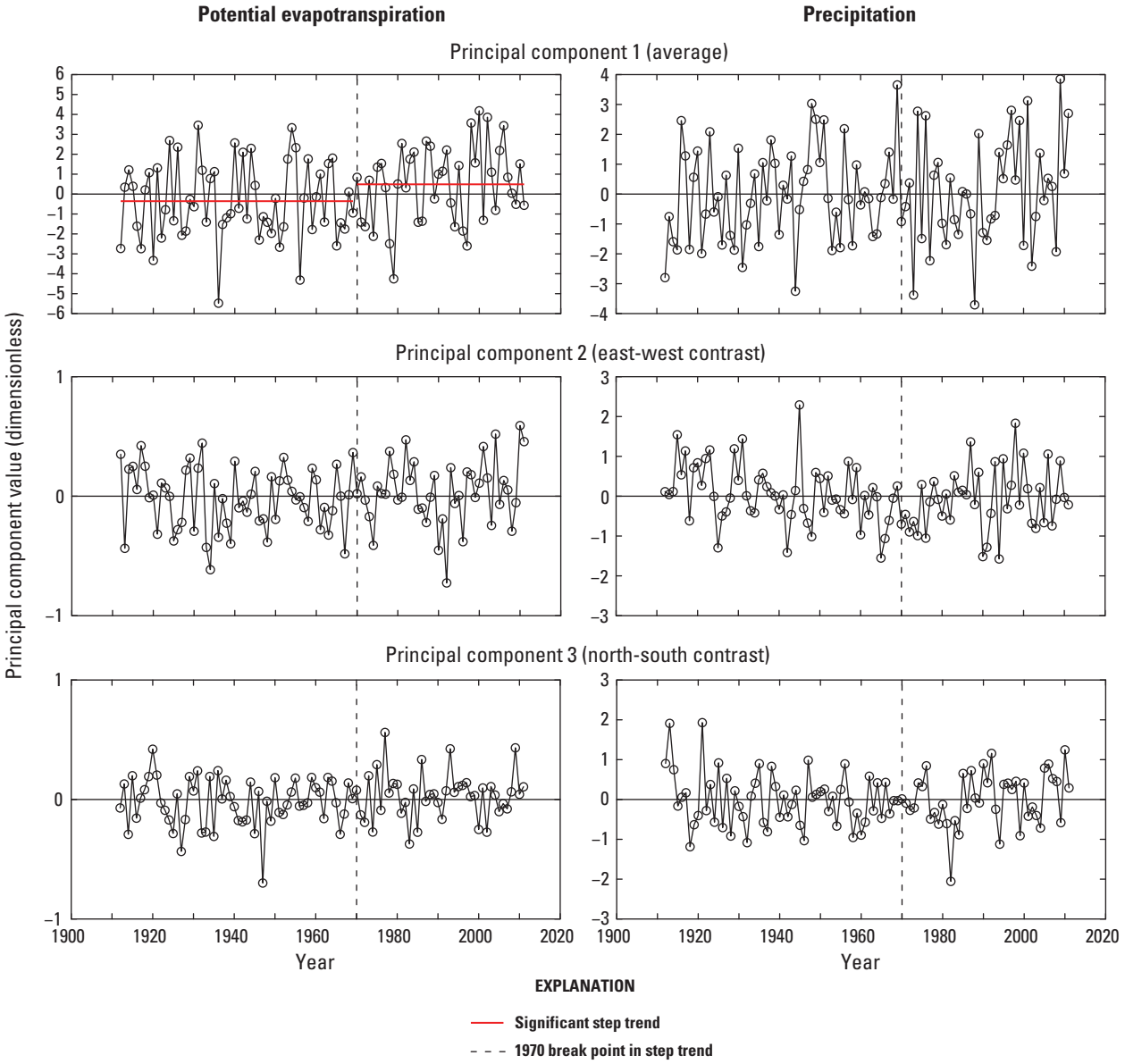

Figure 9. Time series plots of principal components for potential evapotranspiration and precipitation for season 1 (November–February), 1912–2011.

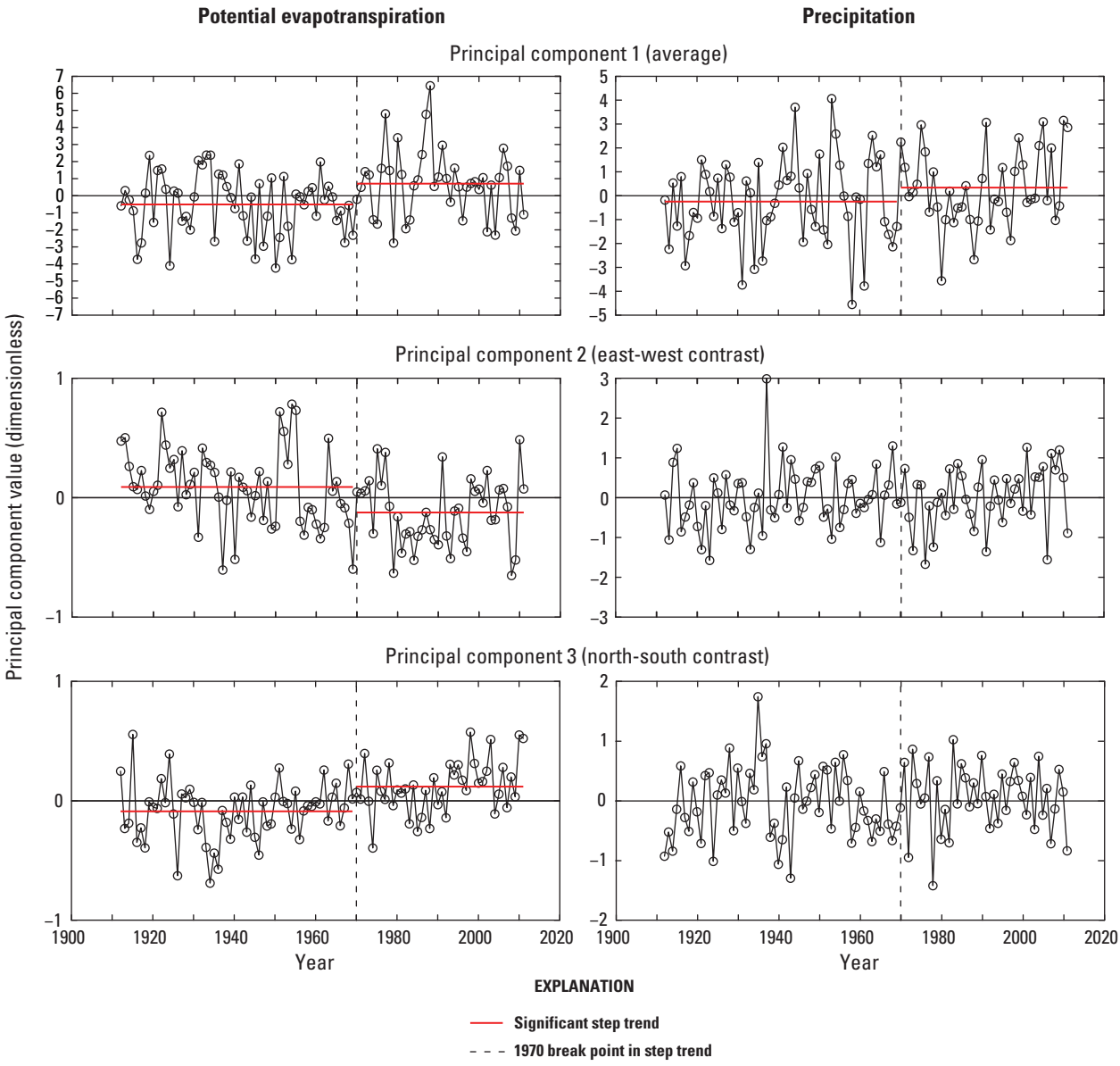

Figure 10. Time series plots of principal components for potential evapotranspiration and precipitation for season 2 (March–June), 1912–2011.

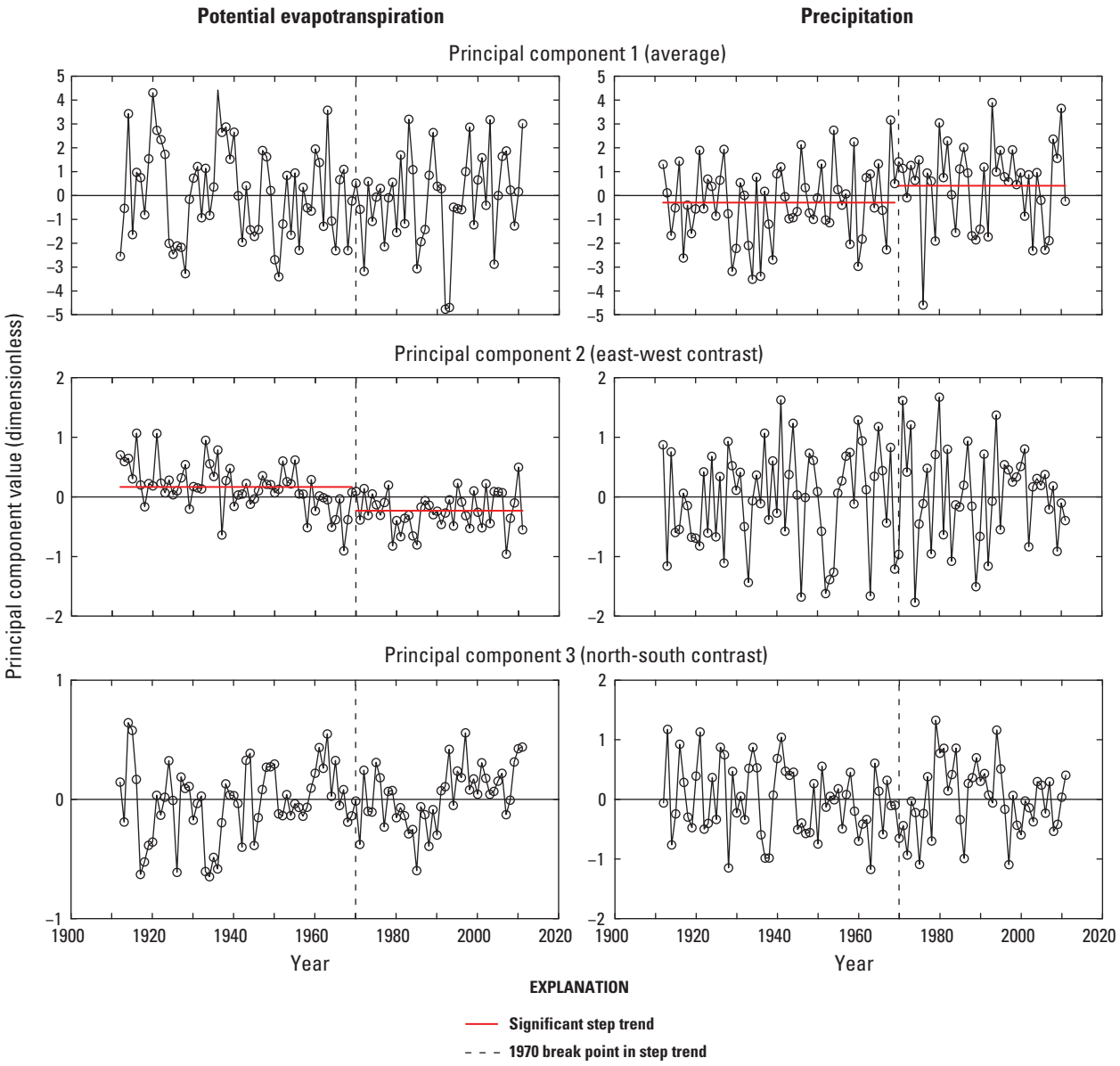

Figure 11. Time series plots of principal components for potential evapotranspiration and precipitation for season 3 (July–October), 1912–2011.

precipitation. The model also needed to reproduce any nonstationarity (such as trends in the mean) or long-range dependence (small deviations of the central tendency from zero that persist for long periods of time before reversing direction). Based on the climate analysis described in the section "Analysis of Long-Term Climate Variability" in this report, and on previous studies from the Devils Lake Basin in North Dakota (Bluemle, 1996; Wiche and others, 2000; Vecchia, 2002, 2008; Hoerling and others, 2010), the Red River of the North Basin (Rannie, 1998; St George and Nielson, 2003), and elsewhere (St George and Neilson, 2002; Shapely and others, 2005; Ryberg and others, 2014; Yonetani and Gordon, 2001), there seems to be strong support for long-range dependence; however, evidence for trends or permanent changes has not been firmly established for central North America (Milly and others, 2005; Hirsch and Ryberg, 2012; Ryberg and others, 2014). Of particular relevance to this study is evidence from the Devils Lake Basin, adjacent to and east of the Souris River Basin (fig. 1), in which an abrupt and highly significant increase in precipitation during summer and fall was seen in the late 1970s along with an increase in spring and summer lake evaporation, which is highly correlated with PET (Vecchia, 2008). Based on a comparison between simulated lake levels and 5,000 years of reconstructed lake levels from paleo lake studies (Murphy and others, 1997), Vecchia (2008) concluded that climate in the Devils Lake Basin had undergone abrupt transitions from "dry" to "wet" (such as was seen in the late 1970s) and "wet" to "dry," on average, about once every 150 years. The duration and timing of the transition periods are highly variable and seemingly random.

Because of the results for the Devils Lake Basin in Vecchia (2008), it was postulated that the Souris River Basin may have undergone a similar abrupt climate transition at about the same time; therefore, for each of the time series variables in figures 9–11, two-sample t-tests (Helsel and Hirsch, 2002) were used to test for step trends in the mean at three transition times: 1960, 1970, and 1980. There were several significant step trends in each case, but the trends were most significant for the 1970 transition time. This differed somewhat from Devils Lake, in which 1980 produced the most significant step trends; however, in either case the step trends may have taken place sometime between 1970 and 1980 with the exact year subject to speculation. The significant (*p*-value, or obtained significance level, less than 0.01) step trends for the 1970 transition time for this study are indicated by the red lines in figures 9–11. For PC1 (regional average of the four groups), there were significant uptrends in PET for season 1 (fig. 9), PET and precipitation for season 2 (fig. 10), and precipitation for season 3 (fig. 11). These trends are consistent with uptrends in precipitation and lake evaporation observed for the Devils Lake Basin and may be indicative of a large regional climate "shift" that was seen sometime during the early to late 1970s. There also was a significant downward step trend in PC2 (east-west contrast) and a significant upward trend in PC3 (north-south contrast) for PET for season 2 (fig. 10), indicating that the increase in PET was largest for the northern and western part of the region (that is, the NW group). For season 3 PET, there was a significant downtrend for PC2, despite no trend in PC1, which indicates that, although average PET for all four groups did not change, there were small increases in the southwest and northwest groups offset by small decreases in the southeast and northeast groups. The implications of these changes in terms of original (untransformed) PET and precipitation and their impact on the water balance will be discussed later in this section.

To simulate the principal component time series, the step changes described in the previous paragraph were subtracted out to obtain adjusted time series for each principal component:

$$\tilde{E}_{j,S}(y) = ZPET^{*}_{j,S}(y) - \alpha_{j,S}(y); \quad \tilde{P}_{j,S}(y) = ZP^{*}_{j,S}(y) - \beta_{j,S}(y) \tag{7}$$

$$\alpha_{j,S}(y) = A_{D;j,S} I_{1912 \le y \le 1969} + A_{W;j,S} I_{1970 \le y \le 2011} \tag{8}$$

$$\beta_{j,S}(y) = B_{D;j,S} I_{1912 \le y \le 1969} + B_{W;j,S} I_{1970 \le y \le 2011} \tag{9}$$

where

$\tilde{E}_{j,S}(y)$ is the adjusted value of *ZPET** for principal component *j*, season *S*, and year *y*;

$\alpha_{j,S}(y)$ is the step change indicator for *ZPET**;

$A_{D;j,S}$ is the step change coefficient for $\tilde{E}_{j,S}(y)$ for the dry period *D*, principal component *j*, and season *S*;

$A_{W;j,S}$ is the step change coefficient for $\tilde{E}_{j,S}(y)$ for the wet period *W*, principal component *j*, and season *S*;

$I_{1970 \le y \le 2011}$ is 1 for years 1912–69 and zero otherwise;

$I_{1970 \le y \le 2011}$ is 1 for years 1970–2011 and zero otherwise;

$\tilde{P}_{j,S}(y)$ is the adjusted value of *ZP** for the principal component *j*, season *S*, and year *y*;

$\beta_{j,S}(y)$ is the step change indicator for *ZP**;

$B_{D;j,S}$ is the step change coefficient for $\beta_{j,S}(y)$ for the dry period *D*, principal component *j*, and season *S*; and

$B_{W;j,S}$ is the step change coefficient for $\beta_{j,S}(y)$ for the wet period *W*, principal component *j*, and season *S*.

The values for the step change coefficients ($A_{D;j,s}$, $A_{W;j,s}$, $B_{D;j,s}$, $B_{W;j,s}$) are either zero (if there was no significant change) or the mean of the variable for the appropriate time period (if the change was significant). Subscript *D* refers to the "dry" period (1912–69) and subscript *W* refers to the "wet" period (1970–2011). A time series model was developed for simulating the adjusted time series. A separate model was used for simulating the step change indicators, which were then added back into the adjusted time series as described later in this section.

For each principal component number (j=1, 2, or 3), the six adjusted time series variables (eq. 7) were modeled using a multivariate, periodic autoregressive model (McLeod, 1994). In this model, the variables were ordered in the following sequence:

$$\ldots, \tilde{P}_{j,3}(y-1), \tilde{E}_{j,3}(y-1), \tilde{P}_{j,1}(y), \tilde{E}_{j,1}(y), \tilde{P}_{j,2}(y),$$
$$\tilde{E}_{j,2}(y), \tilde{P}_{j,3}(y), \tilde{E}_{j,3}(y), \tilde{P}_{j,1}(y+1), \tilde{E}_{j,1}(y+1), \ldots$$

and each variable was predicted using antecedent values in the sequence up to a maximum lag of 1 year (3 seasons); for example, $\tilde{P}_{j,3}(y)$ was predicted using potential predictor variables $\tilde{P}_{j,3}(y-1), \tilde{E}_{j,3}(y-1), \tilde{P}_{j,1}(y), \tilde{E}_{j,1}(y), \tilde{P}_{j,2}(y), \tilde{E}_{j,2}(y)$. The coefficients of the prediction equations were assumed to change from season to season but repeat themselves from year to year. The fitted model coefficients are given in table 3. For each model equation, a stepwise procedure was used, in which the single best antecedent predictor variable was selected. If the coefficient for that predictor variable was not significant ($p \geq 0.05$, where p is the p-value for the coefficient), there were no predictor variables included in that model equation, which was the case for one equation for PET (PC3, season 1) and six equations for precipitation (PC1, season 2; PC2, seasons 1 and 2; and PC3, all three seasons). The subscripted Z variables in the equations are independent, standard normal-random variables. If the single best predictor variable was significant ($p<0.05$), the second most significant variable (given the first was already included) was selected. If the second variable was not significant, the model with the single predictor variable was used. This was the case for five of the nine model equations for PET and three of the nine model equations for precipitation; for example, for PC1 and season 1, PET was negatively related to concurrent precipitation, and precipitation was positively related to precipitation from season 3 of the previous year. There were only three equations in which two predictor variables were included, all for PET. There were no equations with more than two predictor variables.

Table 3. Fitted multivariate periodic autoregressive models for adjusted principal component time series variables.

[PCj, jth principal component; $\tilde{E}_{j,S}$, adjusted time series variable for potential evapotranspiration for principal component j, season S; $\tilde{P}_{j,S}$, adjusted time series variable for precipitation for principal component j, season S; y, year; $Z_{E;j,S}$, independent standard normal random variable for potential evapotranspiration principal component j, season S; $Z_{P;j,S}$, independent standard normal random variable for precipitation principal component j, season S]

Principal component	Season	Potential Evapotranspiration	Precipitation
PC1	1	$\tilde{E}_{1,1}(y) = -0.63\tilde{P}_{1,1}(y) + 1.62Z_{E;1,1}$	$\tilde{P}_{1,1}(y) = 0.25\tilde{P}_{1,3}(y-1) + 1.60Z_{P;1,1}$
	2	$\tilde{E}_{1,2}(y) = -0.30\tilde{P}_{1,2}(y) + 0.17\tilde{E}_{1,1}(y) + 1.78Z_{E;1,2}$	$\tilde{P}_{1,2}(y) = 1.71Z_{P;1,2}$
	3	$\tilde{E}_{1,3}(y) = -0.41\tilde{P}_{1,3}(y) + 1.82Z_{E;1,1}$	$\tilde{P}_{1,3}(y) = 0.21\tilde{P}_{1,2}(y) + 1.59Z_{P;1,3}$
PC2	1	$\tilde{E}_{2,1}(y) = 0.11\tilde{P}_{2,1}(y) + 0.25Z_{E;2,1}$	$\tilde{P}_{2,1}(y) = 0.75Z_{P;2,1}$
	2	$\tilde{E}_{2,2}(y) = -0.12\tilde{P}_{2,2}(y) + 0.19\tilde{E}_{2,3}(y-1) + 0.28Z_{E;1,2}$	$\tilde{P}_{2,2}(y) = 0.77Z_{P;2,2}$
	3	$\tilde{E}_{2,3}(y) = 0.45\tilde{E}_{2,2}(y) + 0.33Z_{E;2,3}$	$\tilde{P}_{2,3}(y) = 0.23\tilde{P}_{2,2}(y) + 0.79Z_{P;2,3}$
PC3	1	$\tilde{E}_{3,1}(y) = 0.20Z_{E;3,1}$	$\tilde{P}_{3,1}(y) = 0.66Z_{P;3,1}$
	2	$\tilde{E}_{3,2}(y) = -0.13\tilde{P}_{3,2}(y) + 0.31\tilde{E}_{3,3}(y-1) + 0.20Z_{E;3,2}$	$\tilde{P}_{3,2}(y) = 0.57Z_{P;3,2}$
	3	$\tilde{E}_{3,3}(y) = 0.67\tilde{E}_{3,2}(y) + 0.24Z_{E;3,3}$	$\tilde{P}_{3,3}(y) = 0.58Z_{P;3,3}$
PC4	1	$\tilde{E}_{4,1}(y) = 0.09Z_{E;4,1}$	$\tilde{P}_{4,1}(y) = 0.50Z_{P;4,1}$
	2	$\tilde{E}_{4,2}(y) = 0.14Z_{E;4,2}$	$\tilde{P}_{4,2}(y) = 0.35Z_{P;4,2}$
	3	$\tilde{E}_{4,3}(y) = 0.19Z_{E;4,3}$	$\tilde{P}_{4,3}(y) = 0.46Z_{P;4,3}$

Stochastic Simulation Results

To compare the short-term (annual to decadal) statistical properties of the simulated data to the observed data, the time series model was used to simulate 100 independent realizations of the time series variables for the dry (1912–69) and wet (1970–2011) periods. Each realization was the same length as the observed record for the respective dry or wet period. The time series model for the principal components (table 3) was used to generate the principal component time series. Then, the step changes (eq. 7) were added back in for either the dry or wet period. The principal components (eq. 3, table 2) were reversed (the coefficient matrix for each season was inverted and multiplied times the vector of principal components), and finally the transformations (eq. 2, table 1) were reversed to obtain simulated time series of PET and precipitation for each of the station groups and seasons, assuming either dry or wet conditions. Statistics computed from the 100 sets of simulated data were compared to corresponding statistics of the observed record (tables 4 and 5). The statistics included the mean, 10th percentile (Q10), and 90th percentile (Q90). The moisture deficit (precipitation minus PET) was used in place of PET because it is the most relevant variable from a water-balance perspective, and it includes the effects of cross-correlation between precipitation and PET. The annual total of the three seasons also is shown in tables 4 and 5. An 80-percent range is shown for the simulated realizations, which is the range between the 10th and 90th percentiles out of 100 simulated values.

For most of the statistics, the observed values were well within the 80-percent ranges from the simulated realizations, and the few that were outside of the ranges were close to the upper or lower limits (tables 4 and 5); therefore, the stochastic climate model was effective for reproducing the short-term variability of the precipitation and PET data for the three seasons and four station groups. Comparison of the dry and wet periods provides insight into the potential effects that changes in climatic conditions may have on the water-balance model simulations described in the "Stochastic Natural Streamflow Model" section of this report. For season 1 (November–February), the ranges from the simulations were nearly identical between the wet and dry periods. For season 2 (March–June) the precipitation statistics tended to be about 10 percent higher for all four station groups for the wet period compared to the dry period; however, when considering the combined effects of precipitation and PET, the deficits were similar for the wet and dry periods except for the northeast station group, for which deficits tended to be smaller (and surpluses larger) for the wet period. For season 3 (July–October), similar to season 2, the precipitation statistics tended to be about 10 percent higher for the wet period; however, unlike season 2, when considering the combined effects of precipitation and PET, the deficits tended to be lower for the wet period for all four station groups compared to the dry period. These lower summer and early fall deficits would be expected to increase runoff the following spring as less winter and spring precipitation would be required to replace the deficits. Taken in aggregate for the annual totals and the deficits, the dry years (indicated by Q10) tended to be less severe for the northeast group and slightly less severe for the remaining groups for the wet period compared to the dry period. The wet years (indicated by Q90) tended to be substantially wetter for the southeast, southwest, and northeast station groups for the wet period compared to the dry period.

In addition to reproducing the short-term variability of the observed climatic data, it is also important that the stochastic climate model is able to reproduce the long-term (multidecadal to century scale) variability. A 100-year observation period (1912–2011) may be much too short to evaluate probabilities of extreme events such as the 2011 spring rainfall amounts in the Souris River Basin, especially if climatic conditions are subject to long-range dependence.

Long-term precipitation variability was evaluated using 12-year moving averages, as was done in the previous section of this report "Analysis of Long-Term Climate Variability." An example of simulated 12-year moving average precipitation from the stochastic climate simulation model is shown in figure 12 for season 2 (March–June) and station group 1 (southeast). Although this station group is not the same as cluster 1 of the previous analysis (fig. 6), the long-term variability is expected to be similar to cluster 1. Assuming dry (1912–69) conditions, for the simulation shown in figure 12*A* there were 10 intervals during the 900-year simulation period for which the simulated 12-year moving average precipitation was less than the recorded low, including three very extreme (in both magnitude and duration) droughts comparable to the extreme early 1700s drought in figure 6. Conversely, there were only two short intervals for which simulated precipitation was higher than the recorded maximum and an 800-year period during which precipitation remained below the recorded maximum. Compared with figure 6, in which there were four extreme wet periods (two with long duration) during the 300-year extended period, the simulations produce far too few extreme wet periods; however, assuming wet (1970–2011) conditions (fig. 12*B*) this simulation produced six wet intervals more severe than the observed record and only three brief dry intervals comparable to the observed record.

Comparing figure 6 with figures 12*A* and 12*B*, it seems that the simulations assuming dry conditions reasonably represent the low extremes of the extended record and the simulations assuming wet conditions reasonably represent the high extremes. Moreover, the extended record was either well below or well above the long-term average (and not near the long-term average) for most of the 300-year extended record; thus, the extended record seems to suggest a mixture of alternating dry and wet conditions. As discussed previously in this section, strong evidence from the Devils Lake Basin in northeastern North Dakota indicates that alternating dry/wet conditions have been seen in that basin for thousands of years (Vecchia, 2008). It is reasonable to postulate that the same regional phenomenon is also responsible for alternating dry/wet conditions in the Souris River Basin; therefore, the

Table 4. Statistics of simulated and observed precipitation and moisture deficit (precipitation minus potential evapotranspiration) for dry (1912–69) period.

[All units are in millimeters; SE, southeast; SW, southwest; NW, northwest; NE, northeast; Annual, total of all three seasons; top number is for the observed record; numbers below represent the 10th and 90th percentiles from 100 simulated datasets]

Season	Group	Precipitation			Precipitation minus potential evapotranspiration		
		Mean	10th percentile	90th percentile	Mean	10th percentile	90th percentile
1	SE	53	32	86	18	-8	56
		46, 52	24, 31	66, 80	10, 18	-17, -6	33, 50
	SW	50	31	69	13	-9	40
		48, 53	27, 34	66, 80	9, 17	-17, -8	32, 46
	NW	98	65	131	69	34	104
		89, 97	58, 68	116, 132	60, 68	24, 35	88, 108
	NE	84	58	119	53	18	91
		78, 87	50, 58	106, 123	46, 56	13, 24	77, 94
2	SE	180	107	255	-31	-112	52
		171, 188	104, 127	229, 263	-42, -22	-116, -89	23, 61
	SW	167	98	230	-50	-132	29
		157, 175	90, 116	215, 252	-62, -41	-136, -107	2, 42
	NW	183	115	264	-9	-80	69
		170, 194	101, 128	238, 277	-23, 2	-102, -70	50, 93
	NE	195	122	268	-14	-91	47
		187, 206	117, 143	247, 283	-24, -1	-100, -71	40, 82
3	SE	180	125	234	-122	-190	-51
		173, 192	112, 132	228, 257	-132, -110	-205, -177	-68, -36
	SW	148	101	186	-159	-223	-98
		141, 154	90, 107	186, 212	-167, -153	-230, -211	-112, -86
	NW	183	113	262	-89	-167	13
		173, 187	110, 132	227, 258	-102, -85	-172, -147	-37, -5
	NE	206	143	254	-93	-157	-33
		195, 215	132, 156	255, 289	-107, -85	-182, -153	-35, -1
Annual	SE	413	315	495	-135	-227	-32
		392, 424	287, 332	484, 534	-160, -123	-274, -231	-53, 2
	SW	365	273	451	-196	-296	-91
		351, 377	258, 294	434, 478	-216, -183	-320, -281	-115, -67
	NW	465	348	597	-28	-150	111
		441, 473	331, 374	543, 596	-53, -19	-178, -130	59, 123
	NE	485	364	599	-54	-178	84
		468, 500	356, 405	569, 617	-75, -40	-197, -149	35, 91

Table 5. Statistics of simulated and observed precipitation and moisture deficit (precipitation minus potential evapotranspiration) for wet (1970–2011) period.

[All units are in millimeters; SE, southeast; SW, southwest; NW, northwest; NE, northeast; Annual, total of all three seasons; top number is for the observed record; numbers below represent the 10th and 90th percentiles from 100 simulated datasets]

Season	Group	Precipitation			Precipitation minus potential evapotranspiration		
		Mean	10th percentile	90th percentile	Mean	10th percentile	90th percentile
1	SE	49	22	75	12	-16	34
		46, 53	24, 32	67, 83	8, 16	-19, -8	33, 49
	SW	56	33	87	16	-14	53
		47, 54	27, 33	66, 79	6, 14	-21, -9	28, 44
	NW	97	65	133	65	26	103
		89, 98	58, 70	116, 134	57, 68	20, 36	88, 106
	NE	91	59	134	57	20	105
		79, 88	49, 60	104, 127	44, 54	9, 22	72, 96
2	SE	193	127	271	-25	-111	54
		184, 206	114, 143	242, 288	-35, -11	-113, -83	30, 82
	SW	178	115	251	-49	-118	32
		170, 193	102, 130	228, 272	-58, -33	-132, -103	3, 56
	NW	200	138	274	-6	-74	71
		189, 213	117, 144	251, 295	-19, 8	-99, -67	54, 102
	NE	216	164	301	-3	-62	86
		202, 225	129, 158	265, 308	-16, 9	-96, -66	52, 101
3	SE	204	135	268	-96	-172	-28
		190, 212	125, 154	250, 286	-110, -86	-185, -153	-42, -1
	SW	164	108	226	-148	-228	-79
		154, 172	102, 126	201, 230	-158, -137	-224, -197	-103, -68
	NW	196	143	254	-82	-141	-24
		186, 208	124, 153	243, 282	-91, -67	-164, -128	-32, 13
	NE	227	139	299	-71	-176	10
		216, 240	150, 178	277, 316	-81, -56	-162, -125	-12, 35
Annual	SE	447	348	549	-110	-226	21
		430, 464	316, 365	526, 581	-129, -90	-249, -199	-23, 39
	SW	398	302	508	-181	-279	-63
		377, 414	282, 325	460, 518	-203, -164	-316, -264	-100, -36
	NW	493	397	615	-23	-133	85
		473, 510	361, 411	564, 643	-43, -2	-169, -107	60, 142
	NE	533	436	647	-17	-127	73
		508, 542	395, 441	605, 674	-43, -4	-174, -121	69, 131

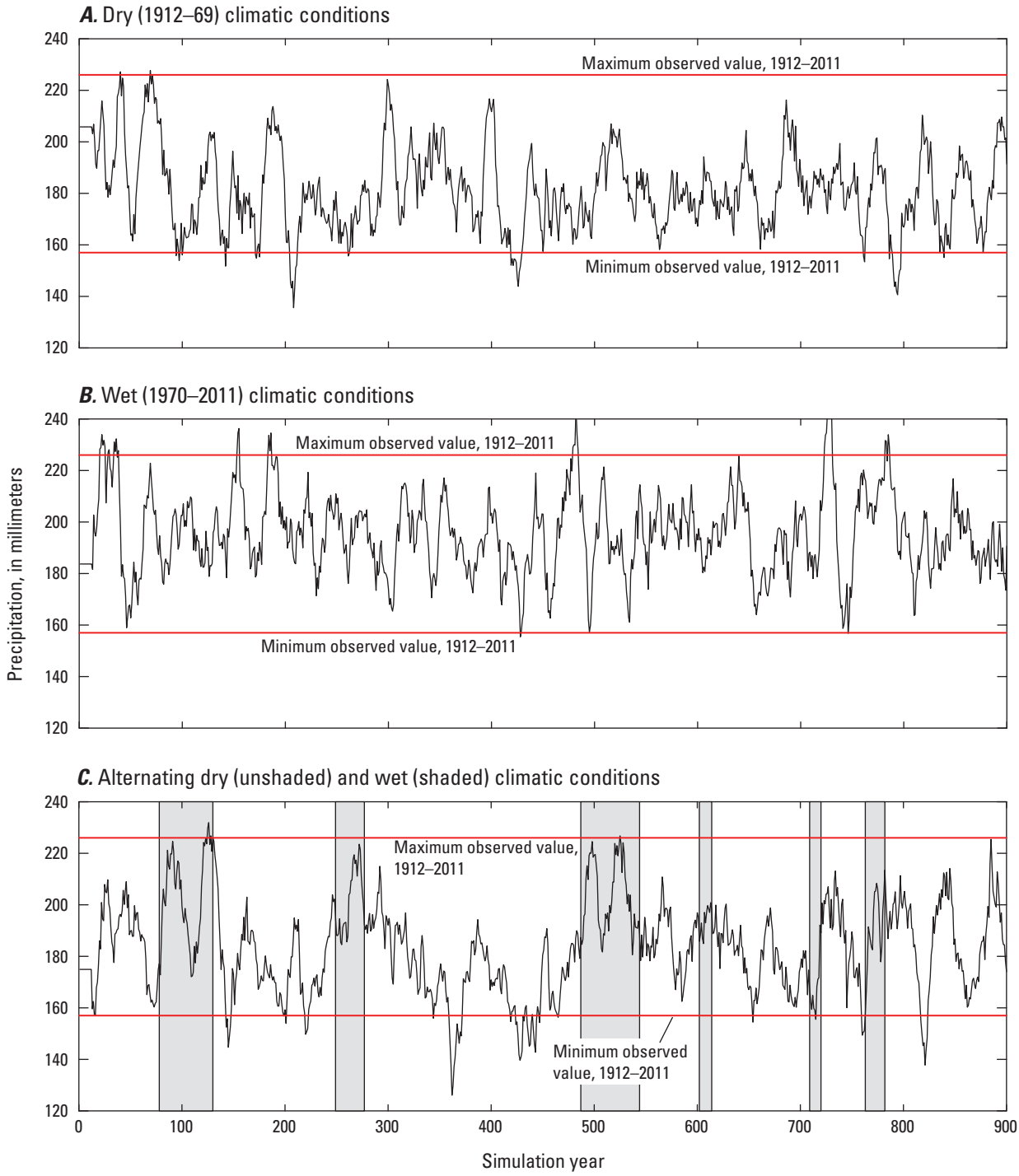

Figure 12. Long-term (900-year) simulated 12-year moving average precipitation for season 2 (March–June) and station group 1 (southeast). *A*, dry conditions. *B*, wet conditions. *C*, alternating dry/wet conditions.

same alternating long-term simulated climate states that were used for the Devils Lake simulation model (Vecchia, 2008), in which dry periods averaged 120 years in duration and wet periods 30 years in duration, were used to model the shifting climate states for the Souris River Basin. An example of simulated 12-year moving average precipitation with alternating dry/wet climate states is shown in figure 12*C*. In this example, there were six wet states with durations ranging from about 10 to 60 years interspersed with dry states ranging from about 50 to more than 200 years in duration. There were 9 severe droughts, 8 of which took place during dry states, and 6 major wet intervals (above 220 millimeters [mm]), 5 of which took place during wet states.

An example of simulated 12-year moving average precipitation from the stochastic climate simulation model is shown in figure 13 for season 3 (July–October) and station group 4 (northeast). Although this station group is not the same as cluster 5 of the previous analysis (fig. 7), the long-term variability is expected to be similar to cluster 5. Similar to the previous example with station group 1 (southeast) and season 2 (March – June), the simulation assuming dry conditions (fig. 13*A*) reproduces the extreme droughts of the extended record (fig. 7), and the simulation assuming wet conditions (fig. 13*B*) reproduces the extreme wet periods. The simulation with alternating dry/wet conditions (fig. 13*C*) has 9 severe droughts, 8 of which took place during dry states, and 4 prolonged wet periods (above 240 mm), 3 of which took place during wet states.

Water-Balance Model for Estimating Natural Streamflow

To convert stochastic estimates of precipitation, temperature, and PET into streamflow for flood risk analysis, evaluation of reservoir operation, and general simulation of future streamflow, a water-balance model (WBM) was developed such that three variables (precipitation, temperature, and PET), in conjunction with static basin properties (soil water storage and permeability), could be used to estimate monthly streamflow. The model was calibrated with historic (1946–2011) average monthly natural (unregulated) streamflow data provided by the U.S. Army Corps of Engineers (USACE) and with observed (gaged) streamflow for locations where observed flow was the same as natural flow. The natural streamflow data provided by the USACE was unregulated, which means the effects of Alameda, Rafferty, Boundary, and Lake Darling reservoirs/dams were removed; and streamflow was allowed to flow through the basin as it would have before the four reservoirs were installed. Once the WBM had been calibrated with the monthly natural streamflow, flows were then disaggregated into an approximately 10-day time step (three values per month).

Input Data for Water-Balance Model

The WBM requires three dynamic inputs (monthly precipitation, average temperature, and PET) and two static inputs (soil water storage and permeability) to simulate natural streamflow at selected streamflow-gaging stations (hereafter referred to as "gaging stations"). In order to determine the contributing area to selected gaging stations, basins were delineated using pre-defined basin delineations, online delineation tools, and (or) digital elevation models (DEMs). Calibration of the model relied heavily on streamflow estimates at various gaging stations throughout the Souris River Basin; therefore, selection of gaging stations with long and continuous streamflow records was critical.

Streamflow

Gaging stations were selected based on location and length of historical streamflow record. Streamflow data were retrieved from U.S. Geological Survey (2014b) and Water Survey of Canada (Government of Canada, 2014) online databases. A list of all gaging stations used to develop the WBM is provided in table 6 and figure 1.

In addition to observed streamflow, natural streamflow estimates from the USACE (U.S. Army Corps of Engineers, 2013) were used to calibrate the WBM. Natural streamflow is that streamflow that would have naturally occurred without the installation of the Boundary, Rafferty, Alameda, and Lake Darling Reservoirs (fig. 1). Natural streamflow does take into account the effects of the Des Lacs and J. Clark Salyer National Wildlife Refuges (NWRs; fig. 1), along with the effects of other minor hydraulic structures throughout the Souris River Basin, because these structures allow water to pass in a way that mimics natural streamflow patterns and are not operated for flood mitigation (U.S. Army Corps of Engineers, 2013). Natural flows were estimated through the use of five different flow routing methods: Null routing (direct routing), Muskingum routing, Muskingum Cunge routing, Lag routing, and Modified Puls routing (U.S. Army Corps of Engineers, 2013).

Watershed Delineation

Selected gaging stations were designated as outlet points, and contributing drainage areas were delineated resulting in the formation of 19 subbasins (both intervening and headwater basins) within the Souris River Basin (fig. 14). The four Manitoba gaging stations (05NF001, 05NG021, 05NG007, and 05NG001; fig. 14) downstream from the United States are not included in the following model development, but basin delineations for these gaging stations were developed for potential future extensions of the model from the international border to the basin outlet.

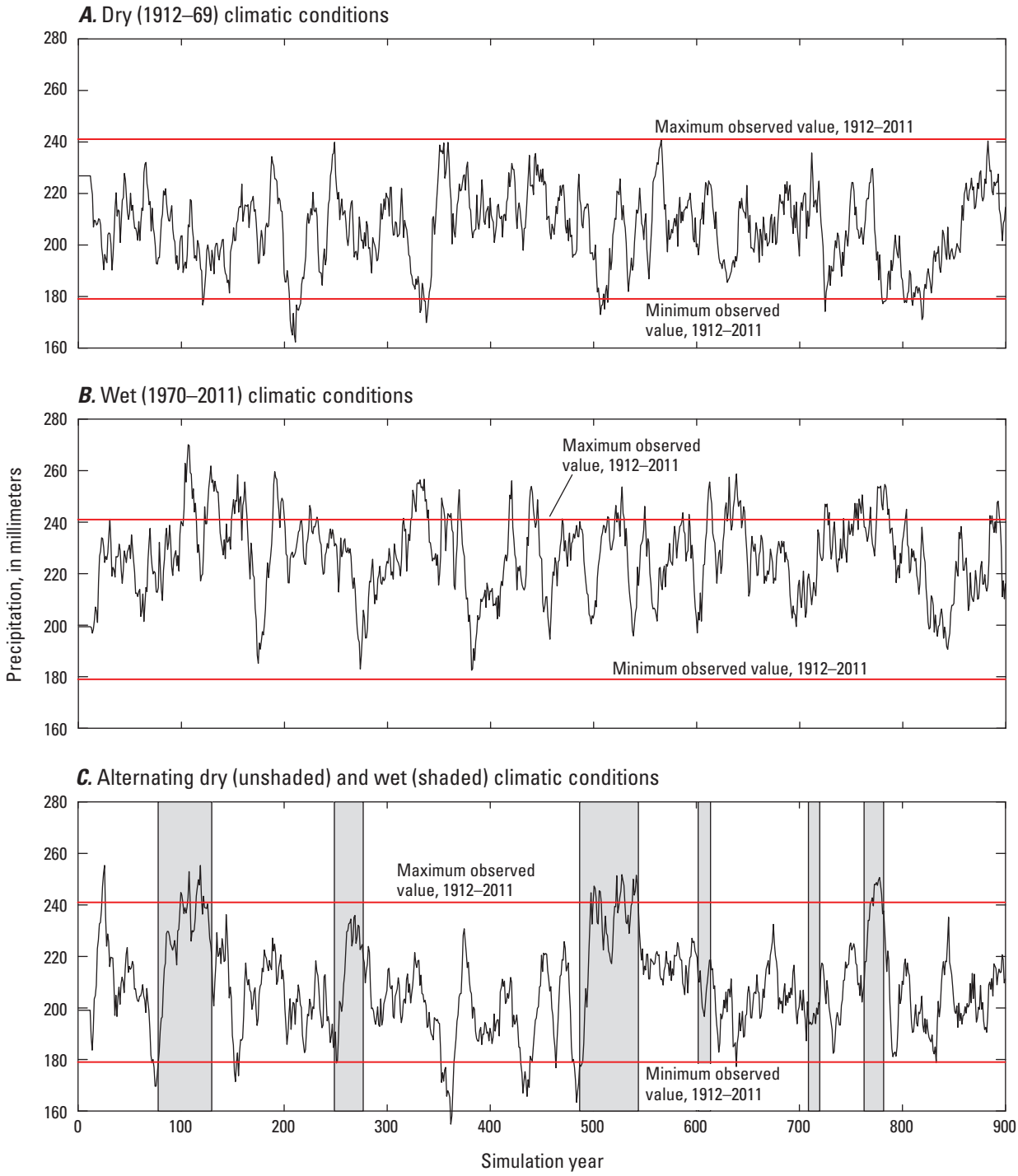

Figure 13. Long-term (900-year) simulated 12-year moving average precipitation for season 3 (July–October) and station group 4 (northeast). *A*, dry conditions. *B*, wet conditions. *C*, alternating dry/wet conditions.

Table 6. Selected United States and Canadian streamflow-gaging stations used for calibration of the water-balance model.

[Sask., Saskatchewan; N. Dak., North Dakota; Man., Manitoba]

Station identifier	Station name	State/ province	Period of record	Comment
05ND004	Moose Mountain Creek near Oxbow	Sask.	1913−present	Seasonal with some continuous record. No record 1918−32.
05NA003	Long Creek at western crossing of international boundary	Sask.	1959−present	Continuous.
05113600	Long Creek near Noonan	N. Dak.	1959−present	Continuous.
05NB001	Long Creek near Estevan	Sask.	1911−present	Seasonal and continuous. No record 1924−32 and 1958.
05NB036	Souris River below Rafferty Reservoir	Sask.	1992−present	Continuous.
05114000	Souris River near Sherwood	N. Dak.	1930−present	Continuous.
05116000	Souris River near Foxholm	N. Dak.	1936−present	Continuous.
05116500	Des Lacs River at Foxholm	N. Dak.	1904−present	No record 1907−45.
05117500	Souris River above Minot	N. Dak.	1903−present	Continuous.
05120000	Souris River near Verendrye	N. Dak.	1937−present	Continuous.
05120500	Wintering River near Karlsruhe	N. Dak.	1937−present	Continuous.
05122000	Souris River near Bantry	N. Dak.	1937−present	Continuous.
05123400	Willow Creek near Willow City	N. Dak.	1956−present	Continuous.
05123510	Deep River near Upham	N. Dak.	1957−present	Seasonal.
05124000	Souris River near Westhope	N. Dak.	1929−present	Continuous.
05NF001	Souris River at Melita	Man.	1912−present	Seasonal with some continuous record. No record 1923−34, 1937−74, 1977−2001.
05NG007	Plum Creek near Souris	Man.	1956−present	Seasonal with some continuous record. No record 1995−2001.
05NG021	Souris River at Souris	Man.	1946−present	Seasonal with some continuous record. No record 1948−66.
05NG001	Souris River at Wawanesa	Man.	1912−present	Seasonal with some continuous record.

An order of operations was followed when determining the method used for subbasin delineation. First, the Souris River Basin delineation, provided through the Agriculture and Agri-Food Canada's (AAFC) Watersheds Project 2013 (Government of Canada, 2015b), defined the border/edge of the basin for the Souris River. Second, USGS StreamStats, an online watershed delineation tool (U.S. Geological Survey, 2014c), was used for delineation of subbasins with an outlet located in the United States. To check the accuracy of the StreamStats delineation, and assist with determining the contributing area, the USGS Watershed Boundary Dataset (U.S. Geological Survey, 2015) was used. For instances when gaps between StreamStats and the USGS Watershed Boundary Dataset existed, delineation with ArcMap 10.2.2 Hydro Tools (Esri, 2014) and USGS 10-meter DEM (U.S. Geological Survey, 2014a) data was used. For outlets in Canada, the AAFC Total Gross Drain dataset (Government of Canada, 2015a) was used to define catchment areas given selected gaging stations.

Soil Characteristics

Soil permeability and available water storage data were obtained from the Gridded Soil Survey Geographic Database (gSSURGO) version 1.1 (U.S. Department of Agriculture, 2014), Detailed Soil Survey (DSS) of Canada (Agriculture and Agri-Food Canada, 2014), and Soil Landscapes Canada (SLC) Version 3.2 (Agriculture and Agri-Food Canada, 2013) at scales of 1:24,000; 1:100,000; and 1:1 million, respectively. Weighted averages were used to estimate soil permeability and available water storage capacity over 90- and 100-centimeter depths, respectively.

Weather Data

Monthly precipitation and temperature data were retrieved from the USHCN and AHCCD online databases as described in the previous section "Analysis of Long-Term Climate Variability." A total of 27 sites were used to estimate

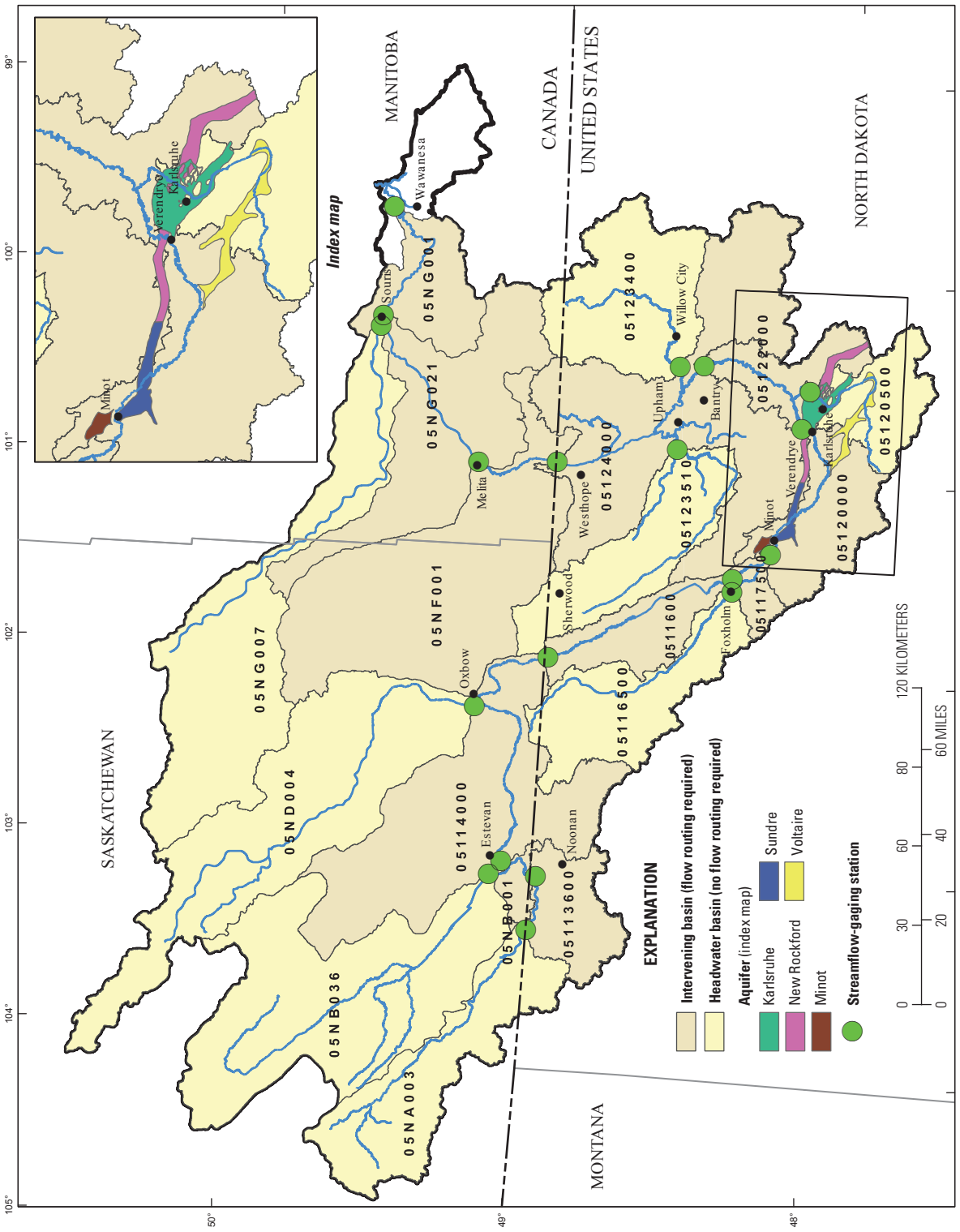

Figure 14. Streamflow-gaging stations and corresponding subbasins, designated by station identifier (table 1), used for developing the water-balance model.

monthly precipitation, temperature, and PET throughout the basin (table 7), with 26 of those sites located within a 1-degree buffer of the Souris River basin (fig. 8). Monthly PET values were estimated through use of the Hamon method, as previously described in the section "Stochastic Climate Model for Simulation of Precipitation, Temperature, and Potential Evapotranspiration."

In comparison with other PET estimation methods, the Hamon method has been shown to underestimate monthly PET, especially during spring and early summer (Rao and others, 2011). Rao and others (2011) suggested underprediction of PET by the Hamon method may be attributed to the method's lack of consideration of solar radiation. To compensate for low PET values in the WBM, a correction factor was applied such that PET values for every month were increased by the same percent. Through trial and error, a 10-percent increase in monthly PET was determined to be effective for the WBM. This correction factor seemed reasonable given other applications, such as Lu and others (2005), which used a correction factor to increase monthly PET by 20 percent. Similarly, a study by Rosenberry and others (2004) determined slight increases in PET, estimated using the Hamon method, resulted in better comparisons with the Bowen-ratio energy-budget method they used as standard in the study. In addition to the general underprediction of PET using the Hamon method, Rao and others (2011) noted the Hamon method had a tendency to stray from seasonal evapotranspiration (ET) patterns compared to other methods (such as Priestley-Taylor and Food and Agriculture Organization [FAO] full Penman-Monteith equation for a grass surface), with PET estimates that were significantly lower during spring and early summer. This low PET in the spring and early summer led to a steeper ascent to peak PET in July. To compensate for this underprediction and steep ascent, PET values from the Hamon method were increased in May and June, such that each subbasin adjustment could be different. By increasing the PET values, the steep ascent to peak PET in July was reduced along with reducing the general underprediction of PET. A list of watershed-specific PET adjustments is provided in table 8.

Water-Balance Model Description and Calibration

The WBM, adapted from Gray and McCabe (2010), is a mass-based deterministic model. Climatic inputs to the model consist of monthly precipitation, average temperature, and PET, along with static inputs such as soil permeability and available water storage capacity measured in depth equivalents. Climatic inputs are routed through the model using a series of equations intended to estimate the amount of water added, retained, and (or) lost at each monthly time step (see appendix). Application of the WBM at the scale of the subbasins (fig. 14) would have limited the ability of the model to take into account changes in soils and climatic variability within the subbasins. To better account for variations in soils and climatic conditions throughout the subbasins, and at the same time maintain reasonable computation times, a grid of 8x8-km cells was used to divide the Souris River Basin into 1,103 cells. The WBM was then applied to individual grid cells, allowing for site-specific estimation of runoff in response to spatial variations in precipitation and (or) soil characteristics across the basin. Soil permeability and available water storage capacity were averaged to each grid cell using weighted averages (fig. 15). Precipitation, temperature, and PET were interpolated from the weather station locations (fig. 8) to each grid cell using locally weighted polynomial regression (loess; Cleveland and others, 1992) in the statistical

Table 7. Selected United States and Canadian weather stations used for calibration of the water-balance model.

[Sask., Saskatchewan; Mont., Montana; N. Dak., North Dakota; Man., Manitoba]

Station identifier	Station name	State/ province	Latitude	Longitude
4011441	Ceylon	Sask.	49.4	-104.7
4016560	Regina	Sask.	50.4	-104.7
245572	Medicine Lake 3 southeast	Mont.	48.5	-104.5
4019040	Yellow Grass	Sask.	49.8	-104.2
4013660	Kelliher	Sask.	51.3	-103.8
4013480	Indian Head	Sask.	50.5	-103.7
321871	Crosby	N. Dak.	48.9	-103.3
4012400	Estevan	Sask.	49.2	-103.0
4010400	Bangor	Sask.	50.9	-102.3
4019082	Tonkin	Sask.	51.2	-102.2
4014913	Manor	Sask.	49.6	-102.1
4015360	Moosomin	Sask.	50.1	-101.7
5012080	Pierson	Man.	49.2	-101.3
5010240	Birtle	Man.	50.4	-101.1
325479	Mandan Experiment Station	N. Dak.	46.8	-100.9
320941	Bottineau	N. Dak.	48.8	-100.4
328792	Towner 2 northeast	N. Dak.	48.4	-100.4
329445	Willow City	N. Dak.	48.6	-100.3
5010480	Brandon	Man.	49.9	-99.9
5022000	Ninette	Man.	49.4	-99.7
5042004	Neepawa Murray	Man.	50.2	-99.6
5010640	Cypress River	Man.	49.5	-99.1
5041535	Langruth West	Man.	50.4	-98.8
324958	Langdon Experimental Farm	N. Dak.	48.8	-98.3
5012321	Portage Prairie	Man.	50.0	-98.3
5021849	Morden	Man.	49.2	-98.1
248569	Vida	Mont.	47.9	-105.4

Table 8. Parameters from calibration of the monthly water-balance model using reconstructed natural (unregulated) monthly streamflow from the U.S. Army Corps of Engineers.

[C_{AWS}, available water storage capacity parameter; C_{DRO}, direct runoff parameter; C_{SM}, snowmelt runoff parameter; PET, potential evapotranspiration; m^3/s, cubic meter per second; Sask., Saskatchewan; N. Dak., North Dakota; NA, correlation coefficient not available due to lack of reconstructed streamflow data; --, no runoff cap applied; calibration coefficients for each subbasin are described in the appendix]

Station/ subbasin identifier	Station name	State/ province	C_{AWS}	C_{DRO}	C_{SM}	Adjustment factors		Correlation coefficient[1]	Runoff cap (m^3/s)	Percentage of excess overland flow entering the stream in the current/following month
						PET (May)	PET (June)			
05ND004	Moose Mountain Creek near Oxbow	Sask.	1.2	0.15	0.01	1.35	1.25	0.85	56	50/50
05NA003	Long Creek at western crossing of international boundary	Sask.	1.0	0.6	0.05	1.2	1.1	0.77	--	50/50
05113600	Long Creek near Noonan	N. Dak.	1.0	0.2	0.03	1.2	1.1	0.78	--	50/50
05NB001	Long Creek near Estevan	Sask.	1.0	0.2	0.03	1.2	1.1	NA	--	50/50
05NB036	Souris River below Rafferty Reservoir	Sask.	1.1	0.35	0.01	1.2	1.1	0.78	--	50/50
05114000	Souris River near Sherwood	N. Dak.	1.2	0.1	0.01	1.3	1.2	0.85	--	50/50
05116000	Souris River near Foxholm	N. Dak.	1.0	0.3	0.03	1.3	1.2	0.85	--	50/50
05116500	Des Lacs River at Foxholm	N. Dak.	1.0	0.3	0.04	1.0	1.0	0.75	--	50/50
05117500	Souris River above Minot	N. Dak.	1.0	0.3	0.04	1.0	1.0	0.84	--	50/50
05120000	Souris River near Verendrye	N. Dak.	0.9	0.5	0.05	1.0	1.0	0.84	--	50/50
05120500	Wintering River near Karlsruhe	N. Dak.	1.0	0.5	0.04	1.1	1.0	0.75	21	50/50
05122000	Souris River near Bantry	N. Dak.	1.0	0.3	0.03	1.1	1.0	0.84	--	50/50
05123400	Willow Creek near Willow City	N. Dak.	1.0	0.25	0.01	1.2	1.1	0.81	--	50/50
05123510	Deep River near Upham	N. Dak.	1.1	0.4	0.01	1.1	1.0	0.83	--	80/20
05124000	Souris River near Westhope	N. Dak.	1.1	0.1	0.01	1.1	1.0	0.78	--	20/80

[1] Correlation coefficient is of log transformed data. Before data was logged each streamflow value was increased by 1 m^3/s to eliminate the possibility of taking the log of a zero flow.

software R (R Core Team, 2015). The loess function makes use of locally weighted regression to assign values to each grid cell based on latitude and longitude. For this application, similar to Ryberg and others (2014), the loess function with polynomial degree of 1 (linear in latitude and longitude) and a span of 0.7 was used.

A simplified schematic of the WBM, adapted from Gray and McCabe (2010), for a generic grid cell is shown in figure 16. A brief description of the model is given here and detailed equations are given in the appendix. Precipitation for a grid cell is partitioned into rain or snow depending on the average monthly temperature. Snow is stored in the snowpack until early spring when temperatures rise and snowmelt is produced. A small portion of the snowmelt directly enters the stream as runoff. The remainder of the snowmelt is used to help reduce (or eliminate) the soil moisture deficit remaining from the previous time step and, depending on time of year, contributes to subsurface flow. The rate of subsurface flow (the percentage of the soil moisture that is assumed to enter the stream) increases with increasing permeability and decreases with increasing soil moisture deficit. The rate of subsurface flow is also dependent on temperature such that temperatures below -10 degrees Celsius (°C) restrict all subsurface flow because soils are frozen. Temperatures above 2 °C leave subsurface flow unrestricted because soils are thawing or have thawed. After losses to subsurface flow have been considered and additions either through snowmelt and (or) liquid precipitation have been accumulated, a fraction of the water in excess of the soil moisture capacity (SMC) is considered to contribute to direct runoff (if any) and is therefore unavailable for PET. The remaining water in the system, after subtractions from direct runoff, is referred to as the total available water (TAW) (or the water available for PET or additional overland flow). If TAW exceeds SMC plus moisture demand (PET) for the month, ET is assumed to equal PET, and the excess (TAW–PET–SMC) is assumed to enter the stream as overland flow. The proportion of overland flow entering the stream in the current month, compared to the following month, was determined

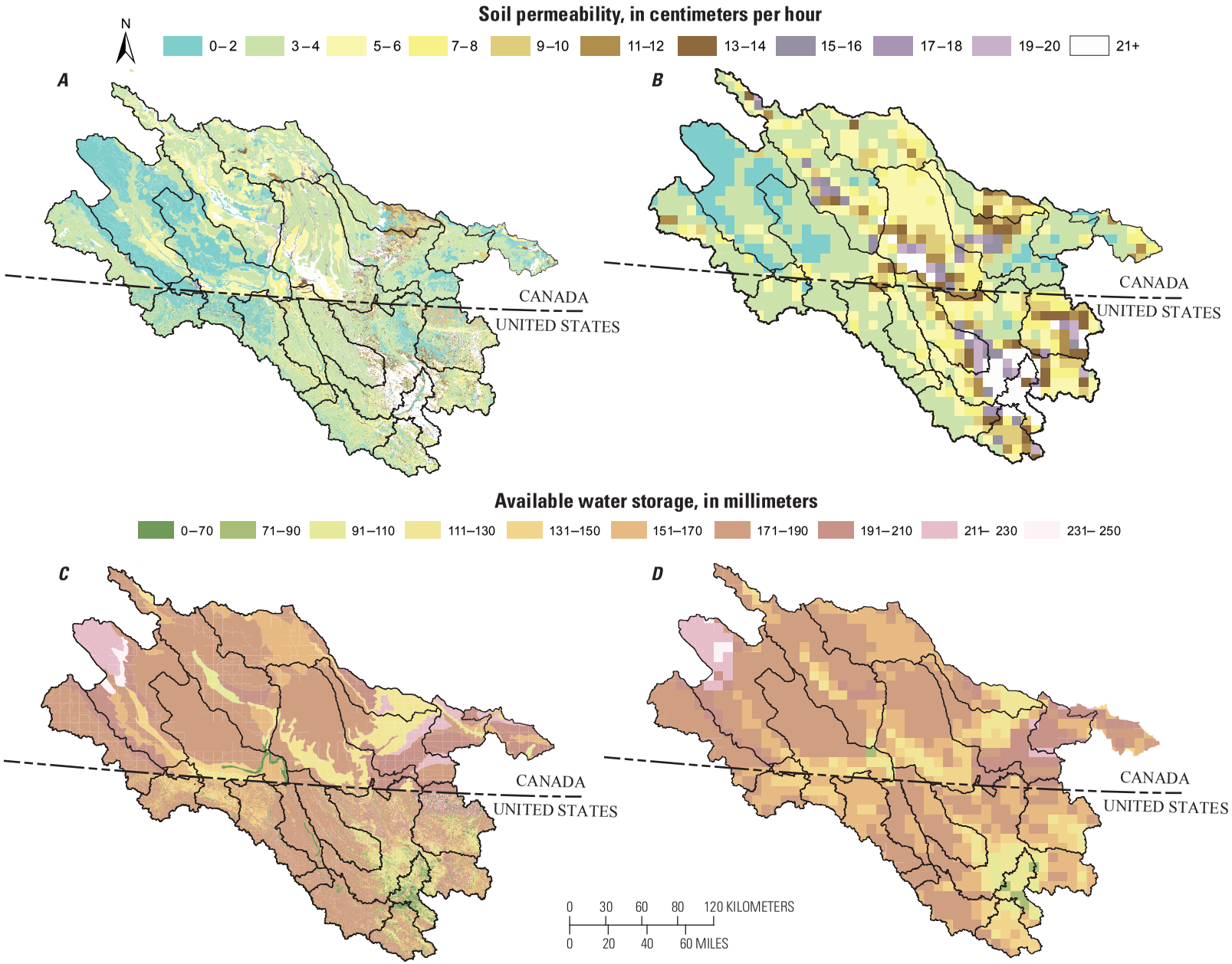

Figure 15. Soil permeability and available water storage (AWS) capacity. *A*, soil permeability before data are averaged to the 8-kilometer x 8-kilometer grid. *B*, soil permeability after data are averaged to the 8-kilometer x 8-kilometer grid. *C*, AWS before data are averaged to the 8-kilometer x 8-kilometer grid. *D*, AWS after data are averaged to the 8-kilometer x 8-kilometer grid.

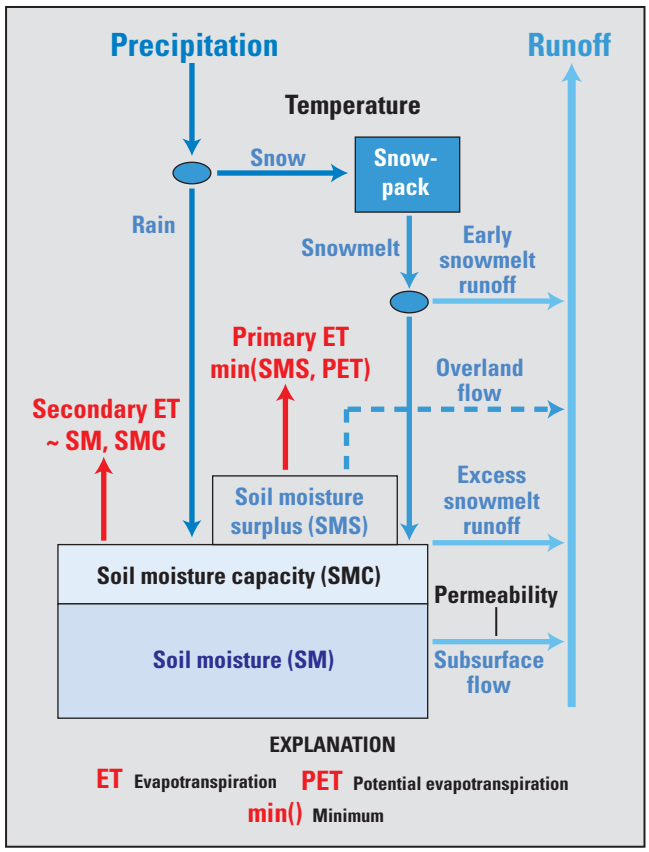

Figure 16. Schematic of water-balance model for a generic grid cell.

through trial and error (table 8) with the intent to closely match the monthly means and standard deviations of the natural streamflow reported by the USACE (U.S. Army Corps of Engineers, 2013). Basins in other settings would most likely have different proportions of flow entering the stream in the current as compared to the following month, because the proportion is highly dependent on size, topography, and climate of the basin. In addition, for 2 (Moose Mountain Creek near Oxbow, Sask., 05ND004 and Wintering River near Karlsruhe, N. Dak., 05120500) of the 15 subbasins, the amount of overland flow was capped such that the overland flow for a given month could not exceed the maximum streamflow recorded (1946 – 2011) at the outlet of that basin (table 8). Runoff caps were applied to those subbasins whose monthly mean streamflow values, after calibration, still tended to overpredict the monthly mean streamflow values provided by the USACE (U.S. Army Corps of Engineers, 2013).

If TAW exceeds soil moisture capacity but is not sufficient to satisfy PET, the surplus (TAW–SMC) is lost as primary ET, and there is no overland flow. A part of the unsatisfied moisture demand (PET–primary ET) is subtracted from the soil moisture as secondary ET, where the amount of secondary ET decreases in proportion to the ratio of soil-moisture storage to the soil-moisture storage capacity. If TAW is less than SMC, there is no primary ET, and thus total ET consists of secondary ET removed from the soil moisture.

The model has five adjustable parameters. These five parameters were estimated to maximize the correlation between estimated and natural monthly streamflows while matching, as closely as possible, monthly means and standard deviations of the natural monthly streamflows (table 8). Two of the five parameters (F_{GW} and F_{ST} in the appendix) were dependent on spatially variable soil properties and temperature and were not calibrated to individual subbasins. The three basin-specific parameters consist of two parameters to control the amount of early snowmelt runoff and the rate of surplus runoff and one parameter to adjust the available water storage capacity. The snowmelt runoff parameter (C_{SM}) ranged between 0.01 and 0.05, the surplus runoff parameter (C_{DRO}) between 0.1 and 0.6, and the available water storage capacity parameter (C_{AWS}) between 0.9 and 1.2 (table 8). The parameters act as coefficients within the model, either increasing or decreasing model values by a certain percent. Neighboring or upstream subbasins tended to have similar parameters as seen with the Souris River near Foxholm, N. Dak. (05116000); Des Lacs River at Foxholm, N. Dak. (05116500); and Souris River above Minot, N. Dak (05117500) subbasins (fig. 14), where each basin had a C_{AWS} and C_{DRO} value of 1.0 and 0.3, respectively, and varied slightly with C_{SM} values ranging between 0.03 and 0.04 (table 8). Subbasins that tended to have higher C_{AWS} values also tended to have lower C_{DRO} and C_{SM} values. Similarly, subbasins with lower C_{AWS} tended to have higher C_{DRO} and C_{SM} values. This can be seen with the Moose Mountain Creek near Oxbow, Sask. (05ND004) subbasin, which had C_{AWS}, C_{DRO}, and C_{SM} values of 1.2, 0.15, and 0.01, respectively; and the Souris River near Verendrye, N. Dak. (05120000) subbasin, which had C_{AWS}, C_{DRO}, and C_{SM} values of 0.9, 0.5, and 0.05, respectively (table 8).

The WBM estimates monthly runoff for an individual grid cell; taking the average of all grid cells overlying a specific subbasin provides an average runoff estimate for that specific subbasin. Runoff was estimated for each of the 15 subbasins; subbasins that did not require streamflow routing (8 headwater basins) were calibrated first through trial and error (fig. 14). Two objectives were used in the calibration: maximizing the correlation between estimated and natural monthly flows and reproducing, as closely as possible, the monthly means and standard deviations of the natural flows. The WBM is not intended as a forecast model to predict natural flows as closely as possible. A forecast model would require much more detailed data inputs with respect to the spatial and temporal distribution of precipitation in the basin and was considered beyond the scope of this report. Rather, the WBM is intended for simulating flows that reproduce the statistical distributions of natural monthly flows given monthly climatic inputs. In most cases, a higher correlation between estimated and natural flows could have been obtained at the expense of deviating from the monthly means and standard deviations; furthermore, there may be many different model configurations and (or) parameter estimates that result in similar correlation coefficients. The monthly means and standard deviations were more sensitive to the model equations (appendix)

and parameter values (table 8) than were the correlation coefficients between estimated and natural flows.

An example of the calibrated WBM output for one of the headwater basins, Long Creek at western crossing of the international boundary (05NA003) (fig. 14), is shown in figures 17 and 18. The WBM was able to closely replicate historical streamflow events where simulated results were able to catch most of the high flow and almost all of the low flow events with a correlation coefficient of 0.8 (fig. 17). In addition, the monthly means showed little to no bias between natural and simulated values (fig. 18*A*). Similarly, monthly standard deviations for simulated and natural flows followed the same trend with monthly variation peaking in April and June along with a slight dip in May (fig. 18*B*).

Natural (Unregulated) Streamflow Routing

After runoff values were estimated for each of the headwater basins, flows were routed through downstream basins and intervening flows calibrated with USACE natural flow data (U.S. Army Corps of Engineers, 2013). During the calibration process, intervening basin parameters were checked for similarity to neighboring basins to ensure calibration was reasonable (table 8). All but one subbasin, Long Creek near Estevan, Sask. (05NB001), was calibrated with natural flow data (fig. 14). For the Long Creek near Estevan, Sask. (05NB001) subbasin, there was no natural flow data available for calibration, and as a result basin parameters were assumed to be the same as the upstream subbasin, Long Creek near Noonan, N. Dak. (05113600). Given the relatively small size of the Long Creek near Estevan, Sask. (05NB001) subbasin (295 km^2) and similar topography and vegetation to the Long Creek near Noonan, N. Dak. (05113600) subbasin, this seemed to be a reasonable assumption.

To route monthly flows through the Souris River Basin, direct routing and lagging were used. Direct routing involved the simple addition of streamflow from separate subbasins (upstream and downstream) such that flows in the same time step were added. Lagging involved delaying the amount of flow for the current time step by partitioning the flow such that a fraction of the flow comes from the current time step and the remaining fraction comes from the previous time step; for example, taking 90 percent of the flow from the current time step and 10 percent from the previous time step creates a lagged/delayed flow of about 3 days when considering a monthly time step of 30 days. The combination of direct and lagged routing allows for a simplified routing model that takes into consideration time of travel for routed flows. When the reach between a basin's outlet and the downstream outlet was short (less than about 45 km), no lag was applied and flows were directly routed. Subbasins that did not have a lag for downstream flow routing included Long Creek at western crossing of the international boundary (05NA003); Long Creek near Noonan, N. Dak. (05113600); Moose Mountain Creek near Oxbow, Sask. (05ND004); Souris River near Foxholm, N. Dak. (05116000); Des Lacs River at Foxholm. N. Dak. (05116500); and Souris River near Westhope, N. Dak. (05124000) (table 9). In cases where the river reach extended beyond 45 km and (or) there were hydraulic structures limiting flow, lags were applied. The extent of the lag applied was determined through trial and error such that the monthly means and standard deviations of simulated routed monthly flows closely matched those provided by the USACE (U.S. Army Corps of Engineers, 2013). A list of the subbasins and their respective lags are given in table 9. Lags were applied to their respective subbasin when flows were being routed from that subbasin to the next (table 9). For example, for estimating streamflow at the Souris River near Foxholm, N. Dak. (05116000) gaging station, flows (with their respective lags) would be routed up to Foxholm, but the lag provided for Foxholm would not be applied; however, for estimating streamflow at the next downstream gaging station, Souris River above Minot, N. Dak. (05117500), the lag would be applied to Foxholm as accumulated flows are routed from Foxholm to Minot. Simulated monthly means for the Souris River near Sherwood, N. Dak. (05114000) and Souris River near Westhope, N. Dak. (05124000) gaging stations compared well with mean natural monthly streamflow from the USACE (fig. 19), showing very little bias between simulated and natural monthly streamflow. Similarly, the standard deviations for simulated and natural monthly streamflow compared well (fig. 20) with simulated monthly standard deviations following the same trends as those produced by the USACE data.

Disaggregation of monthly streamflow to a three-per-month or approximately 10-day time step allows for a more precise routing of flows and provides simulated natural flow data that can assist with reservoir operation. Reservoir operation is highly dependent on 30-day forecasted streamflow volumes, with forecasts being updated daily during flood years. Flood years are those in which the 30-day streamflow volume at the Souris River near Sherwood, N. Dak. (05114000) gaging station (fig. 1) is greater than 216,105,696 cubic meters (m^3) (175,200 acre-foot [acre-ft]) or local flows to this gage exceed a 30-day volume of 37,004,400 m^3 (30,000 acre-ft) (U.S. Army Corps of Engineers, 2013). Disaggregation of monthly streamflow to a three-per-month time step allows reservoir operators to not only look at forecasted streamflow volumes for each month but also allows them to look at forecasted streamflow volumes for the 1st (days 1–10), 2nd (days 11–20), and 3rd (days 21 through the end of the month) periods of each month, which enables them to make more time sensitive operation decisions.

Disaggregation of monthly flows was done by taking historic daily flow values at each of the gaging points and calculating the fraction of monthly flow occurring in the 1st, 2nd, and 3rd periods of the month. The disaggregation resulted in there being three periods for each month, each of which had a ratio defining the fraction of monthly flow occurring during that period, such that when the ratios were added for all three periods the sum was equal to one. The ratios were then used to subdivide simulated monthly streamflow to three-per-month values during the same historic record. In other

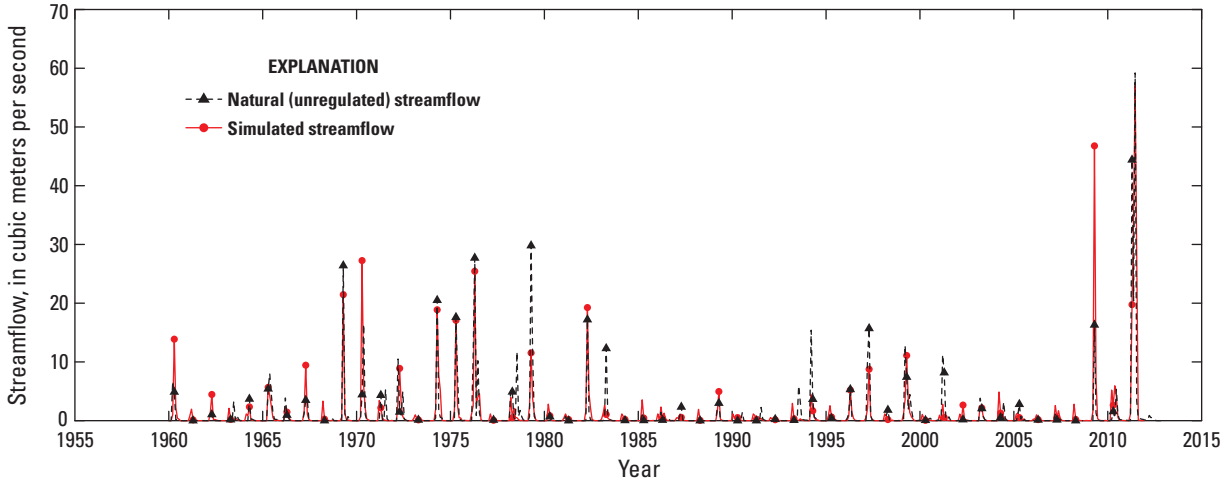

Figure 17. Simulated and natural (unregulated) monthly streamflow for Long Creek at the western crossing of the international boundary (05NA003).

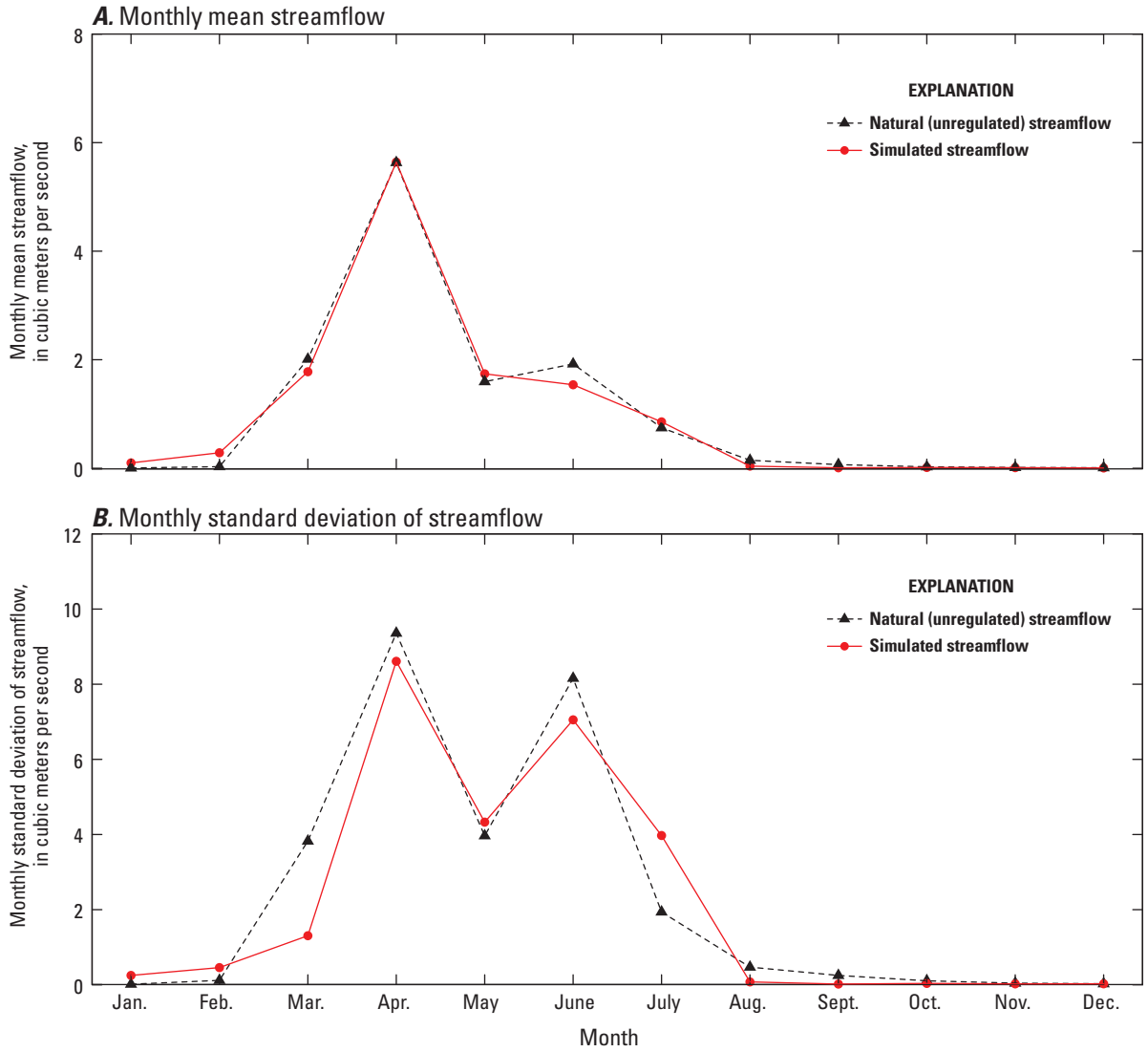

Figure 18. Simulated and natural (unregulated) monthly streamflow for Long Creek at the western crossing of the international boundary (05NA003). *A*, monthly mean streamflow. *B*, monthly standard deviation of streamflow.

Table 9. Lags applied to monthly streamflow routing model.

[Sask., Saskatchewan; N. Dak., North Dakota]

Station/subbasin identifier	Station name	State/ province	Fraction of current monthly streamflow	Fraction of previous monthly streamflow
05ND004	Moose Mountain Creek near Oxbow	Sask.	1.0	0
05NA003	Long Creek at western crossing of international boundary	Sask.	1.0	0
05113600	Long Creek near Noonan	N. Dak.	1.0	0
05NB001	Long Creek near Estevan	Sask.	0.8	0.2
05NB036	Souris River below Rafferty Reservoir	Sask.	0.8	0.2
05114000	Souris River near Sherwood	N. Dak.	0.95	0.05
05116000	Souris River near Foxholm	N. Dak.	1.0	0
05116500	Des Lacs River at Foxholm	N. Dak.	1.0	0
05117500	Souris River above Minot	N. Dak.	0.9	0.1
05120000	Souris River near Verendrye	N. Dak.	0.8	0.2
05120500	Wintering River near Karlsruhe	N. Dak.	0.8	0.2
05122000	Souris River near Bantry	N. Dak.	0.75	0.25
05123400	Willow Creek near Willow City	N. Dak.	0.75	0.25
05123510	Deep River near Upham	N. Dak.	0.75	0.25
05124000	Souris River near Westhope	N. Dak.	1.0	0

words, historic ratios during a specific year and month were applied to the same year and month for the simulated values. Once all the monthly subbasin flows had been subdivided into three-per-month flows, they were routed through the Souris River Basin in a similar manner as the monthly flows, with additional consideration taken for streamflow loss to evaporation and aquifer recharge (table 10). The three-per-month flows were calibrated such that simulated 10-day means and standard deviations compared well with the natural flow data provided by the USACE (U.S. Army Corps of Engineers, 2013).

At the three-per-month time step, it was easier to catch small losses in streamflow assumed to be contributed to evaporation and (or) aquifer recharge. Subbasins with lagged flows greater than 1 day had noticeable streamflow losses, which increased as the lag increased (table 10). This may be the result of increased exposure of streamflow to surface evaporation as well as the result of streamflow loss to nearby/underlying aquifers. Specifically, Pusc (1994) noted that the Souris River can lose anywhere from 0.13 to 0.52 m^3/s to the Minot aquifer (fig. 14), with a potential for losing greater amounts (Pettyjohn, 1967; Bradley, 1963). The Minot aquifer is within the Souris River near Verendrye, N. Dak. (05120000) subbasin (fig. 14), but losses to the Minot aquifer were too small for the three-per-month routing model to catch; however, Pusc (1994) focused mainly on water losses to the Minot aquifer and there are several aquifers that lie downstream, which may contribute to streamflow loss. These aquifers include, but are not limited to, Sundre, Voltaire, Karlsruhe, and New Rockford (fig. 14).

In addition to considering the effects of evaporation and aquifer recharge in the three-per-month streamflow routing model, the effects of the J. Clark Salyer NWR also resulted in modifications to the routing model. Inclusion of the J. Clark Salyer NWR resulted in a reduction of peak flows during the spring and increased flows during the summer at the Souris River near Westhope, N. Dak., (05124000) gaging station because of water being retained in the spring for management of vegetation and then slowly released throughout the summer months (U.S. Army Corps of Engineers, 2013). Although the amount of water retained for management of vegetation in the spring and the amount released throughout the summer varied each year depending on management needs and water availability, an average amount retained and released was determined through trial and error such that simulated 10-day means and standard deviations compared well with the natural 10-day historical flows provided by the USACE (U.S. Army Corps of Engineers, 2013). To account for the effects of the J. Clark Salyer NWR in the three-per-month streamflow routing model, peak flows were reduced in the spring by retaining 15 percent of the natural streamflow during March, April, and May. Then, during the summer months (June, July, August, September), some of the retained flow was released such that 8 percent of the average 10-day flow between March and May was released for each 10-day period between June and September, resulting in slightly higher flows at Westhope during the summer months. A list of basin-specific lags and streamflow loss coefficients is provided in table 10.

Routed 10-day simulated flows compared well with natural flows provided by the USACE, with 10-day means and standard deviations showing little bias and following similar trends in 10-day variation (figs. 21 and 22); hence, both routed 10-day and monthly natural flows matched the statistical properties of historical natural flow quite well.

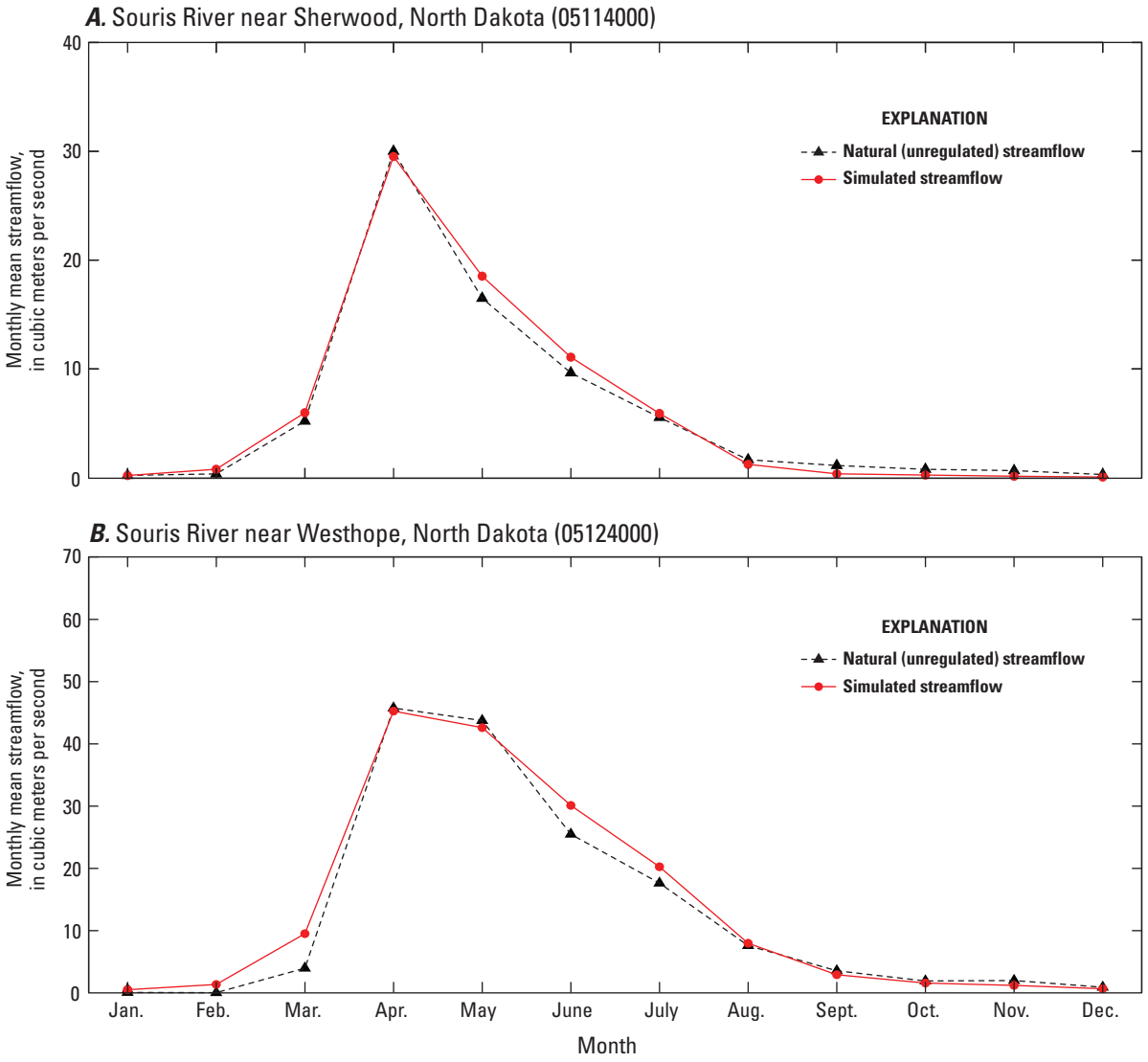

Figure 19. Means of simulated and natural (unregulated) monthly streamflow. *A*, the Souris River near Sherwood, North Dakota (05114000) streamflow-gaging station. *B*, the Souris River near Westhope, North Dakota (05124000) streamflow-gaging station.

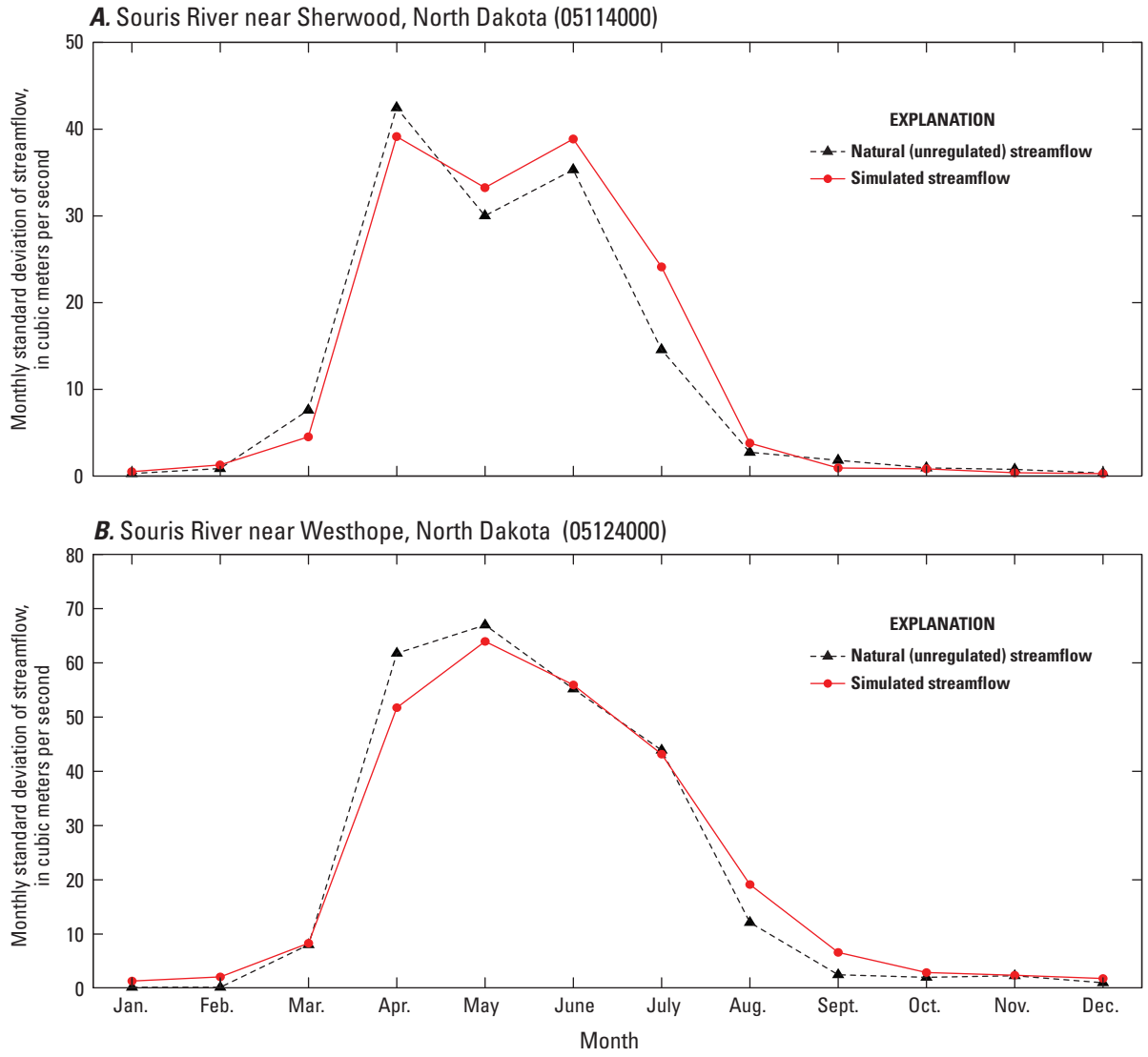

Figure 20. Standard deviations of simulated and natural (unregulated) monthly streamflow. *A*, the Souris River near Sherwood, North Dakota (05114000) streamflow-gaging station. *B*, Souris River near Westhope, North Dakota (05124000) streamflow-gaging station.

Table 10. Lags applied to 10-day streamflow routing model.

[Sask., Saskatchewan; N. Dak., North Dakota; NA, not available due to lack of reconstructed streamflow data]

Station/subbasin identifier	Station name	State/ province	Fraction of current 10-day streamflow	Fraction of previous 10-day streamflow	Streamflow loss (percent)
05ND004	Moose Mountain Creek near Oxbow	Sask.	1.0	0	0
05NA003	Long Creek at western crossing of international boundary	Sask.	1.0	0	0
05113600	Long Creek near Noonan	N. Dak.	0.80	0.20	5
05NB001	Long Creek near Estevan	Sask.	NA	NA	NA
05NB036	Souris River below Rafferty Reservoir	Sask.	0.80	0.20	5
05114000	Souris River near Sherwood	N. Dak.	0.90	0.10	0
05116000	Souris River near Foxholm	N. Dak.	1.0	0	0
05116500	Des Lacs River at Foxholm	N. Dak.	1.0	0	0
05117500	Souris River above Minot	N. Dak.	0.90	0.10	0
05120000	Souris River near Verendrye	N. Dak.	0.65	0.35	7
05120500	Wintering River near Karlsruhe	N. Dak.	0.65	0.35	7
05122000	Souris River near Bantry	N. Dak.	0.60	0.40	([1])
05123400	Willow Creek near Willow City	N. Dak.	0.60	0.40	([1])
05123510	Deep River near Upham	N. Dak.	0.70	0.30	([1])
05124000	Souris River near Westhope	N. Dak.	1.0	0	0

[1]Streamflow loss is dependent on the amount of flow retained in the J. Clark Salyer National Wildlife Refuge versus the amount of flow released during the summer months.

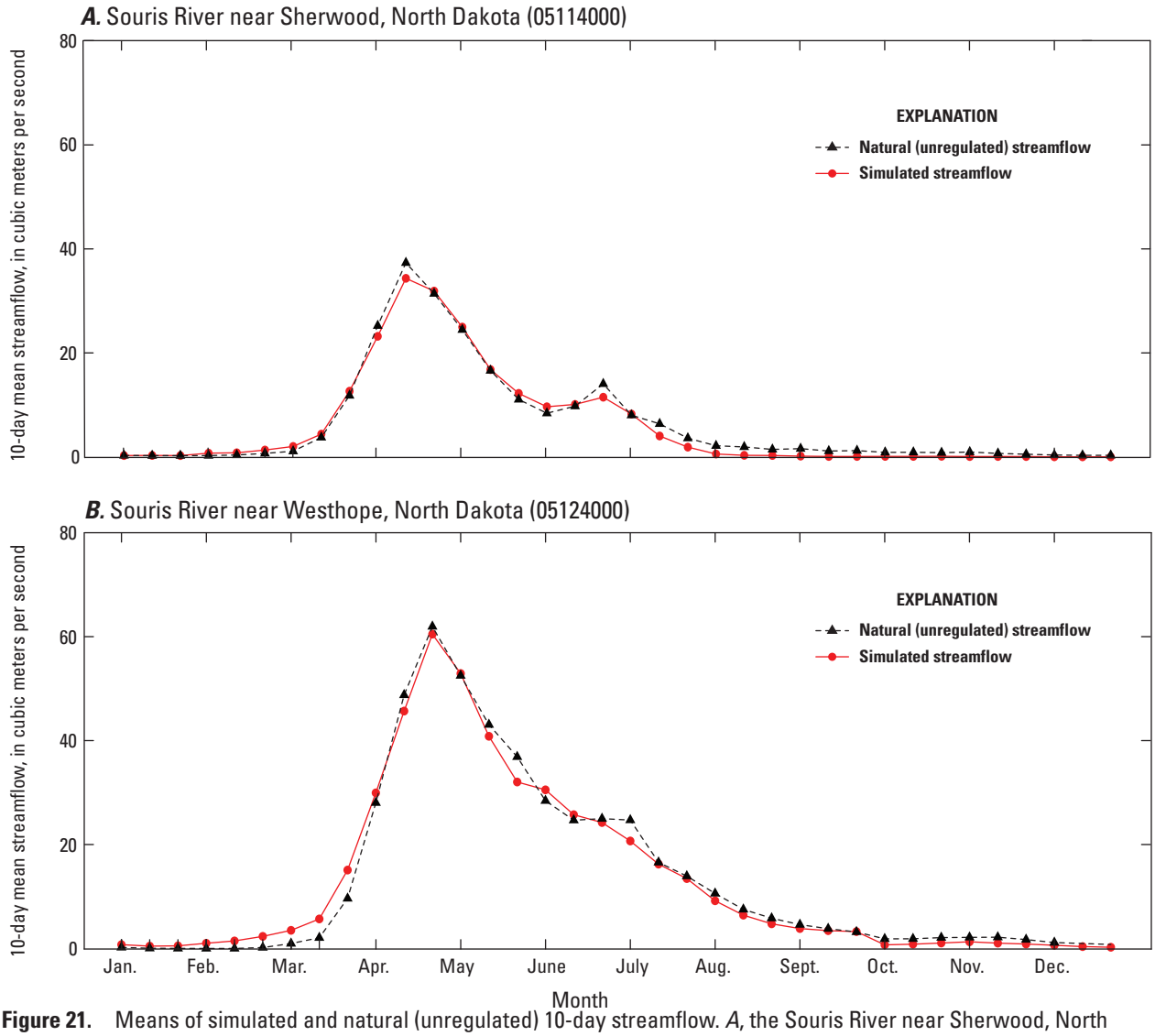

Figure 21. Means of simulated and natural (unregulated) 10-day streamflow. *A*, the Souris River near Sherwood, North Dakota (05114000) streamflow-gaging station. *B*, Souris River near Westhope, North Dakota (05124000) streamflow-gaging station.

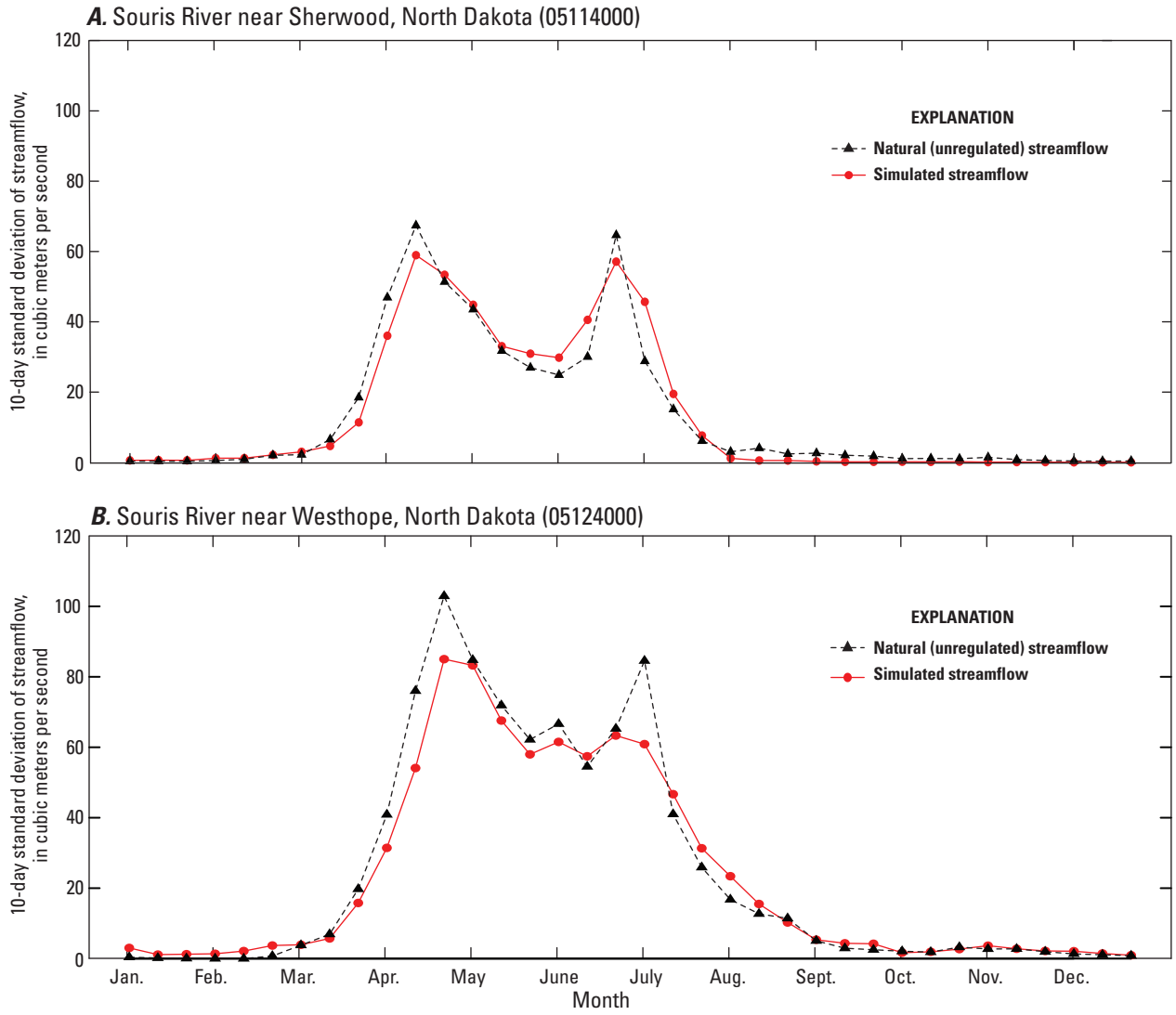

Figure 22. Standard deviations of simulated and natural (unregulated) 10-day streamflow. *A*, the Souris River near Sherwood, North Dakota (05114000) streamflow-gaging station. *B*, the Souris River near Westhope, North Dakota (05124000) streamflow-gaging station.

Stochastic Natural Streamflow Model

When evaluating future flood risk for the Souris River Basin, revising reservoir operating rules, or designing levees or other hydraulic structures, it is critical to have a model that can simulate future flows that realistically mimic natural flows and accurately represent the probabilities of future extreme events. The stochastic natural streamflow model is intended to simulate future conditions well beyond the envelope of those seen in the historical record and assign probabilities that can be used to evaluate risk and complete economic cost/benefit analyses. In this section, the stochastic climate simulation and water-balance models, described in previous sections, are combined to simulate future natural flows, which in turn are used to compute flow-frequency curves (frequency distributions). Such distributions are used extensively for designing hydraulic structures and completing cost/benefit analyses; however, in the standard application of these methods it is assumed that both climate and streamflow are stationary (that is, the frequency distribution remains constant through time). Long historical streamflow records are used to compute an empirical frequency distribution, which in turn is modeled using a theoretical statistical distribution such as the log-Pearson type III distribution (Interagency Advisory Committee on Water Data, 1982); however, for cases such as the Souris River Basin where (1) climate is not stationary and (2) extreme hydroclimatic variability and persistence make determining the theoretical frequency distribution difficult even with a long historical record, it is necessary to use a different approach such as the one described in this section.

Methods

To combine the stochastic climate simulation model (SCSM) and the WBM, the group-averaged seasonal data from the SCSM (eq. 1) needed to be converted into monthly data for specific locations that could be used by the WBM. To ensure that the simulated monthly data realistically represented the statistical properties (means, variances, serial correlations, and cross-correlations) of actual data, a simple conditional resampling approach was used:

$$\begin{aligned} PET_{L,m}(y) &= R^{PET}_{L,m}(y) PET_{G,S}(y); P_{L,m}(y) \\ &= R^{P}_{L,m}(y) P_{G,S}(y); L = 1,\cdots,4; m = 1,\cdots,4 \end{aligned} \quad (10)$$

where

$PET_{L,m}(y)$ is the potential evapotranspiration for the meteorological station L, month m, and year y;

$R^{PET}_{L,m}(y)$ is the ratio computed from historical data for potential evapotranspiration PET, meteorological station L, month m, and year y;

$P_{L,m}(y)$ is the precipitation for the meteorological station L, month m, and year y; and

$R^{P}_{L,m}(y)$ is the ratio computed from historical data for precipitation P, meteorological station L, month m, and year y.

where L designates the particular meteorological station locations in group G and m designates the particular months in season S. For each year, there were 192 ratios (16 for each of the 12 combinations of station group and season) for PET and 192 ratios for precipitation. For each year of the historical record from y=1946 to y=2011, the ratios were computed. The starting year 1946 was used because ratios needed to be matched with the ratios used for disaggregating simulated flows from a monthly to 10-day time step, and the latter ratios were not available before 1946. For a given simulation year, the group-averaged seasonal values for PET and precipitation generated using the SCSM were multiplied by the ratios for a randomly sampled (with replacement) historical year to obtain simulated values of PET and precipitation for each month and station location:

$$\begin{aligned} PET_{L,m}(\mathrm{Y}) &= R^{PET}_{L,m}(y^*) PET_{G,S}(\mathrm{Y}); P_{L,m}(\mathrm{Y}) \\ &= R^{P}_{L,m}(y^*) P_{G,S}(\mathrm{Y}); L = 1,\cdots,4; m = 1,\cdots,4 \end{aligned} \quad (11)$$

where Y designates a simulation year and y^* a randomly sampled historical year. In accordance with the dry (1912–69) and wet (1970–2011) climate states described previously for the SCSM, for the dry climate state, y^* is randomly sampled from historical years 1946–69, and for the wet climate state, y^* is randomly sampled from historical years 1970–2011.

Simulated monthly temperature was back-calculated from simulated monthly PET using separate equations for each combination of month and station location. Simulated values for monthly PET, precipitation, and temperature for each meteorological station location and month were then interpolated to the 8x8-km grid cells using the same loess procedure described previously for the WBM calibration and used to obtain simulated monthly streamflow values for each subbasin. The monthly streamflow values for each subbasin were disaggregated to three values per month using the same randomly sampled historical year y^* that was used to disaggregate the climatic inputs, and the 10-day streamflow routing model was used to simulate streamflow for each gaging station. The reason for using the same randomly sampled year is that the relative distribution of monthly flow among the 10-day subintervals for a particular year should be determined by climatic conditions (timing of snowmelt, for example) for that year. Although the climate simulations consisted of "climate years" November–October (November and December from the previous calendar year combined with January–October of the current calendar year), the WBM simulations were done using calendar years (January–December). Because November and December are winter months with minimal runoff, the difference between using calendar year y^*or y^*–1 ratios for those months to disaggregate monthly flows was expected to be negligible; furthermore, because in either case (climate years or calendar years) the break between years happens in late fall or

winter, discontinuity from the end of one year to the beginning of the next year caused by randomly sampling 2 separate years to disaggregate climate variables or streamflow was minimal.

Stochastic Simulation Results

As discussed in the "Stochastic Climate Model for Simulation of Precipitation, Temperature, and Potential Evapotranspiration" section of this report, the Souris River Basin can be characterized by wet or dry equilibrium climate states. Soil-moisture storage can potentially cause a long lag-time between the onset of a new climate state and the eventual onset of the new streamflow equilibrium. To evaluate flood risk in this light, 100 independent realizations, or traces, of streamflow data were generated, each starting in a wet equilibrium state that continues for 50 years before transitioning to a dry state that continues for an additional 50 years. It is not necessary at the outset to specify exactly when this transition may take place in the future or even to specify a starting year for the simulations. To avoid dependence of the WBM simulations on initial conditions (such as starting soil-moisture storage), an initial 10-year "burn-in" period was discarded at the beginning of each trace.

Example simulated traces are illustrated for three of the gaging stations (table 6)—Souris River below Rafferty Reservoir (05NB036), Souris River above Minot, N. Dak. (05117500), and Wintering River near Karlsruhe, N. Dak. (05120500) (figs. 1 and 14; hereafter referred to as the "Rafferty," "Minot," and "Wintering" gaging stations, respectively). For comparison with the actual data, historical natural streamflows for 1946–2011 are shown in figure 23. The red lines in these graphs show the median, 90th percentile, and maximum recorded values for the annual maximum 10-day natural streamflow during 1946–2011. These graphs highlight the extreme interannual streamflow variability of the Souris River Basin; for example, for the Minot gaging station, the annual maxima are near zero for many years and for a "normal" year (represented by the median), the maximum is about 30 m^3/s. To put this value in perspective, 30 m^3/s of flow for a 10-day period for this site corresponds to only about 1 mm of runoff for the upstream drainage area. At the upper extreme, in 2011 the maximum 10-day flow was about 500 m^3/s, which corresponds to about 16 mm of runoff. During most years, runoff for the Souris River Basin is only a small fraction of the precipitation that falls in the basin and is much less than the soil-moisture storage capacity; thus, streamflow is extremely variable and persistent (characterized by a tendency for clusters of low-flow and high-flow years). The same properties are evident in the historical flows for the other two gaging stations as well.

One of the 100 simulated streamflow traces for the three selected gaging stations is shown in figure 24. This trace is similar overall to the natural streamflow record (fig. 23) (but with the wet period at the beginning rather than the end). For the Rafferty gaging station, during the wet simulation period there was one simulation year that exceeded the 2011 recorded maximum, and 10 percent (5 out of 50) of the annual maxima exceeded the 90th percentile of the recorded maxima. For the other two gaging stations and the wet simulation period, none of the simulated annual maxima exceeded the value from 2011 but several simulated maxima exceeded the 90th percentile line. There was a stark contrast for this trace between the simulated flows for the wet and dry periods. For the dry period, only one of the simulated maxima for both the Rafferty and Minot gaging stations and three for the Wintering gaging station exceeded the 90th percentile line.

Another simulated trace is shown in figure 25. This trace differs from the previous example in that there are more extreme simulated high flows during the wet period. For the Rafferty and Minot gaging stations, there are two simulation years during the wet period for which the annual maxima exceeded the value from 2011. In addition, for the Rafferty and Minot gages the simulated maximum for the second year of the dry period exceeded the 2011 value, which indicates that high soil moisture conditions at the end of the wet period can persist for several years after the transition to drier conditions; however, as shown by the high simulated value for Rafferty near the end of the dry period, occasional extremes similar to 2011 can take place even after the lower streamflow equilibrium is reached.

The set of 100 independent streamflow traces were used to estimate equilibrium frequency distributions for the wet and dry climate states. The first 50 years of each trace (5,000 simulation years for the 100 traces) are assumed to represent the equilibrium distribution for the wet climate state, and the last 40 years of each trace (4,000 simulation years) are assumed to represent the equilibrium distribution for the dry climate state. Years 51–60 are assumed to represent a transition period from the wet to the dry state before equilibrium was reached for the dry state. The probability of exceeding a given value for a specified streamflow variable (such as the annual maximum 10-day flow or the annual total flow volume) was estimated using the percent of the simulation years for which the value was exceeded.

The equilibrium frequency distributions for annual maximum 10-day mean streamflow and annual total streamflow volume for the Rafferty gaging station are shown in figure 26. To allow comparison with the historical data, empirical frequency distributions for the historical natural flow data for 1946–69 (representing the dry climate state) and 1970–2011 (representing the wet climate state) are plotted along with the curves computed using the simulated data. The Rafferty gaging station location is important because it represents natural inflows to Rafferty Reservoir, which is the major flood control structure for downstream communities. The capacity of Rafferty Dam at its maximum storage capacity is 633 million cubic meters (International Joint Commission, 1989), which is shown by the horizontal line in figure 26*B*. In 2011, total inflow to Rafferty Reservoir was almost 1.2 billion cubic meters, twice its capacity. Much of the inflow came during a span of a few weeks in May and June of that year, overwhelming the reservoir and causing a large uncontrolled spill. The equilibrium frequency curve for annual total volume for the wet climate state (the

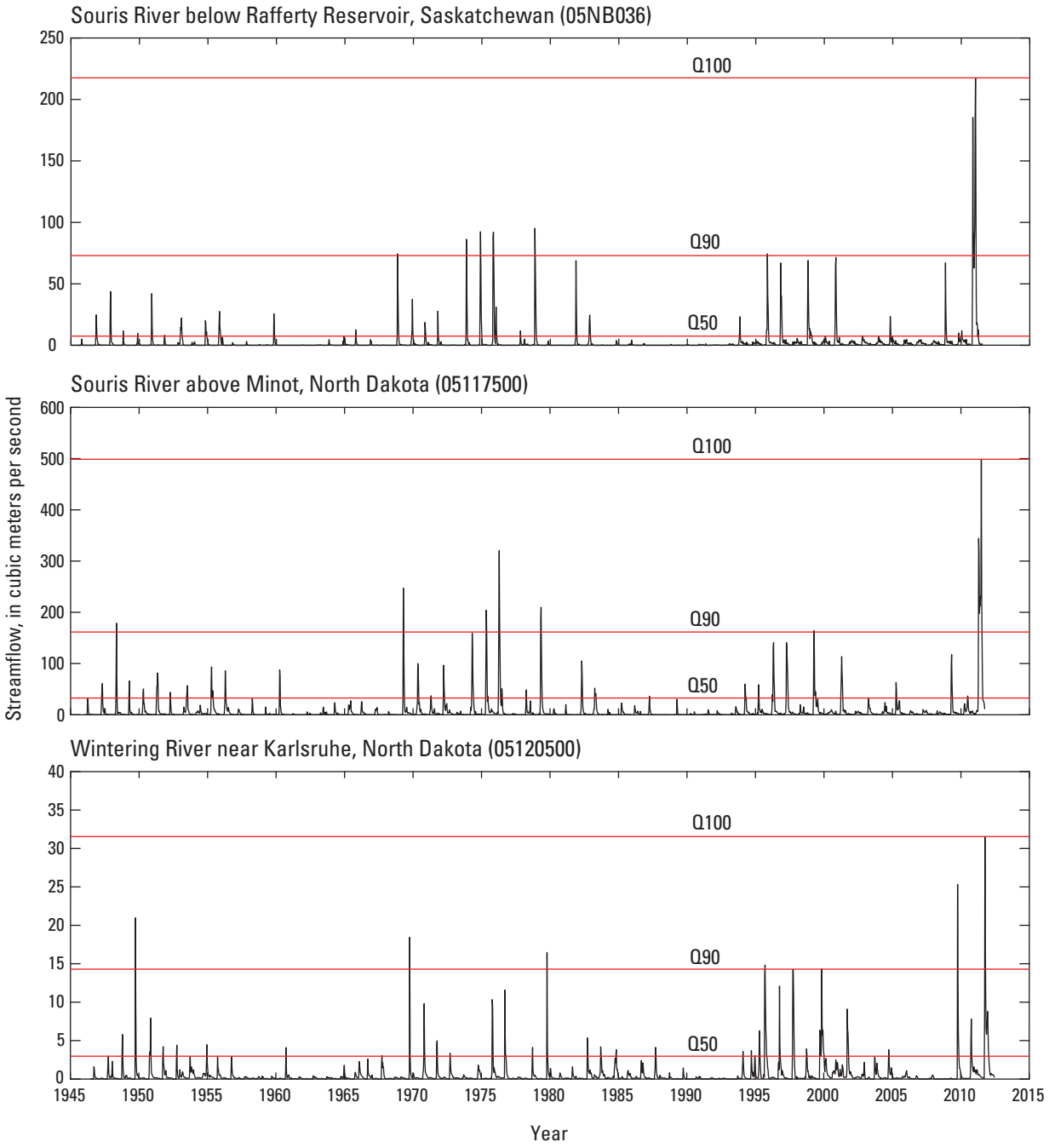

Figure 23. Natural (unregulated) 10-day mean streamflow for 1946–2011 for the Souris River below Rafferty Reservoir, Saskatchewan (05NB036), Souris River above Minot, North Dakota (05117500), and Wintering River near Karlsruhe, North Dakota (05120500), streamflow-gaging stations as compared to the median (Q50), 90th percentile (Q90), and maximum (Q100) recorded values of annual maximum 10-day streamflow.

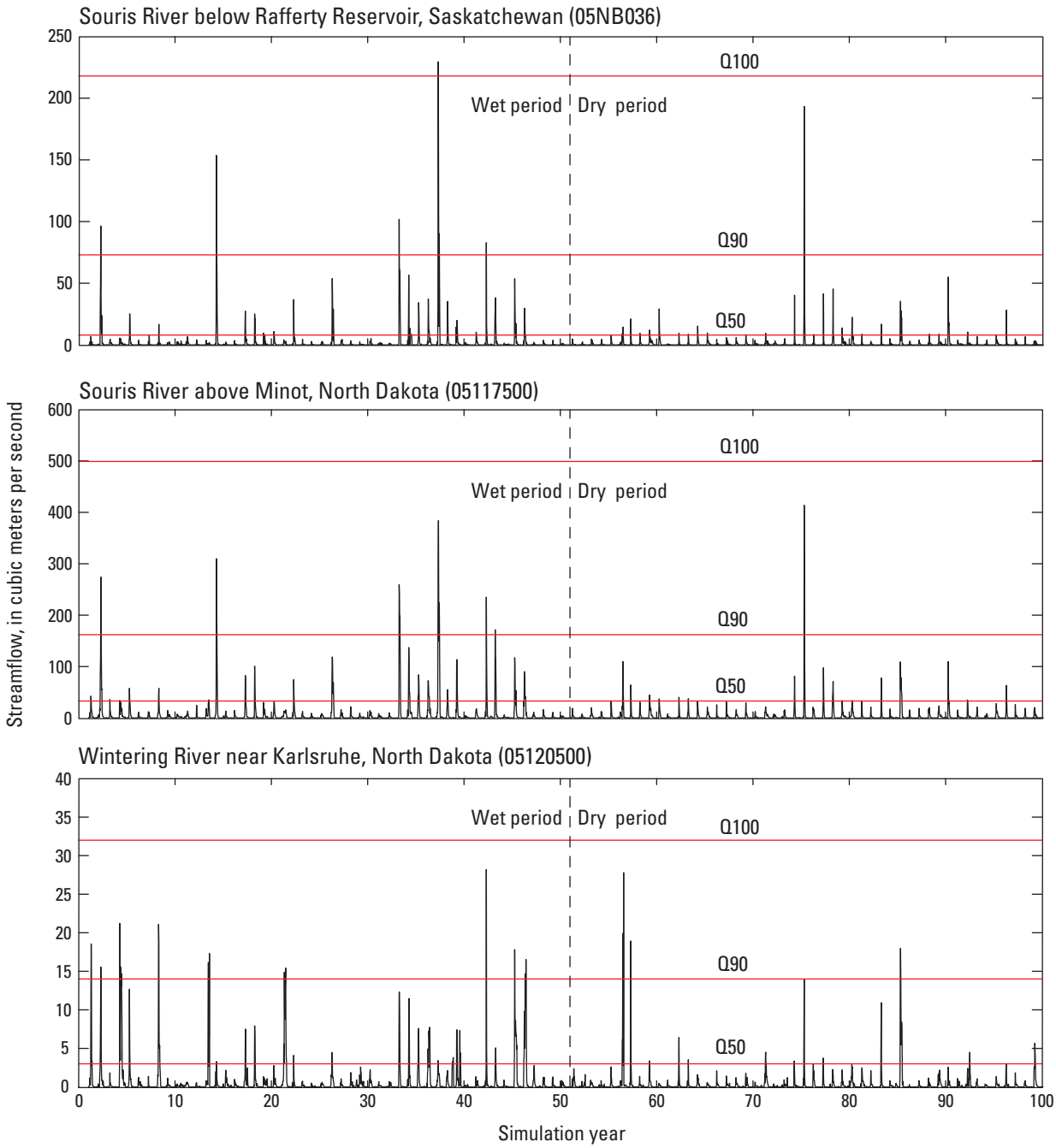

Figure 24. Simulated 10-day mean streamflow for 100-year simulation period (50 years of wet climate state followed by 50 years of dry climate state) for the Souris River below Rafferty Reservoir, Saskatchewan (05NB036), Souris River above Minot, North Dakota (05117500), and Wintering River near Karlsruhe, North Dakota (05120500), streamflow-gaging stations (trace 10 out of 100) as compared to the median (Q50), 90th percentile (Q90), and maximum (Q100) recorded values of annual maximum 10-day streamflow.

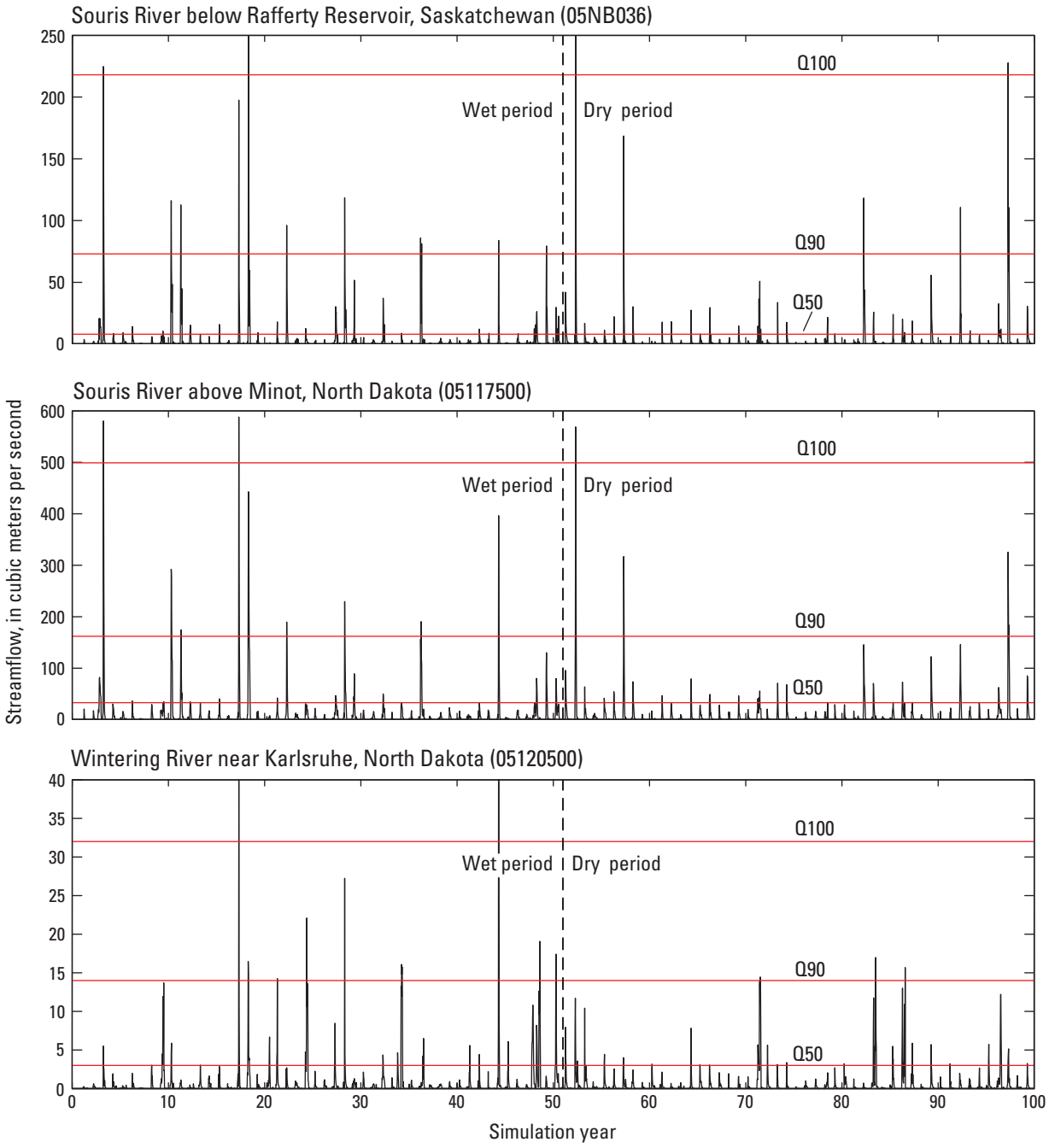

Figure 25. Simulated 10-day mean streamflow for 100-year simulation period (50 years of wet climate state followed by 50 years of dry climate state) for the Souris River below Rafferty Reservoir, Saskatchewan (05NB036), Souris River above Minot, North Dakota (05117500), and Wintering River near Karlsruhe, North Dakota (05120500), streamflow-gaging stations (trace 4 out of 100) as compared to the median (Q50), 90th percentile (Q90), and maximum (Q100) recorded values of annual maximum 10-day streamflow.

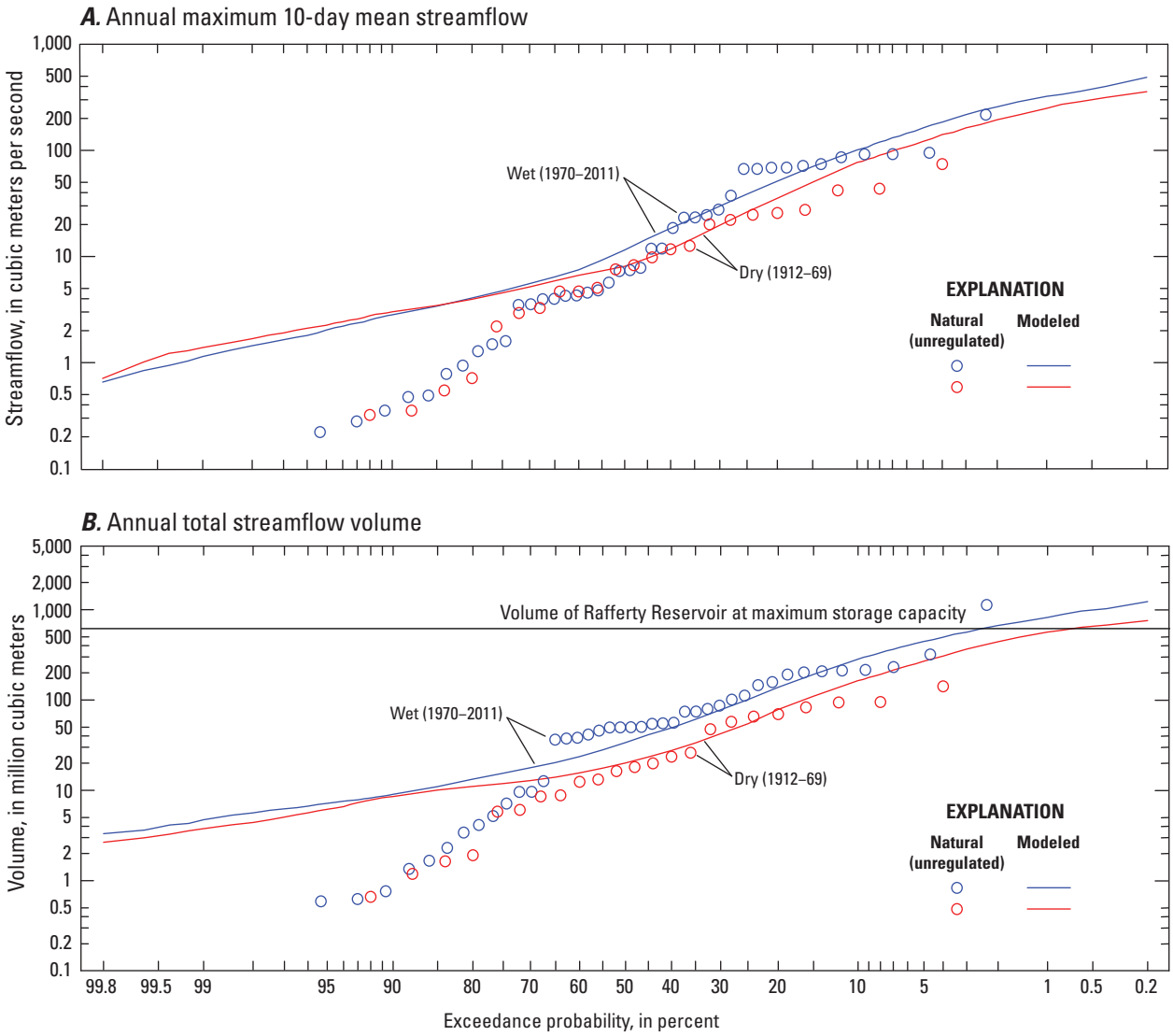

Figure 26. Equilibrium frequency distributions for the Souris River below Rafferty Reservoir, Saskatchewan (05NB036), streamflow-gaging station for wet (1970–2011) and dry (1912–1969) climate states. *A*, annual maximum 10-day streamflow; and *B*, annual total streamflow volume.

blue curve in figure 26*B*) indicates only about a 0.2 percent per year (1 in 500) chance of exceeding the 2011 inflow volume; however, it indicates a much more likely chance—about 3 percent per year—of exceeding the 633 million cubic meter capacity. In contrast, the dry equilibrium curve indicates only about a 0.5-percent chance of exceeding the 633 million cubic meter capacity; thus, it is about six times more likely to exceed 633 million cubic meters of inflow for the wet state compared to the dry state. Considering that the wet state could continue for several more decades, this high flood risk could have major implications for downstream flood control.

The equilibrium frequency distributions for the Minot gaging station are shown in figure 27. The maximum 10-day natural flow for this site in 2011 was about 500 m^3/s, which falls just below the equilibrium frequency curve for the wet state, indicating about a 3-percent per year chance of exceedance. In comparison, the dry equilibrium curve indicates less than a 0.5-percent per year chance of exceeding the same value. The annual total natural flow volume for the Minot gaging station was about 2.4 billion cubic meters in 2011, which, similar to the Rafferty gaging station, is estimated to have about a 0.5-percent per year chance of exceedance for the wet state. For the dry state, there is an extremely small chance (less than 0.1 percent) of exceeding the 2011 flow volume.

The equilibrium frequency distributions for the Westhope gaging station are shown in figure 28. This gage is at the international border between North Dakota and Manitoba. The results for this gage are similar to the previous examples; thus, it seems that the wet and dry climate states have a similar effect on streamflow for the entire main stem Souris River upstream from Westhope, which reinforces the conclusion that the shifting climate states represent a large regional phenomenon encompassing the Souris River Basin and other areas of Saskatchewan, North Dakota, and Manitoba.

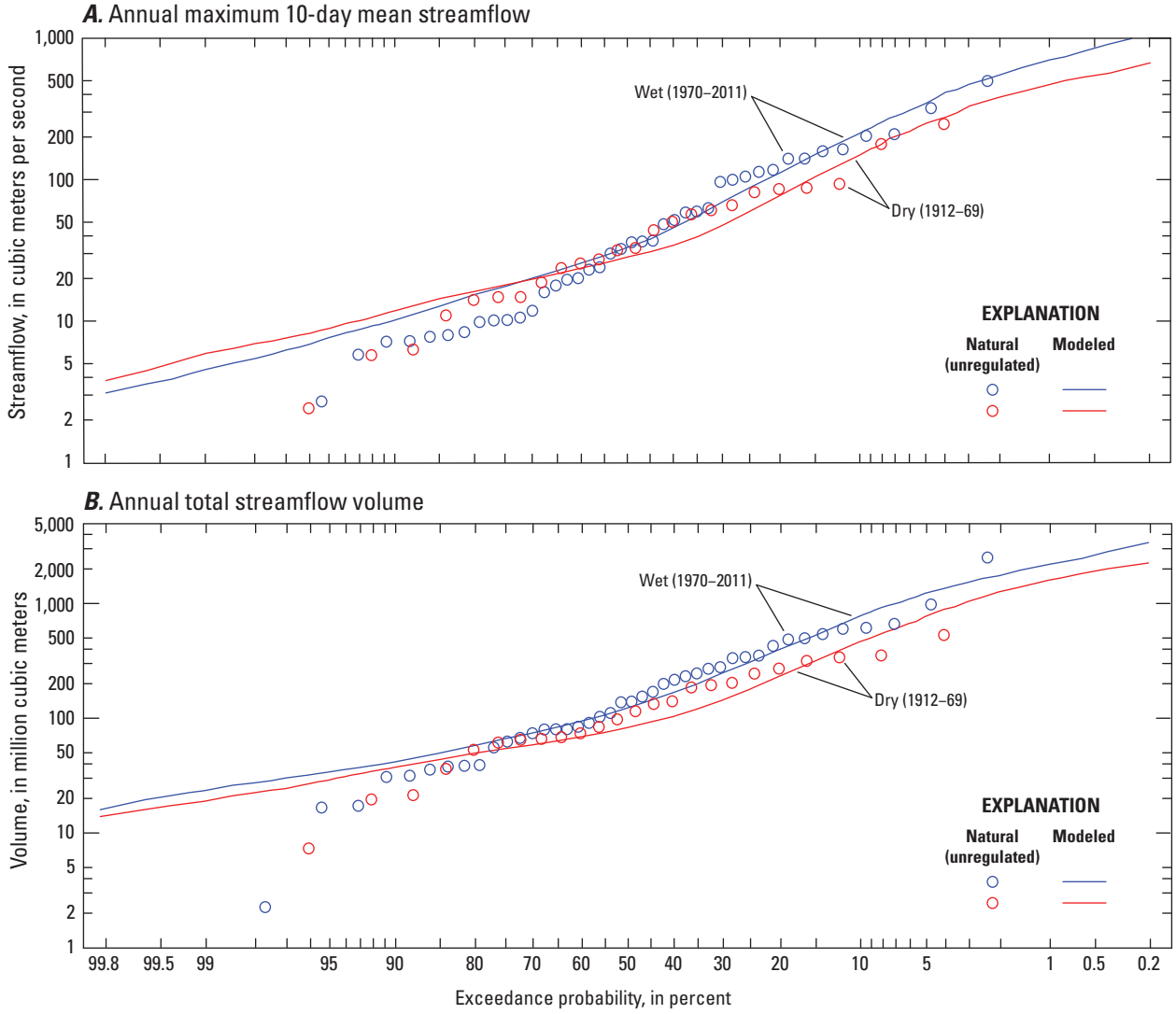

Figure 27. Equilibrium frequency distributions for the Souris River above Minot, North Dakota (05117500), streamflow-gaging station for wet (1970–2011) and dry (1912–69) climate states. *A*, annual maximum 10-day mean streamflow; and *B*, annual total streamflow volume.

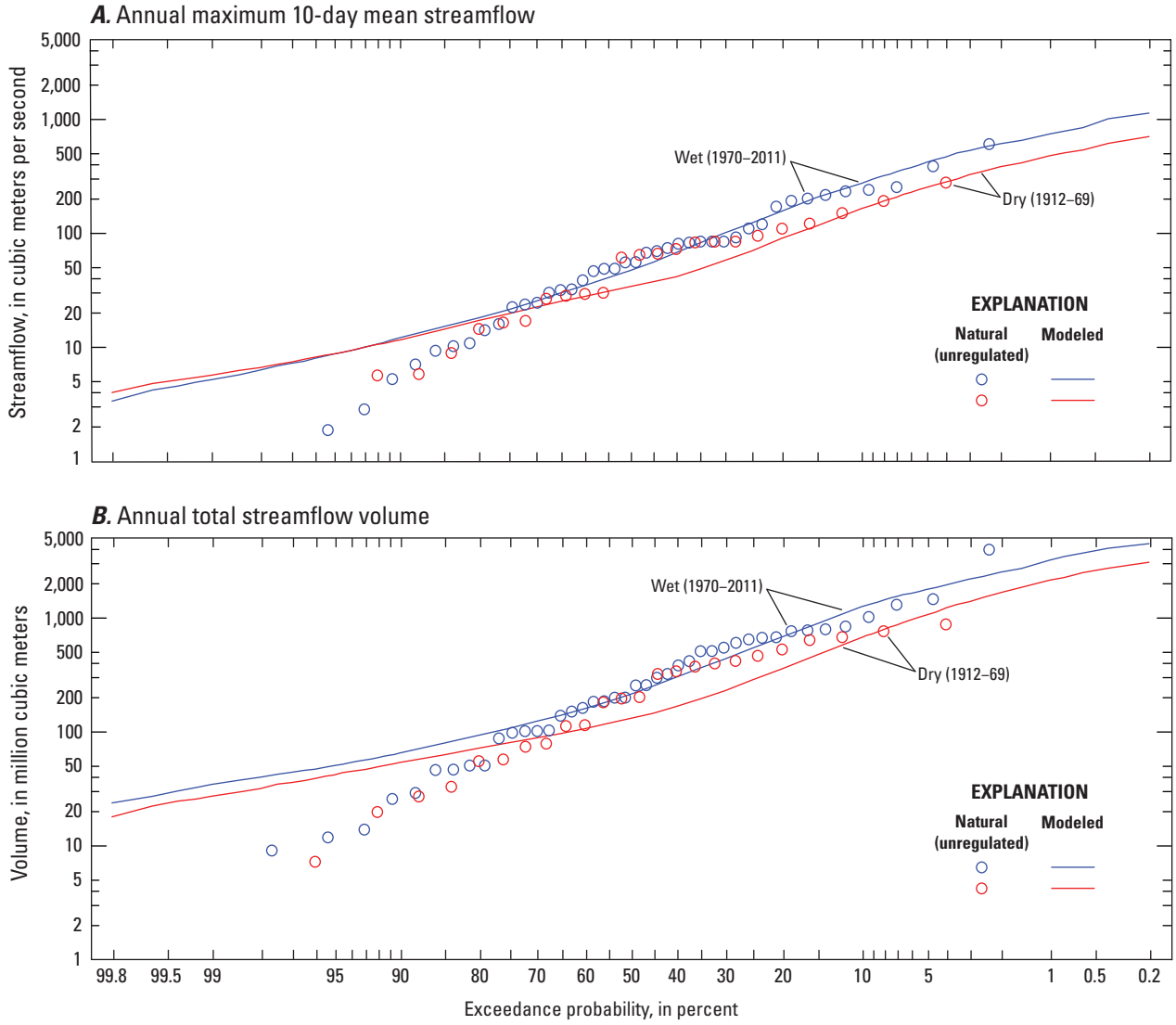

Figure 28. Equilibrium frequency distributions for the Souris River near Westhope, North Dakota (05124000), streamflow-gaging station for wet (1970–2011) and dry (1912–69) climate states. *A*, annual maximum 10-day mean streamflow; and *B*, annual total streamflow volume.

Summary

The Souris River Basin is a 61,000 square-kilometer basin in the Provinces of Saskatchewan and Manitoba and the State of North Dakota. In May and June of 2011, record-setting rains were seen in the headwater areas of the basin. Emergency spillways of major reservoirs were discharging at or near full capacity resulting in extensive flooding to numerous downstream communities. As a result, a Souris River Basin Task Force was appointed to develop a plan of study for mitigating future damages from extreme events such as the 2011 flood. One of the recommendations of the task force was to develop a model for simulating future streamflow that could determine the probabilities of future floods or droughts. In response to this recommendation, the U.S. Geological Survey, in cooperation with the North Dakota State Water Commission, developed a stochastic model for simulating Souris River Basin precipitation, evapotranspiration, and natural (unregulated) streamflow. Simulations from the model can be used in future studies to simulate regulated streamflow, design levees, and other structures, and complete economic cost/benefit analyses.

Long-term climatic variability was analyzed using tree-ring chronologies and meteorological data from United States and Canadian weather stations in a large region of south-central Canada and the north-central United States centered on the Souris River Basin. Five statistically distinct clusters of weather stations were identified based on seasonal precipitation patterns, resulting in five distinct climate regions, four of which overlapped the Souris River Basin. Using multiresolution decomposition of tree-ring chronologies along with multiple regression equations to predict seasonal precipitation based on tree-ring wavelets with wavelengths of 16, 32, and 64 years, it

was determined that most of the multidecadal variability of seasonal precipitation for the climate regions could be explained by the tree-ring chronologies. The tree-ring chronologies were used to hindcast precipitation to the early 1700s and compare recent (since the late 1800s) wet and dry conditions to earlier extreme conditions. It was shown that several extreme wet periods (as extreme as or more extreme than the wettest recorded period) and several extreme dry periods (as extreme as or more extreme than the driest recorded period) took place prior to the historical record. The extreme wet and dry periods were verified based on historical information and comparison with other paleoclimatic studies.

A stochastic climate model for simulation of precipitation, temperature, and potential evapotranspiration for the Souris River Basin was developed using the recorded meteorological data and the tree-ring-extended precipitation records. The model was developed first for seasonal data (three 4-month seasons: November–February, March–June, and July–October), and then the seasonal data were disaggregated to a monthly time step. A significant climate transition was seen around 1970, with 1912–69 representing a dry climate state and 1970–2011 representing a wet climate state. Although there were some distinct subpatterns within the basin, the predominant differences between the two states were higher spring through early fall precipitation and higher spring potential evapotranspiration for the wet compared to the dry state. Verification of the stochastic climate simulation model showed that it was able to reproduce both the short-term (annual to multidecadal) variability of the historical data and the long-term (multidecadal to century scale) variability of the tree-ring-extended data.

A water-balance model was developed for simulating monthly natural (unregulated) streamflow based on precipitation, temperature, and potential evapotranspiration. The model was calibrated using streamflow data from the U.S. Geological Survey and Environment Canada, as well as natural (unregulated) streamflow data from the U.S. Army Corps of Engineers. Streamflow was simulated for 15 streamflow-gaging stations. The water-balance model was designed to estimate monthly runoff from each of 1,103 8x8-kilometer grid cells covering the Souris River Basin based on moisture inputs (precipitation), moisture outputs (evapotranspiration and runoff), and soil-moisture storage. Static inputs include soil-moisture storage capacity and soil permeability; and dynamic inputs include monthly precipitation, temperature, and potential evapotranspiration interpolated to each grid cell from weather station data using a locally weighted smoothing algorithm. Monthly runoff for the grid cells was aggregated to obtain runoff for each of 15 subbasins, and a simple streamflow routing model was used to simulate monthly runoff for streamflow-gaging stations with more than one upstream subbasin. After calibrating the model for a monthly time step, monthly runoff for each subbasin was disaggregated into three values per month, or an approximately 10-day time step, and a separate streamflow routing model was developed for simulating 10-day streamflow for downstream streamflow-gaging stations. Water-balance model results indicated good agreement between simulated and natural (unregulated) streamflow for both the monthly and 10-day time steps. Correlation coefficients between simulated and natural (unregulated) flows were generally high and the seasonal means and standard deviations of the simulated flows closely matched the means and standard deviations of the natural (unregulated) flows.

The stochastic climate simulation model for precipitation, temperature, and potential evapotranspiration was combined with the water-balance model to simulate potential future sequences of 10-day mean streamflow for each of the streamflow-gaging station locations. Flood risk, as determined by equilibrium flow-frequency distributions for both the dry (1912–69) and wet (1970–2011) climate states, is considerably higher for the wet state compared to the dry state; for example, for the wet climate state, annual inflow volume for Rafferty Reservoir (the major flood control structure for downstream communities) has about a 3-percent chance per year of exceeding 633 million cubic meters, the maximum storage capacity of the reservoir. In contrast, for the dry climate state, the annual inflow volume has only about a 0.5-percent chance per year of exceeding 633 million cubic meters. Future flood risk will remain high until the wet climate state ends, and for several years after that, because there may be a long lag-time between the return of drier conditions and the onset of a lower soil-moisture storage equilibrium.

References Cited

Agriculture and Agri-Food Canada, 2013, Soil Landscapes of Canada, version 3.2: Government of Canada, accessed October 21, 2014, at http://sis.agr.gc.ca/cansis/nsdb/slc/v3.2/index.html.

Agriculture and Agri-Food Canada, 2014, Detailed Soil Survey (DSS) compilations: Government of Canada, accessed October 21, 2014, at http://sis.agr.gc.ca/cansis/nsdb/dss/v3/index.html.

Ault, T.R., and St. George, Scott., 2010, The magnitude of decadal and multidecadal variability in North American precipitation: Journal of Climate, v. 23, p. 842–850.

Bluemle, J.P., 1996, From the state geologist: North Dakota Geological Survey Newsletter, v. 23, no. 1, p. 1–2.

Bradley, Edward., 1963, Relation of surface and ground water in the Souris River Valley near Minot, North Dakota: U.S. Geological Survey Open-File Report 62–10, 12 p.

Bunn, A.G., Korpela, Mikko; Biondi, Franco; Campelo, Filipe; Mérian, Pierre; Mudelsee, Manfred; Qeadan, Fares; Schulz, Michael; and Zang, Christian, 2014, dplR—Dendrochronology program library in R: R Foundation for Statistical Computing, R package version 1.6.0.

Cleveland, W.S., Grosse, Eric., and Shyu, W.M., 1992, Local regression model, chap. 8 *of* Chambers, J.M., and Hastie, T.J., eds., Statistical models in S: Pacific Grove, California, Wadsworth & Brooks/Cole, p., 309–376.

Environment Canada, 2014, Adjusted and Homogenized Canadian Climate Data (AHCCD): Environment and Climate Change Canada, accessed July 15, 2015, at https://ec.gc.ca/dccha-ahccd/default.asp?lang=En&n=B1F8423A-1.

Esri, 2014 ArcMap 10.2.2 Hydro Tools: Esri, accessed October 9, 2014, at http://blogs.esri.com/esri/arcgis/2011/10/12/.

Garbrecht, J.D., and Rossel, F.E., 2002, Decade-scale precipitation increase in Great Plains at end of 20th century: Journal of Hydrologic Engineering, v. 7, no. 1, p. 64–75.

Government of Canada, 2015a, PFRA sub-basins of the AAFC Watersheds Project—2013: Government of Canada, accessed June 11, 2015, at http://open.canada.ca/data/en/dataset/4f3c7d6d-e018-4a69-a6cf-a4c327572b24.

Government of Canada, 2014, Water office: Government of Canada, accessed November 19, 2014, at http://wateroffice.ec.gc.ca/.

Government of Canada, 2015b, Total gross drainage areas of the AAFC Watersheds Project—2013: Government of Canada, accessed June 11, 2015, at http://open.canada.ca/data/en/dataset/67c8352d-d362-43dc-9255-21e2b0cf466c.

Gray, S.T., and McCabe, G.J., 2010, A combined water balance and tree ring approach to understanding the potential hydrologic effects of climate change in the central Rocky Mountain region: Water Resources Research, v. 46, no. 5, W05513, accessed August 20, 2015, at http://onlinelibrary.wiley.com/doi/10.1029/2008WR007650/full.

Hamon, W.R., 1961, Estimating potential evapotranspiration: Proceedings of the American Society of Civil Engineers, Journal of the Hydraulic Division, v. 87, no. 3, p. 107–120.

Helsel, D.R., and Hirsch, R.M., 2002, Statistical methods in water resources: U.S. Geological Survey Techniques of Water-Resources Investigations, book 4, chap. A3, 522 p.

Hirsch, R.M., and Ryberg, K.R., 2012, Has the magnitude of floods across the USA changed with global CO2 levels?: Hydrological Science Journal, v. 57, no. 1, p. 1–9.

Hoerling, Martin; Eischeid, Jon; Esterling, David; Peterson, Thomas; and Webb, Robert, 2010, Understanding and explaining hydro-climatic variations of Devils Lake: National Oceanic and Atmospheric Administration, Climate Assessment Report, 20 p.

Huffman, R.L., Fangmeier, D.D., Elliot, W.J., Workman, S.R., and Schwab, G.O., 2011, Soil and water conservation engineering (6th ed.): St. Joseph, Mich., American Society of Agricultural Engineers, 523 p.

Interagency Advisory Committee on Water Data, 1982, Guidelines for determining flood flow frequency: Reston, Va., U.S. Geological Survey Hydrology Subcommittee Bulletin 17B, 28 p. plus appendixes. [Also available at http://water.usgs.gov/osw/bulletin17b/bulletin_17B.html.]

International Joint Commission, 1989, Boundary waters—Agreement between the Government of Canada and the Government of the United States of America for water supply and flood control in the Souris River Basin (with Annexes and Canada/Sasketchewan agreement): Ottawa, Canada, Queen's Printer for Canada, 36 p.

International Souris River Board, 2013, Plan of study—For the review of the operating plan contained in Annex A of the 1989 international agreement between the Government of Canada and the Government of the United States of America: Souris River Basin Task Force, 197 p.

Johnson, R.C., Mercier, T.J., and Brownfield, M.E., 2014, Spatial and stratigraphic distribution of water in oil shale of the Green River Formation using Fischer Assay, Piceance Basin, northwestern Colorado: U.S. Geological Survey Open-File Report 2014–1059, 57 p., accessed April 14, 2014, at http://dx.doi.org/10.3133/ofr20141059.

Lu, Jianbiao; Sun, Ge; McNulty, S.G., and Amatya, D.M., 2005, A comparison of six potential evapotranspiration methods for regional use in the southeastern United States: Journal of the American Water Resources Association, v. 41, no. 3, p. 621–633.

Maechler, Martin; Rousseeuw, Peter; Struyl, Anja; Hubert, Mia; and Hornik, Kurt, 2015, Cluster—Cluster anaysis basics and extensions: R Foundation for Statistical Computing, R package version 1.15.2

McLeod, A.I., 1994, Diagnostic checking of periodic autoregression models with application: Journal of Time Series Analysis, v. 15, p. 221–233, accessed August 20, 2015, at http://onlinelibrary.wiley.com/doi/10.1111/j.1467-9892.1994.tb00186.x/pdf.

Menne, M.J., Williams, C.N., Jr., and Vose, R.S., 2014, United States Historical Climatology Network (USHCN) Version 2.5 serial monthly dataset: National Climatic Data Center, National Oceanic and Atmospheric Administration, accessed May 15, 2014, at http://cdiac.ornl.gov/ftp/ushcn_v2.5_monthly/.

Milly, P.C.D., Dunne, K.A., and Vecchia, A.V., 2005, Global pattern of trends in streamflow and water availability in a changing climate: Nature, v. 438, no. 7066, p. 347–50.

Murphy, E.C., Fritz, A.K., and Fleming, R.F., 1997, The Jerusalem and Tolna outlets in the Devils Lake Basin, North Dakota: North Dakota Geological Survey Report of Investigation No. 100, 36 p.

National Oceanic and Atmospheric Administration, National Climatic Data Center, 2014, Tree ring: National Oceanic and Atmospheric Administration, accessed July 15, 2014, at http://www.ncdc.noaa.gov/data-access/paleoclimatology-data/datasets/tree-ring.

Pettyjohn, W.A., 1967, Geohydrology of the Souris River Valley in the vicinity of Minot, North Dakota: U.S. Geological Survey Water-Supply Paper 1844, 53 p.

Pusc, S.W., 1994, Hydrogeology of the Minot Aquifer, Ward County, North Dakota: North Dakota State Water Commission Ground-water Studies Number 102, Part 2, 92 p.

R Core Team, 2015, R—A language and environment for statistical computing: Vienna, Austria, R Foundation for Statistical Computing, September 30, 2014, at http://www.R-project.org.

Rannie, W.F., 1998, A survey of hydroclimate, flooding, and runoff in the Red River Basin prior to 1870: Geological Survey of Canada Open-File Report 3705, 189 p.

Rao, L.Y., Sun, Ge, Ford, C.R., and Vose, J.M., 2011, Modeling potential evapotranspiration of two forested watersheds in the southern Appalachians: Transactions of the ASABE, v. 54, no. 6, p. 2067–2078.

Rosenberry, D.O., Stannard, D.I., Winter, T.C., and Martinez, M.L., 2004, Comparison of 13 equations for determining evapotranspiration from prairie wetland, Cottonwood Lake area, North Dakota, USA: Wetlands, v. 24, no. 3, p. 483–497.

Ryberg, K.R., 2015, The impact of climate variability on streamflow and water quality in the North Central United States: Fargo, North Dakota State University, Ph.D. dissertation, 277 p.

Ryberg, K.R., Lin, Wei, and Vecchia, A.V., 2014, Impact of climate variability on runoff in the north-central United States: Journal of Hydrologic Engineering, v. 19, no. 1, p. 148–158.

Shapley, M.D., Johnson, W.C., Engstrom, D.R., and Osterkamp, W.R., 2005, Late-Holocene flooding and drought in the Northern Great Plains, USA, reconstructed from tree rings, lake sediments, and ancient shorelines: The Holocene, v. 15, p. 29–41.

Small, David, and Islam, Shafiqul, 2008, Low frequency variability in fall precipitation across the United States: Water Resources Research, v. 44, no. 4, 13 p.

Small, David, and Islam, Shafiqul, 2009, A synoptic view of trends and decadal variations in autumn precipitation across the United States from 1948 to 2004: Journal of Geophysical Research, v. 114, no. D10, 14 p.

St. George, S., and Nielsen, E., 2002, Hydroclimatic change in southern Manitoba since A.D. 1409 inferred from tree rings: Quaternary Research, v. 58, no. 4, p. 103–111.

St. George, S., and Nielsen, E., 2003, Palaeoflood records for the Red River, Manitoba, Canada, derived from anatomical tree-ring signatures: The Holocene, v. 13, no. 4, p. 547–555.

U.S. Army Corps of Engineers, 2013, Regional and reconstructed hydrology of the Souris River: St. Paul District, 158 p.

U.S. Department of Agriculture, 2014, Gridded Soil Survey Geographic Database (gSSURGO) Version 1.1: accessed October 21, 2014, at https://gdg.sc.egov.usda.gov/GDGOrder.aspx.

U.S. Department of Commerce, 2012, The Missouri/Souris floods of May–August 2011: Kansas City, National Weather Service, 68 p.

U.S. Geological Survey, 2014a, The National Map Viewer: accessed September 16, 2014, at http://viewer.nationalmap.gov/viewer/.

U.S. Geological Survey, 2014b, USGS water data for North Dakota: U.S. Geological Survey, National Water Informatoin System Web page, accessed November 18, 2014, at http://waterdata.usgs.gov/nd/nwis/.

U.S. Geological Survey, 2014c, StreamStats Version 3: accessed October 8, 2014, at http://ssdev.cr.usgs.gov/ss_dev/.

U.S. Geological Survey, 2015, National Hydro Dataset (NHD0901): U.S. Geological Survey, The National Map, accessed September 8, 2014, at http://nhd.usgs.gov/wbd.html.

Vecchia, A.V., 2002, Simulation of a proposed emergency outlet from Devils Lake, North Dakota: U.S. Geological Survey Water-Resources Investigations Report 02–4042, 129 p.

Vecchia, A.V., 2008, Climate simulation and flood risk analysis for 2008–40 for Devils Lake, North Dakota: U.S. Geological Survey Scientific Investigations Report 2008–5011, 28 p., accessed June 23, 2015, at http://pubs.usgs.gov/sir/2008/5011/.

Wiche, G.J., Vecchia, A.V., Osborne, L., Wood, C.M., and Fey, J.T., 2000, Climatology, hydrology, and simulation of an emergency outlet, Devils Lake Basin, North Dakota: U.S. Geological Survey Water-Resources Investigations Report 00–4174, 16 p.

Whitcher, Brandon, 2013, Waveslim—Basic wavelet routines for one-, two- and three-dimensional signal processing: R Foundation for Statistical Computing, R package version 1.7.3, accessed October 6, 2014, at http://CRAN.R-project.org/package=waveslim.

Yang, Song, Ding, X., Zheng, D., and Li, Q., 2007, Depiction of the variations of Great Plains precipitation and its relationship with Tropical Central-Eastern Pacific SST: Journal of Applied Meteorology and Climatology, v. 46, no. 2, p. 136–153.

Yonetani, T., and Gordon, H.B., 2001, Abrupt changes as indicators of decadal climate variability: Climate Dynamics, v. 17, no. 4, p. 249–58.

Appendix. Water-Balance Model Equations

The water-balance model (WBM) consists of a series of equations, which, when operated in sequential order, estimate the amount of available water, either stored in the soil profile or contributing to runoff, at a monthly time step. Model inputs are in-depth equivalents and consist of monthly precipitation, average temperature, and potential evapotranspiration (PET) along with static variables such as available water storage capacity (AWSC) and soil permeability (K_s). Model outputs estimate the amount of available water contributing to runoff and are converted from depth equivalent values to streamflow estimates in cubic meters per second.

The first parameters in the model are two coefficients for adjusting PET computed using the Hamon method, as described in the section "Water-Balance Model Description and Calibration":

$$PET = \begin{Bmatrix} 1.1C_M PET_H, \text{May} \\ 1.1C_J PET_H, \text{June} \\ 1.1PET_H, \text{remaining months} \end{Bmatrix}$$

where

PET is adjusted PET (millimeters),
PET_H is PET computed using the Hamon method (millimeters),
C_M is the adjustment factor PET (May) found in table 8 (dimensionless), and
C_J is the adjustment factor PET(June) found in table 8 (dimensionless).

The next model parameter is a coefficient for adjusting the available soil-moisture storage capacity computed using the geographic information system (GIS) data described in the "Water-Balance Model Description and Calibration" section of this report:

$$AWSC = C_{AWS} AWSC_{GIS}$$

where

$AWSC$ is the adjusted available water storage capacity (millimeters),
$AWSC_{GIS}$ is the storage capacity computed from the GIS data (millimeters), and
C_{AWS} is the available water storage adjustment coefficient (dimensionless).

As indicated in table 8, for most of the subbasins this coefficient (C_{AWS}) was equal to one; however, some of the coefficients were larger than one, signifying depression storage may play a larger role in the amount of water retained within the subbasin as compared to running off, and some of the coefficients were less than one, signifying a subbasin with less than normal depression storage. One subbasin, Souris River near Verendrye, North Dakota (05120000), had a coefficient of 0.9, which may be the consequence of more runoff (less infiltration) being delivered from urban/suburban development in this particular subbasin that contains the city of Minot.

The other WBM parameters and equations depended on how precipitation entered the system (rain or snow). The classification of precipitation as rain or snow is dependent on monthly average temperature (T_{avg}) such that precipitation is considered rain if T_{avg} exceeds a specified threshold (T_r), snow if T_{avg} is less than a specified threshold (T_s), and a mixture of rain and snow if T_{avg} is between the two thresholds:

$$P_{snow} = \begin{Bmatrix} P, T_{avg} \le T_s = -10\ ^{\circ}\text{C} \\ P\dfrac{T_r - T_{avg}}{T_r - T_s}, T_s < T_{avg} < T_r \\ 0, T_{avg} \ge T_r = 2\ ^{\circ}\text{C} \end{Bmatrix}$$

$$P_{rain} = P - P_{snow}$$

where

P_{snow} is snow (millimeters),
P is monthly precipitation (millimeters), and
P_{rain} is rain (millimeters).

The values selected for T_r (2 degrees Celsius [°C]) and T_s (-10 °C) were similar to those selected by Gray and McCabe (2010), who used 5 °C for T_r and minus 5 °C for T_s. Differences in the thresholds for different climatic regions, topography, vegetation, and so forth, would be expected for a monthly time step. Gray and McCabe (2010) studied the Upper Yellowstone River in the Rocky Mountains.

Precipitation classified as snow is accumulated in snowpack (SN_p). Subtractions from SN_p only take place when T_{avg} is greater than (>) T_s and are lost in the form of snowmelt (SM). The fraction of SN_p lost to SM is directly related to the difference between T_{avg} and T_s as well as the time of year:

$$SM = \begin{cases} 0, T_{avg} \le T_s \\ \min[10(T_{avg} - T_s), SN_P], T_{avg} > T_s \ \text{(for January – March)} \\ \min[20(T_{avg} - T_s), SN_P], T_{avg} > T_s \ \text{(for April – December)} \end{cases}$$

where

SM is the snowmelt (millimeters) and
SN_p is the accumulated snowpack (millimeters).

The smaller value of the multiplier (10) for January–March was selected through trial and error to match the timing of the snowmelt season and is reasonable considering more energy (higher temperature) would be required to condense and ripen the snowpack early in the snowmelt season than during later months. A small portion of SM is assumed to become direct runoff during the late winter and early spring months when the ground is still frozen/thawing and not all of the SM infiltrates the soil:

$$SM_{RO} = \begin{cases} \min(C_{SM} SM, 1), \ \text{January – February} \\ \min(0.01 SM + C_{SM} SM, 5), \ \text{March} \\ \min(C_{SM} SM, 15), \ \text{April} \\ 0, \ \text{May – December} \end{cases}$$

where

SM_{RO} is the direct snowmelt runoff (millimeters) and
C_{SM} is the snowmelt adjustment coefficient (dimensionless; table 8).

A SM_{RO} cap of 1 millimeter (mm) was used between January and February, 5 mm during March, 15 mm during April, and no SM_{RO} was considered between May and December ($SM_{RO} = 0$). A cap was placed on SM_{RO} such that monthly values would not exceed reasonable values for the region.

In addition to $SM_{RO,}$ groundwater runoff also contributes directly to streamflow, but unlike SM_{RO}, groundwater runoff is subtracted from the initial soil moisture remaining from the end of previous time step:

$$GW_{RO} = F_{GW} AWS_i$$

$$AWS_u = AWS_i - GW_{RO}$$

where

GW_{RO} is groundwater runoff (millimeters),
F_{GW} is the fraction of soil moisture that becomes groundwater runoff (dimensionless),
AWS_i is initial available soil moisture from the previous time step (millimeters), and
AWS_u is updated (for the current time step) available soil moisture (millimeters).

F_{GW} depends on temperature, permeability, and the degree of soil moisture deficit:

$$F_{GW} = 0.02 \max\left(\frac{\min(T_{avg}, T_r) - T_s}{T_r - T_s}, 0\right)\left(\frac{AWS_i}{AWSC}\right)^2 e^{1.4\left(\frac{\min(K_s, 20)}{20} - 1\right)}$$

where

K_s is the soil permeability (centimeters per hour).

K_s was computed using the GIS data described in the "Water-Balance Model Description and Calibration" section. The constant multiplier (0.02) was determined through the calibration process. The second term on the right-hand side equals one if T_{avg} is greater than or equal to (≥) T_r, zero if T_{avg} is less than or equal to (≤) T_r, and lies in between 0 and 1 otherwise, and is present to reduce the groundwater runoff during winter months when soils are frozen. The third term equals one if AWS_i equals $AWSC$ and decreases as AWS_i approaches zero. The last term on the right-hand side is one if $K_s \geq 20$ centimeters per hour and decreases to a small value as K_s tends towards zero.

For the months of April and May, when there is both ground thaw and snowmelt, GW_{RO} determined from the previous equations is increased up to a maximum potential value and the extra groundwater runoff is taken from snowmelt:

$$GW_{RO}^* = \begin{Bmatrix} GW_{\max}, SM - SM_{RO} \geq GW_{\max} - GW_{RO} \\ GW_{RO} + SM - SM_{RO}, SM - SM_{RO} < GW_{\max} - GW_{RO} \end{Bmatrix} \text{ for April} - \text{May}$$

$$SM^* = SM - SM_{RO} - (GW_{RO}^* - GW_{RO}) \text{ for April} - \text{May}$$

$$GW_{RO}^* = GW_{RO}, \text{ for January} - \text{March and June} - \text{December}$$

$$SM^* = SM - SM_{RO}, \text{ for January} - \text{March and June} - \text{December}$$

where

GW_{RO}^* is the adjusted groundwater runoff (millimeters),

GW_{max} is determined by replacing AWS_i with $AWSC$ in the previous equation for F_{GW} and multiplying the resulting fraction times $AWSC$, and

SM^* is the current snowmelt remaining after subtracting snowmelt runoff and (or) extra groundwater runoff (millimeters).

After snowmelt contributions to groundwater have been determined, the remaining SM^* is combined with the remaining soil-moisture storage and rainfall input to obtain the total available water in soil-moisture storage:

$$AWS_u^* = AWS_u + SM^* + P_{rain}$$

where

AWS_u^* is the current total available water in soil-moisture storage (millimeters).

If AWS_u^* exceeds $AWSC$, more direct runoff is taken from the surplus before considering water losses to actual evapotranspiration (AET):

$$Sur_1 = \max(AWS_u^* - AWSC, 0)$$

$$DS_{RO} = \begin{cases} 0.65 C_{DRO} Sur_1 \text{ , April} \\ 0.05 C_{DRO} Sur_1 \text{ , May} \\ 0.01 C_{DRO} Sur_1 \text{ , October} - \text{November} \\ 0, \text{ otherwise} \end{cases}$$

$$Sur_2 = Sur_1 - DS_{RO}$$

where

Sur_1 is the initial surplus (millimeters),
DS_{RO} is the direct runoff from the initial surplus (millimeters),
C_{DRO} is the direct runoff adjustment coefficient (dimensionless; table 8), and
Sur_2 is the surplus remaining after direct runoff (millimeters).

The direct runoff coefficient varies by month such that April has the largest coefficient, whereas May, October, and November have much smaller coefficients. In April most of the ET comes later in the month, when surplus would be expected to runoff before ET has a chance to begin. Similarly, in May, there tends to be somewhat higher ET late in the month compared to early in the month. In October and November the ground is beginning to freeze and the crops are becoming dormant, which limits the amount of water retained in the soil profile and results in slightly more runoff.

The remaining surplus (Sur_2), if any, is used to satisfy primary ET (the amount of ET that does not come from the soil-moisture storage) and if primary ET does not satisfy PET, additional ET is removed from the soil-moisture storage:

$$AET = \begin{cases} PET, Sur_2 \geq PET \\ \min(PET, Sur_2 + F_{ST} AWSC), 0 < Sur_2 < PET \\ \min(PET, F_{ST} AWS_u^*), Sur_2 \leq 0 \end{cases}$$

$$F_{ST} = \frac{1}{25} \max(\min(T_{avg}, 24) + 1, 0)$$

where

AET is actual ET (millimeters) and
F_{ST} is the fraction of soil-moisture storage that is exposed to secondary ET (dimensionless).

This fraction is dependent on temperature, such that temperatures below -1°C result in none of the soil moisture being available for secondary ET and as temperatures increase so does the amount of soil-moisture storage available for secondary ET. If T_{avg} exceeds 24 °C, all of the soil moisture can potentially be lost to secondary ET. The reason for the temperature dependence is that most of the secondary ET is considered to result from evapotranspiration from natural vegetation and crops, which would become dormant as temperatures near freezing and grow rigorously during mid- to late summer.

After water losses to AET are considered, remaining water surplus (if any) goes to excess overland runoff:

$$EO_{RO} = \max(Sur_2 - AET, 0)$$

where

EO_{RO} is excess overland runoff for the current time step (millimeters).

To account for time to travel across the watershed, a lag was introduced such that a portion of the excess overland runoff was assumed to enter the stream in the current month and a portion in the subsequent month (table 8):

$$EO_{RO}^* = F_{EO,i-1} EO_{RO,i-1} + F_{EO,i} EO_{RO,i}$$

where

EO^{*}_{RO} is the current excess overland runoff (millimeters),

$F_{EO,i-1}$ is the fraction of excess overland runoff from the previous month entering the stream for the current month (dimensionless),

$EO_{RO,i-1}$ is excess overland runoff (millimeters) from the previous month,

$F_{EO,i}$ is the fraction of excess overland runoff for the current month entering the stream (dimensionless), and

$EO_{RO,i}$ is the excess overland runoff (millimeters) for the current month.

Considering all of the previous water gains and losses in aggregate, the total runoff for the current month is

$$TOT_{RO} = SM_{RO} + GW^{*}_{RO} + DS_{RO} + EO^{*}_{RO}$$

where

TOT_{RO} is the total runoff (millimeters).

The remaining storage at the end of the current time step (and the beginning storage at the start of the next time step) is

$$AWS_{i+1} = AWS^{*}_{u} - AET - DS_{RO} - EO_{RO,i}$$

where

AWS_{i+1} is the remaining storage at the end of the current time step (millimeters).

Once a depth equivalent of TOT_{RO} is determined for each grid cell, an average is taken over the entire subbasin and a streamflow equivalent calculated:

$$Q = 1,000\, Avg_{WS}\{TOT_{RO}\} A_{WS} / (86,400 d)$$

where

Q is monthly mean streamflow (cubic meters per second);

$Avg_{WS}\{.\}$ is the average of the total runoff for the grid cells in the watershed (millimeters);

A_{WS} is the watershed area (square kilometers); and

d is the number of days in the month.

The equation has a unit correction factor of 1,000 to convert runoff from a depth equivalent to volume in cubic meters and a unit correction factor of 86,400 to convert from days to seconds.

Publishing support provided by:
Rolla Publishing Service Center

For more information concerning this publication, contact:
Director, USGS North Dakota Water Science Center
821 East Interstate Avenue
Bismarck, North Dakota 58503
(701) 250–7400

Or visit the North Dakota Water Science Center Web site at:
http://nd.water.usgs.gov/

USGS

Kolars and others—**Stochastic Model for Simulating Souris River Basin Precipitation, Evapotranspiration, and Natural Streamflow**—SIR 2015–5185

ISSN 2328-0328 (online)
http://dx.doi.org/10.3133/sir20155185